

EFFECTS OF REDOX-CYCLING ON IRON-MINERAL TRANSFORMATIONS AND  
METATRANSCRIPTOME OF IRON(III)-REDUCING BACTERIA IN A HUMID TROPICAL  
FOREST SOIL

by

JARED LEE WILMOTH

(Under the Direction of Aaron Thompson)

ABSTRACT

The reactivity of iron(III)-(oxyhydr)oxides toward microbial iron(III)-reduction is dependent on mineral reactive surface area and solubility, properties that can be altered by redox cycling. Because carbon (C) stability and nutrient availability can be influenced by redox dynamics, there is a need to evaluate the mechanisms that govern iron(III)-(oxyhydr)oxide transformations and strategies of microbial iron(III)-reducers to access these phases under fluctuating redox conditions in soils. To do this, we characterized the native iron phases in soils from the Bisley Watershed, Luquillo Critical Zone Observatory (LCZO), PR using selective chemical extractions, X-ray diffraction and  $^{57}\text{Fe}$ -Mössbauer spectroscopy. We then conducted laboratory experiments where we exposed the soils to redox cycles with variable iron(II)-oxidation rates and measured changes in the solution and solid phase iron speciation as well as sequenced mRNA extracted from native iron(III)-reducing bacteria. The native iron composition in the LCZO soil comprised goethite and lepidocrocite, with higher solid phase iron(II) correlated with higher lepidocrocite abundance and citrate-ascorbate extractable (low crystallinity) iron.  $^{57}\text{Fe}$ -Mössbauer spectra at 140 Kelvin (K) show that iron-(oxyhydr)oxides

underwent either an increase or a decrease in crystal order due to rate of iron(II)-oxidation over multiple redox cycles in laboratory incubations. Soil RNA isolated following multiple redox cycles was subsequently depleted of rRNA and enriched for mRNA by linear amplification. *De novo* assembly of millions of paired-end Illumina reads was used to further examine the importance of several putative *c*-type cytochrome, pilin, exopolysaccharide, chemotaxis, TCA cycle and carbon degradation transcripts that were collectively binned to iron(III)-reducer genomes of *Anaeromyxobacter*, *Geobacter* and *Desulfovibrio*. We also enriched <sup>57</sup>iron in soil incubations to track iron(III)-(oxyhydr)oxide formation. We found that rapid oxidation of enriched iron(II) generates short-range-ordered (i.e. low crystallinity) iron phases that are more readily solubilized by iron(III)-reducing microorganisms than the bulk native soil iron phases at the onset of iron(III)-reduction. Some <sup>57</sup>iron-enriched solid iron(III) that is not reduced becomes incorporated into longer-range-order phases (i.e. higher crystallinity) during iron(III)-reduction. A portion of iron(II) formed in the solid phase during iron(III)-reduction displays weak magnetic order in the Mössbauer spectra collected at 4.5 K, perhaps arising from the formation of nano-magnetite or, more generally, iron(II) adsorbed/incorporated at the surface of short-range-ordered iron(III)-(oxyhydr)oxides. These processes regarding mineral-microbial interactions are expected to be linked to ecosystem-level nutrient cycling, carbon stability and global greenhouse gas emissions in highly-active, humid, tropical forest soils.

INDEX WORDS: Soil redox cycling, microbial Fe(III)-reduction, Mössbauer spectroscopy, <sup>57</sup>Fe-isotope enrichment, metatranscriptomics, mRNA, Luquillo Critical Zone Observatory, *Anaeromyxobacter*, *Geobacter*, cytochromes, carbon degradation

EFFECTS OF REDOX-CYCLING ON IRON-MINERAL TRANSFORMATIONS AND  
METATRANSCRIPTOME OF IRON(III)-REDUCING BACTERIA IN A HUMID TROPICAL  
FOREST SOIL

by

JARED LEE WILMOTH

BS, West Virginia University, 2006

MS, West Virginia University, 2009

A Dissertation Submitted to the Graduate Faculty of The University of Georgia in Partial  
Fulfillment of the Requirements for the Degree

DOCTOR OF PHILOSOPHY

ATHENS, GEORGIA

2016

© 2016

Jared Lee Wilmoth

All Rights Reserved

EFFECTS OF REDOX-CYCLING ON IRON-MINERAL TRANSFORMATIONS AND  
METATRANSCRIPTOME OF IRON(III)-REDUCING BACTERIA IN A HUMID TROPICAL  
FOREST SOIL

by

JARED LEE WILMOTH

Major Professor: Aaron Thompson

Committee: Doug Crowe  
Christof Meile  
Mary Ann Moran  
Paul Schroeder

Electronic Version Approved:

Suzanne Barbour  
Dean of the Graduate School  
The University of Georgia  
May 2016

## DEDICATION

I dedicate this dissertation and long years of hard work in science to my dear friend and mentor Mr. Randy King. Thank you for teaching me the value of being an informed skeptic, creative thinker and philosopher.

## ACKNOWLEDGEMENTS

I would like to thank all committee members for their guidance over the years and evaluation of this dissertation.

## TABLE OF CONTENTS

	Page
ACKNOWLEDGEMENTS .....	viii
LIST OF TABLES .....	xi
LIST OF FIGURES .....	xii
CHAPTER	
1 INTRODUCTION AND LITERATURE REVIEW .....	1
2 IRON(III) CRYSTALLINITY AND EXTRACELLULAR ELECTRON TRANSFER STRATEGIES OF IRON(III)-REDUCING BACTERIA ARE ALTERED BY REDOX CYCLING IN TROPICAL FOREST SOIL MICROCOSMS .....	23
ABSTRACT .....	24
INTRODUCTION .....	25
MATERIALS AND METHODS .....	29
RESULTS .....	39
DISCUSSION .....	50
CONCLUSIONS .....	57
LITERATURE CITED .....	58
TABLES AND FIGURES .....	67
APPENDIX .....	76
3 MICROBIAL FE(III)-REDUCTION IS MODULATED BY OXYGEN PULSE RATES IN REDOX-FLUCTUATING SOIL SLURRIES .....	86

ABSTRACT.....	87
INTRODUCTION .....	88
MATERIALS AND METHODS.....	91
RESULTS .....	100
DISCUSSION.....	105
CONCLUSIONS .....	108
LITERATURE CITED.....	110
TABLES AND FIGURES .....	116
APPENDIX.....	127
<b>4 CHARACTERIZATION OF IRON SOLID PHASES IN A REDOX-DYNAMIC</b>	
<b>TROPICAL FOREST SOIL .....</b>	<b>135</b>
ABSTRACT.....	136
INTRODUCTION .....	137
MATERIALS AND METHODS.....	140
RESULTS .....	143
DISCUSSION.....	146
CONCLUSION.....	150
LITERATURE CITED .....	152
APPENDIX.....	167
CONCLUSION.....	182

## LIST OF TABLES

	Page
Table 2.1. Extracted, processed and assembled transcript parameters .....	67
Appx. Table 2.1. MBS parameters.....	79
Appx. Table 2.2. Cytochrome annotations .....	82
Appx. Table 2.3. Pili, flagella, exopolysaccharide and chemotaxis annotations.....	83
Appx. Table 2.4. Carbon degradation annotations .....	84
Appx. Table 2.5. TCA cycle annotations.....	85
Appx. Table 3.1. MBS parameters table.....	127
Appx. Table 4.1. Table of total elements.....	167
Appx. Table 4.2. MBS details for plot 2 and 4 at 295, 140, 77, ~20 and 4.5 K. ....	169
Appx. Table 4.3. Average 295 (room temperature K or RTK), 140, 77, ~20 and 4.5 K key Mössbauer parameters for plot 1, 2, 4, 7, 9 and 18.....	171
Appx. Table 4.4. Correlation matrix statistics for selected variables measured in this study (see Fig. 4.7.).....	178

## LIST OF FIGURES

	Page
Figure 2.1. Fe(II) concentrations measured in the aqueous (top) and 0.5 M HCl extracted solid (bottom) phases during incubation.....	68
Figure 2.2. <sup>57</sup> Fe Mössbauer spectra collected at 140, 77 and 4.5 K for starting material and endpoint samples collected from the fast and slow oxidation treatments at 24 d.....	70
Figure 2.3. Upper quartile normalized, assembled transcripts of putative c-type cytochrome-related sequences showing differential relative abundance between the fast and slow oxidation treatments.....	71
Figure 2.4. Upper quartile normalized, assembled transcripts of putative type IV pilin, flagella, biofilm and chemotaxis related sequences showing differential relative abundance between the fast and slow oxidation treatments.....	72
Figure 2.5. Upper quartile normalized, assembled transcripts of putative environmental-C degradation-related sequences showing differential relative abundance between the fast and slow oxidation treatments.....	73
Figure 2.6. (A) Pathway of detected TCA cycle enzyme transcripts binning to <i>Anaeromyxobacter</i> (derived from KEGG map 00020, 9/25/14, (c) Kanehisa Laboratories) (B) Upper quartile normalized, assembled transcripts of putative TCA cycle related sequences showing differential relative abundance between the fast and slow oxidation treatments .....	75

Appx. Figure 2.1. Taxonomy-based collector's curves at the phylum and species ranks combining assembled transcripts contigs from the fast and slow oxidation treatments for each curve.....	76
Appx. Figure 2.2. Count of assembled transcript contigs, from the fast and slow oxidation treatments combined, binning to prokaryotic phyla, by Proteobacteria class, by Deltaproteobacteria genus and to the top three (Fe(III)-reducing) genera at the species-strain level representing <i>Anaeromyxobacter</i> , <i>Geobacter</i> and <i>Desulfovibrio</i> .....	77
Appx. Figure 2.3. Count of assembled transcript contigs that were at significantly higher relative abundance in either the fast or slow oxidation treatment (p;q <0.05) (n=3) at the class level that binned to prokaryotes.....	78
Figure 3.1. Fast, Medium and Slow oxidation rates of supplied Fe(II), supplied as FeCl <sub>2</sub> , (experiment #1) lead to different rates of microbial Fe(III)-reduction in LCZO soils following oxic conditions.....	116
Figure 3.2. Net rate of Fe(II)-production (aqueous + 0.5 M HCl extractable Fe(II)) between 24 and 360 hrs (between sample point 4 and 7), following 24 hrs oxidation in Fast, Medium (Med) and Slow treatments, including the Anoxic control.....	117
Figure. 3.3. Enriched <sup>57</sup> Fe-label and control microcosm Fe(II) concentrations in the aqueous and 0.5 M HCl extractable phases.....	118
Figure. 3.4. <sup>57</sup> / <sup>54</sup> Fe isotope ratios in the aqueous (Aq Fe) and 0.5 M HCl extractable (Solid Fe) phases for the <sup>57</sup> Fe-label treatment.....	119
Figure 3.5. Aqueous and 0.5 M HCl-extractable % <sup>57</sup> Fe, added <sup>57</sup> Fe-label (with natural abundance <sup>57</sup> Fe subtracted) and total extractable Fe during incubation.....	120

Figure 3.6. $^{57}\text{Fe}$ -label shown as atom distributions (% total added $^{57}\text{Fe}$ atoms) in $^{57}\text{Fe}$ -enriched samples under oxic (8 d combined triplicates from enriched trt) and anoxic (15 d combined triplicates from enriched trt) conditions, and measured by MBS at 140 and 4.5 K.....	121
Figure 3.7. Natural abundance $^{57}\text{Fe}$ shown as atom distributions in $\text{FeCl}_2$ control samples (not enriched with added $^{57}\text{Fe}$ ) under oxic (8 d mixed replicates from control trt) and anoxic (15 d mixed replicates from control trt) conditions, and measured by MBS at 140 and 4.5 K. ....	122
Fig 3.8. $^{57}\text{Fe}$ -Mössbauer spectra collected at 140 K after calculating differences between treatment and control $^{57}\text{Fe}$ -site populations. ....	124
Fig 3.9. $^{57}\text{Fe}$ -Mössbauer spectra collected at 4.5 K after calculating differences between treatment and control $^{57}\text{Fe}$ -site populations. ....	125
Figure 3.10. High resolution electron micrograph of representative cluster of 3-8 nm Fe-(oxyhydr)oxides collected from undisturbed, oxic, soil microcosm.....	126
Appx. Figure 3.1. Fe(II)-sorption isotherm for LCZO soil using aqueous Fe(II) concentrations ranging from 0 to 50 mM (as $\text{FeCl}_2 \cdot 4\text{HCl}$ ) under anoxic conditions.....	129
Appx. Figure 3.2. XRD was performed on the air-dry starting material using a Bruker Advance diffractometer with a Co- $K\alpha$ source. ....	130
Appx. Figure 3.3. High resolution electron micrograph of representative cluster of 3-8 nm Fe-(oxyhydr)oxides collected from undisturbed, oxic, soil microcosm without post-imaging analysis. ....	131
Appx. Figure 3.4. High resolution electron micrograph of representative cluster of 3-8 nm Fe-(oxyhydr)oxides collected from undisturbed, oxic, soil microcosm with dimensional analysis after imaging. ....	132

Appx. Figure 3.5. Energy dispersive X-ray spectrum (EDXS) of nano-Fe cluster collected from undisturbed, oxic, soil microcosm (spot size diameter = 25 nm). .....	133
Appx. Figure 3.6. Electron energy loss spectrum (EELS) of nano-Fe cluster collected from undisturbed oxic (blue line) and anoxic (red line) soil microcosms (spot size diameter = 25 nm). .....	134
Figure 4.1. Extracts from field moist and freeze dried soils (n=18 field plots).....	160
Figure 4.2. Box plots of total Fe concentrations in duplicate acid ammonium oxalate (AAO) and citrate ascorbic acid (CA) extracts from field moist and freeze dried soils (n=18 field plots)...	161
Figure 4.3. XRD was performed on the freeze-dried soils from plots 1, 2, 4, 7, 9 and 18 using a Bruker Advance diffractometer with a Co-K $\alpha$ source. ....	162
Figure 4.4. $^{57}\text{Fe}$ Mössbauer spectra collected at 295, 140, 77, 20 and 4.5 K for freeze-dried plots 2 and 4. Raw spectral data points are shown as black open circles. ....	163
Figure 4.5. Probability density distributions of the dominant sextets (HFD-OxHy) from plot 2 and plot 4 MBS spectra collected at 4.5 K.....	164
Figure 4.6. Most probable hyperfine field, H peak vs. average $B_{\text{hf}}$ quadrupole shift, $\langle e \rangle$ , for the HFD-OxHy sextets, primary site-component 1, of freeze-dried samples (n=6) at 140, 77 and ~20 K.....	165
Figure 4.7. Correlation matrix for selected variables measured in this study. Al/Fe ratios were calculated from total elements analysis. ....	166

Appx. Figure 4.1. XRD was performed on the freeze-dried bulk soils from plots 1, 2, 4, 7, 9 and 18 using a Bruker Advance diffractometer with a Co-K $\alpha$ source.....	179
Appx. Figure. 4.2. Raw MBS spectra (observed data points) of freeze-dried plot samples 1, 2, 4, 7, 9 and 18 collected at 295, 140, 77 and 20 K.....	180
Appx. Figure 4.3. $^{57}\text{Fe}$ Mössbauer spectra collected at 4.5 K for freeze-dried plots P2 and P4.	181

## CHAPTER 1

### INTRODUCTION AND LITERATURE REVIEW

The microbial reduction of iron (Fe) minerals can shape the biogeochemistry in terrestrial environments that undergo fluctuations in redox status (Scharer *et al.*, 2009; DeAngelis *et al.*, 2010; Dubinsky *et al.*, 2010; Liang *et al.*, 2012). Under oxic conditions, microbes couple electron-rich energy sources (e.g. organic carbon (OC)) to molecular oxygen (O<sub>2</sub>) during respiration. At sufficiently low O<sub>2</sub> concentrations— or in the absence of O<sub>2</sub>— a series of alternate terminal electron acceptors become more thermodynamically favored (Richter *et al.*, 2012a; Roden, 2012; Merkle *et al.*, 2015). These electron acceptors include nitrate (NO<sub>3</sub><sup>-</sup>, which is reduced to NO<sub>2</sub><sup>-</sup>), manganese (Mn(IV), which is reduced to Mn(II)) and iron (Fe(III), which is reduced to Fe(II)). Although energy yield is theoretically higher for NO<sub>3</sub><sup>-</sup> and Mn(IV) reduction, Fe(III) is typically present in most soils and is therefore a more abundant electron acceptor in soils exposed to anoxic conditions (Bradley *et al.*, 1998; Zachara *et al.*, 1998; Pett-Ridge *et al.*, 2006; Song *et al.*, 2015).

It is well known that Fe-(oxyhydr)oxides bind important plant nutrients (e.g. P) through specific molecular arrangements (Scharer *et al.*, 2009). For example, there is an active hydroxyl site every 22 to 24 Å<sup>2</sup> on the mineral surface of a typical Fe-(oxyhydr)oxide. The PO<sub>4</sub><sup>3-</sup> tetrahedron has a base of approximately 21.6 Å<sup>2</sup>, allowing the hydroxyl sites to adsorb PO<sub>4</sub><sup>3-</sup> without steric hindrance (Hassett, 1992). It is now known generally that when O<sub>2</sub> diminishes in soil pore spaces (e.g. pore saturation by rainfall, followed by respiratory turnover), certain groups of bacteria can directly or indirectly utilize the iron-reducing pathway (Pett-Ridge and

Firestone, 2005). Reduction of Fe(III) is more ubiquitous in soils than previously thought, even occurring in soils exposed on average to predominantly oxic conditions (Sexstone *et al.*, 1985; Weiss *et al.*, 2004; Pett-Ridge *et al.*, 2006). Redox oscillation has also been shown to be a primary factor (Thompson *et al.*, 2006; Coby *et al.*, 2011; Cismasu *et al.*, 2016). During redox oscillations, soil OC becomes degraded, solid Fe is subsequently transformed and bound nutrients like P can be released for biological consumption (Bradley *et al.*, 1998; Peretyazhko and Sposito, 2005; Pett-Ridge *et al.*, 2006; Scharer *et al.*, 2009; Liptzin *et al.*, 2011). Humid tropical forests have the highest soil respiration rates of any terrestrial ecosystem (Raich and Schlesinger, 1992) and the fastest rates of decomposition globally (Cusack *et al.*, 2011). Rapid rates of C-oxidation occur in soils that typically experience fluctuating redox conditions (Liptzin *et al.*, 2011). The coupled behavior of global C soil-atmosphere exchange as well as P mobility and specific microbial community responses in environments continuously undergoing transitions in redox status remains poorly understood.

When O<sub>2</sub> infiltrates anoxic or low-O<sub>2</sub> soil, a significant portion of Fe(II) will oxidize to Fe(III) and depending on the pH and abundance of complexing ligand, most Fe(III) will then rapidly hydrolyze to Fe-(oxyhydr)oxides (Singer and Stumm, 1970; Weiss *et al.*, 2004). Reduced Fe (Fe(II)) that accumulates during anoxic conditions may be oxidized to Fe(III) phases that are similar or different than the precursor Fe(III) phase that was reduced (Tufano *et al.*, 2009). In Fe-dominated and low pH soils, Fe(II) tends to adsorb onto solid-phase surfaces during microbial Fe(III)-reduction (Tufano *et al.*, 2009; Wu *et al.*, 2010). Studies show that the adsorbed Fe(II) can accelerate crystal ripening, a process that describes the transformation of small, thermodynamically less stable crystals to larger, more stable crystals (Steeffel and Vancappellen, 1990; Hansel *et al.*, 2005; Tufano *et al.*, 2009). This mechanism highlights the importance of

reactive mineral dissolution and subsequent precipitation during crystal growth (Steeffel and Vancappellen, 1990).

Laboratory studies on highly weathered tropical soils from Puerto Rico suggest that prolonged or fluctuating redox status does not significantly alter Fe solid transformations (Pett-Ridge *et al.*, 2006; DeAngelis *et al.*, 2010). However, Thompson *et al.* (2006) used Mössbauer spectroscopy to show that imposed redox fluctuations on Hawaiian soils increased Fe crystal order. Understanding the implications of Fe redox dynamics in tropical systems is critical for predicting nutrient cycling and C degradation/sequestration, as well as microbial community responses that often drive nutrient and C cycles.

Past and recent published studies on Bisley soils (Luquillo, Puerto Rico) have examined redox fluctuations with fixed oxidation rates during oxic cycles (Pett-Ridge and Firestone, 2005; Pett-Ridge *et al.*, 2006; DeAngelis *et al.*, 2010). This is also the general case in other soil systems research (Komlos *et al.*, 2007). Thus, the redox dynamics observed in these studies were dependent on oxic cycles that were relatively static, with no changes in oxidation rate. However, variation in Fe(III)-oxide crystallinity can occur during formation under different oxidation rates of Fe(II) in the lab (Carlson and Schwertmann, 1990; Steefel and Vancappellen, 1990; Schwertmann and Cornell, 1991; Cabot *et al.*, 2007; Gotic *et al.*, 2008). Consequently, differences in the rate of Fe(II)-oxidation in soils are expected to affect changes in the crystallinity and reactivity of the resulting Fe(III) solid phases. The slow oxidation of Fe(II) may result in the formations of more crystalline Fe minerals than if Fe(II) was oxidized more rapidly (Steeffel and Vancappellen, 1990). Sorption of Fe(II) onto Fe-(oxyhydr)oxides during anoxic conditions, followed by variable oxidation rates, may be an important determinant in the *net* crystallinity of Fe(III) phases in soils (Tufano *et al.*, 2009).

Iron(III) solid phases of lower crystallinity are likely to have faster rates of microbial reduction due to higher surface area and higher solubility of short-range-ordered phases (Zachara *et al.*, 1998; Roden, 2006; Bonneville *et al.*, 2009). Evaluating Fe reduction in the Luquillo soils on the basis of changes in Fe crystal order is important for many reasons, but two in particular: (1) as mentioned previously, the majority of relevant environmental studies have examined oxidation as a static parameter in the lab (no change in oxidation rate); and (2) observing changes in net Fe(III) reduction rates, which are known to impact coupled C and P cycling, in parallel with changes in Fe crystallinity would help link critical biogeochemical pathways in soils. With regard to reason (1), past research has primarily used O<sub>2</sub> saturation as a general parameter for affecting Fe, nitrogen (N), C and microbial responses during oxic incubation cycles, but have not explicitly tested the effects of different oxidation rates (Weiss *et al.*, 2004; Pett-Ridge *et al.*, 2006; Komlos *et al.*, 2007; Stewart *et al.*, 2009; DeAngelis *et al.*, 2010; Cismasu *et al.*, 2016). Reason (2) highlights the importance of understanding how Fe(III) solids are linked to and govern biogeochemical processes in soils. Modulation of Fe(II)-oxidation rates is a novel means for studying the behavior of Fe mineral transformations and microbial activity as affected by soil redox-cycling.

### Iron Minerals in Tropical Soils

The physical properties of soil Fe phases such as size, structure, surface area and atomic order are important geochemical parameters that regulate the bioavailability of essential compounds (e.g. OC and P) (Hutchison and Hesterberg, 2004; Scharer *et al.*, 2009; Hiemstra *et al.*, 2013; Mallet *et al.*, 2013; Saidy *et al.*, 2013), retention of organic and inorganic contaminants (Hanna, 2007; Wang *et al.*, 2008; Jiskra *et al.*, 2012) and are both dependent on and influenced

by the rate and extent of Fe-redox transformations (Zachara *et al.*, 1998; Hansel *et al.*, 2004; Roden, 2006; Bonneville *et al.*, 2009; Coby *et al.*, 2011; Li *et al.*, 2012a). Tropical soils that are highly weathered and experience changes in redox conditions due to wetting and drying cycles (i.e. transitions between atm O<sub>2</sub> depletion and atm O<sub>2</sub> saturation) are of great interest because Fe minerals are relatively abundant, facilitate P immobilization under oxic conditions and release limited P and are coupled to OC oxidation during anoxic conditions (Miller *et al.*, 2001; Chacon *et al.*, 2005; Peretyazhko and Sposito, 2005; Liptzin and Silver, 2009). Soils of the Bisley Watershed, Luquillo Critical Zone Observatory (LCZO), Puerto Rico—as part of the NSF sponsored Long Term Ecological Research Program—have been used in numerous studies involving redox transitions, including studies on microbial community structure and activity; and the biogeochemical cycling of Fe, C and P (Peretyazhko and Sposito, 2005; DeAngelis *et al.*, 2010; Dubinsky *et al.*, 2010; Liptzin *et al.*, 2011; DeAngelis and Firestone, 2012; Minyard *et al.*, 2012). However, little information exists on the characteristics of the Fe minerals in these redox-dynamic soils.

#### Chemical Extraction and X-ray Diffraction

Because the Fe minerals are generally difficult to physically separate and isolate for direct characterization in soil (Bigham *et al.*, 1978; Wu *et al.*, 2012; Regelink *et al.*, 2013), operationally defined chemical extractions have been used to assess the abundance and composition of Fe oxides. Extraction of soil iron with dithionite-citrate-bicarbonate (DCB) (Loeppert and Inskeep, 1996) gives an estimate of the abundance of total reducible Fe oxides, whereas acid-ammonium-oxalate (AAO) (McKeague and Day, 1966) and citrate-ascorbic acid (CA) (Reyes and Torrent, 1997) solutions solubilize primarily short-range-ordered (SRO) Fe

oxides. The composition of all minerals solubilized by these extractants can often be estimated by the extracted Al, Si, Fe, Ti, Mn and P (Bigham *et al.*, 1978; Peretyazhko and Sposito, 2005).

Alternatively, Fe solid phases can be analyzed via techniques that do not significantly alter mineral chemical and physical properties (i.e., non-destructive techniques). X-ray diffraction (XRD) is a non-destructive technique that yields information on the structure and relative abundance of many crystalline minerals, but may be insufficient to study the Fe solid phases of interest due to their lower concentrations and short-range order in soils (Schwertmann *et al.*, 1982; Refait *et al.*, 2001). These properties may explain observed differences between abundance of reducible Fe oxides derived from DCB extractions and abundance of Fe oxides detected by XRD in highly weathered soils (Bigham *et al.*, 1978; Peretyazhko and Sposito, 2005).

#### <sup>57</sup>Fe-Mössbauer Spectroscopy

Mössbauer spectroscopy (MBS) has been used in conjunction with XRD and chemical extractions to study Fe solid phases in soils (Bigham *et al.*, 1978; Schwertmann *et al.*, 1982; Thompson *et al.*, 2011). MBS is a non-destructive technique that probes the composition of <sup>57</sup>Fe in the soil and can describe the Fe solid phases irrespective of crystal ordering or the degree of foreign-ion substitution (Bigham *et al.*, 1978; Schwertmann *et al.*, 1982; Amarasiriwardena *et al.*, 1986; Fontes *et al.*, 1992; Komlos *et al.*, 2007; Mikutta *et al.*, 2008; Murad, 2010; Thompson *et al.*, 2011; Larese-Casanova *et al.*, 2012; Dhakal *et al.*, 2013). A concise overview of MBS and its application to environmental samples can be found in Kukkadapu *et al.* (2006); Murad (2010). Previous characterizations of Fe in surface soils of the tropics have included operational extractions as measures of Fe oxide crystallinity and solid phase analysis with MBS and XRD (Bigham *et al.*, 1978; Amarasiriwardena *et al.*, 1986; Peretyazhko and Sposito, 2005). In general,

tropical soils are replete with a relatively large proportion of short-range-ordered Fe minerals (Bigham *et al.*, 1978; Peretyazhko and Sposito, 2005).

### Iron Transformations During Redox Cycling

In surface soils, redox cycling can be perpetuated by O<sub>2</sub> fluctuations driven by periodic rainfall that infiltrates soil pore spaces (Liptzin *et al.*, 2011). Anoxic and/or O<sub>2</sub>-limited conditions that arise cause certain bacteria to use soluble and insoluble Fe(III) minerals in terminal electron accepting pathways to facilitate growth (Roden, 2012). Over successive alternating oxic and anoxic cycles, Fe(III) minerals can change in crystallinity (Thompson *et al.*, 2006). The exact mechanisms of these crystalline changes have not been comprehensively evaluated in soils and resulting changes in crystallinity vary depending on the initial conditions and characteristics of the redox fluctuation (Thompson *et al.*, 2006; Komlos *et al.*, 2007; Scharer *et al.*, 2009).

During the synthesis of Fe(III)-(oxyhydr)oxides, slower Fe(II) oxidation rates by O<sub>2</sub> tend to form more crystalline minerals as opposed to faster rates which favor more short-range-ordered phases (Carlson and Schwertmann, 1990; Schwertmann and Cornell, 1991). Slow Fe(II)<sub>aq</sub>-oxidation allows Fe(III) atoms to arrange themselves in larger crystals, whereas faster precipitation does not (Steefel and Vancappellen, 1990). Oxidation of Fe(II) adsorbed on Fe(III) solid phases can lead to de novo minerals of variable crystallinity (Park and Dempsey, 2005). The reactive surface area of Fe(III)-(oxyhydr)oxides is perhaps the most important constraint on microbial Fe(III) reduction kinetics (Roden, 2006) and is likely to influence trajectory of changes in Fe(III) crystallinity during soil redox cycling (Zachara *et al.*, 1998; Tufano *et al.*, 2009; Roden, 2012).

## Iron Mineral and Microbial Interactions

The impact of redox fluctuations on Fe(III) mineral transformations and molecular mechanisms of extracellular electron transfer by Fe(III)-reducing microorganisms (e.g. *c*-type cytochromes, electrically conductive pili, biofilms and chemotaxis proteins) is environmentally relevant (Coby *et al.*, 2011; Richter *et al.*, 2012a; Parsons *et al.*, 2013; Smith *et al.*, 2013), especially in soils where mineral-microbial interactions govern many aspects of nutrient and C cycling (Pett-Ridge *et al.*, 2006; Li *et al.*, 2012b). Characterizing the coevolution of mineral composition and microbial activity in fluctuating redox soils poses many analytical challenges when compared to synthetic systems. Fe(III) minerals in most soils typically do not exist as discrete phases with well-defined boundaries, but instead form a continuum of crystalline order and speciation that in turn gives rise to differences in reactivity (Bigham *et al.*, 1978; Hansel *et al.*, 2004; Pallud *et al.*, 2010; Thompson *et al.*, 2011; Sjöstedt *et al.*, 2013). In addition, many different microbial taxa have the ability to reduce Fe(III) in soils (Loneragan *et al.*, 1996; Kato *et al.*, 2012; Liang *et al.*, 2012).

## RNA-Sequencing of Soil Metatranscriptomes

Modeling of microbial Fe(III)-reduction (Roden, 2006; Bonneville *et al.*, 2009), and genome sequencing of model organisms such as *Geobacter sulfurreducens* (Mahadevan *et al.*, 2006), have elucidated select aspects of Fe biogeochemistry as they may occur in nature, however, detailed studies of more environmentally relevant systems are lacking. Next generation RNA-sequencing (RNAseq) can describe the soil metatranscriptome of Fe(III)-reducers at the precise time of sampling as the turnover rate of mRNA molecules is on the order of seconds to minutes (Gifford *et al.*, 2011). RNAseq analysis of anoxic soils is a current challenge in microbial ecology due in part to the presence of degraded organics, fermentation

byproducts and metal cations that interfere with RNA isolation, purification and cDNA library construction (Tveit *et al.*, 2014). Despite such difficulties, evaluating mechanistic coupling between changes in Fe(III) crystallinity/reactivity and the strategies of Fe(III)-reducers to utilize extracellular forms of Fe(III) during soil redox transitions will improve our conceptual model of biogeochemical cycling at the ecosystem level.

#### Microbial Strategies for Electron-Transfer to Insoluble Fe(III)-oxides

Members of the Delta and Gammaproteobacteria (e.g. *Geobacter* and *Shewanella*) have been used extensively to gauge microbial activity in Fe(III)-reducing environments (Childers *et al.*, 2002; Liang *et al.*, 2012; Leung *et al.*, 2013; Embree *et al.*, 2014; Szeinbaum *et al.*, 2014). Representatives within these groups are specialized with regard to Fe(III) reduction, as they can use insoluble forms of extracellular Fe(III) as terminal electron acceptors coupled to ATP production through the TCA cycle. Other less specialized bacteria that rely on fermentation are not known to efficiently grow using Fe(III) reduction (Lehours *et al.*, 2010).

Species of *Geobacter* can use of organic C as both electron donor and acceptor, insoluble Fe(III) phases and electrodes as terminal electron acceptors, and remediation of radionuclide and organic pollutants (Lovley, 2011; Richter *et al.*, 2012b). Unlike *Shewanella* and *Geothrix* that can produce soluble electron-shuttles and/or chelating moieties to transfer electrons to extracellular Fe(III), *Geobacter* predominantly accesses extracellular Fe(III) surfaces by direct contact using outer-membrane *c*-type cytochromes, electrically conductive pili (e.g. microbial nanowires) and specialized chemotaxis directed toward Fe(II) generation (Leang *et al.*, 2005; Smith *et al.*, 2013). These features likely give *Geobacter* a competitive advantage over other Fe(III)-reducers in soils and sediments (Childers *et al.*, 2002).

The model Fe(III)-reducers *Geobacter metallireducens* and *Geobacter sulfurreducens* also grow flagella and form multi-heme *c*-type cytochromes along electrically conductive pili, respectively, when grown on insoluble Fe(III) minerals (Childers *et al.*, 2002; Smith *et al.*, 2013). However, many diverse bacteria including *Shewanella* use surface cytochromes and electrically conductive pili in a similar manner, although the mechanisms and efficiency of electron transport across such components vary depending on the organism (Gorby *et al.*, 2006; Smith *et al.*, 2013). Cell-surface *c*-type cytochromes and associated Fe(III)-reducing functionality are thought to be poorly conserved among *Geobacter* species (Smith *et al.*, 2013). This feature of cytochrome conservation could theoretically allow for the unique identification of particular cytochromes associated with particular species (i.e. using unique cytochromes as bioindicators in complex systems). Overall, outer-membrane *c*-type cytochromes of microbial Fe(III)-reducers in particular offer a direct, well recognized, molecular mechanism at the mineral-microbial interface to study the pathway of electron transfer between organic C and Fe(III) minerals in soils.

#### Microbial Characterizations in the LCZO

Recent 16S rRNA microarray and qPCR-based studies of the LCZO soils indicate that members of *Geobacter*, *Geothrix* and *Shewanella* are at least five orders of magnitude lower in abundance compared to the total population under environmental conditions (DeAngelis *et al.*, 2010). Consequently, Fe(III) reduction in these highly active tropical soils is likely performed in concert by many taxonomically diverse organisms. However, the insolubility and inaccessibility of soil Fe(III) pools likely limits energy conservation for cell growth, and Fe(III)-reducers using specialized-extracellular electron transfer pathways should therefore have a competitive advantage (Lehours *et al.*, 2010). Even at low cell counts in a diverse community, specialized

Fe(III)-reducers might display unique and high level activity, the functionality of which cannot be deduced purely based on analysis of rRNA and/or rRNA genes (DeAngelis *et al.*, 2010; Midgley *et al.*, 2012).

The rate of oxidation is not likely to directly influence microbial Fe(III) reducers, but rather indirectly influence them through the formation of Fe(III) phases of different crystal order and hence different reactivity. Several studies have been published on the microbial community response to changes in redox status in tropical soils (Pett-Ridge and Firestone, 2005; Pett-Ridge *et al.*, 2006; DeAngelis *et al.*, 2010; DeAngelis and Firestone, 2012; Nissen *et al.*, 2012; Song *et al.*, 2015), including the use of biomolecular techniques such as TRFLP, qPCR and DNA/RNA microarray analysis (DeAngelis *et al.*, 2010). Generally, these techniques yield phylum and order level taxonomic delineation (DeAngelis *et al.*, 2010; DeAngelis and Firestone, 2012). Four general anoxic/oxic interval treatments have been used to alter redox status in Bisley soils: 12 hr anoxic/oxic, 4 d anoxic/oxic, continuous anoxic and continuous oxic (Pett-Ridge *et al.*, 2006; DeAngelis *et al.*, 2010). It should be noted that imposed fluctuating redox cycles in these soils have tended to be temporally symmetric, that is to say anoxic cycle intervals have equaled oxic cycle intervals during oscillations. From these studies, reported findings have been (1) that significant changes in community composition occur in continuous (static) oxic and anoxic treatments, (2) rapid redox fluctuations (i.e. 12 hr cycles) show similar community composition to static anoxic treatments, (3) microbial composition under a longer (i.e. 4 d) redox frequency is not significantly different from the native composition, (4) transcriptome/genome microarray analysis has shown that a significant number of organisms become more active under fluctuating redox conditions, even though community composition does not significantly change and (5) that

specialized Fe reducers *Geobacter*, *Shewanella* and *Geothrix* make up <1% of the total microbial population by cell abundance.

With regard to findings (1) and (2), community composition actually decreases under static redox conditions, as well as in rapid 12 hr fluctuations (Pett-Ridge *et al.*, 2006; DeAngelis *et al.*, 2010). Pett-Ridge *et al.* (2006) propose that the similarity of the microbial composition during rapid cycles to that during the static anoxic treatment is due to the extremely high O<sub>2</sub> demand in these soils, where available O<sub>2</sub> is quickly metabolized following an oxic cycle such that sub-oxic conditions persist during a high-frequency redox oscillation experiment (Pett-Ridge *et al.*, 2006). Findings (3) and (4) suggest that in these soils Fe reducers are a ubiquitous feature of the native microbial community (DeAngelis *et al.*, 2010). Finding (5) may indicate the relative abundance of specialized Fe reducers in these soils, but does not account for their activity as measured by important gene expression during Fe(III)-reducing conditions (DeAngelis and Firestone, 2012). The DNA/RNA microarray approach used previously (DeAngelis *et al.*, 2010) has a detection limit near the observed number of these specific Fe reducers (<1% of the total microbial population by cell abundance), such that rRNA abundances of these organisms during oscillating redox status could not be determined, and remains unknown (DeAngelis *et al.*, 2010). Even in a soil with ubiquitous Fe-reducing microbes, highly specialized activity could very well have a significant impact on Fe, C, and P dynamics.

#### LITERATURE CITED

Amarasiriwardena DD, Degraeve E, Bowen LH, Weed SB. (1986). Quantitative-determination of aluminum-substituted goethite-hematite mixtures by mossbauer-spectroscopy. *Clay Clay Min.* **34**: 250-256.

- Bigham JM, Golden DC, Bowen LH, Buol SW, Weed SB. (1978). Iron-oxide mineralogy of well-drained ultisols and oxisols .1. Characterization of iron-oxides in soil clays by mossbauer-spectroscopy, x-ray-diffractometry, and selected chemical techniques. *Soil Science Society of America Journal* **42**: 816-825.
- Bonneville S, Behrends T, Van Cappellen P. (2009). Solubility and dissimilatory reduction kinetics of iron(iii) oxyhydroxides: A linear free energy relationship. *Geochim Cosmochim Acta* **73**: 5273-5282.
- Bradley PM, Chapelle FH, Lovley DR. (1998). Humic acids as electron acceptors for anaerobic microbial oxidation of vinyl chloride and dichloroethene. *Appl Environ Microb* **64**: 3102-3105.
- Cabot A, Puntès VF, Shevchenko E, Yin Y, Balcells L, Marcus MA *et al.* (2007). Vacancy coalescence during oxidation of iron nanoparticles. *J Am Chem Soc* **129**: 10358-+.
- Carlson L, Schwertmann U. (1990). The effect of co<sub>2</sub> and oxidation rate on the formation of goethite versus lepidocrocite from an fe(ii) system at ph-6 and ph-7. *Clay Miner* **25**: 65-71.
- Chacon N, Dezzio N, Munoz B, Rodriguez JM. (2005). Implications of soil organic carbon and the biogeochemistry of iron and aluminum on soil phosphorus distribution in flooded forests of the lower orinoco river, venezuela. *Biogeochemistry* **73**: 555-566.
- Childers SE, Ciufo S, Lovley DR. (2002). *Geobacter metallireducens* accesses insoluble fe(iii) oxide by chemotaxis. *Nature* **416**: 767-769.
- Cismasu AC, Williams KH, Nico PS. (2016). Iron and carbon dynamics during aging and reductive transformation of biogenic ferrihydrite. *Environ Sci Technol* **50**: 25-35.

- Coby AJ, Picardal F, Shelobolina E, Xu HF, Roden EE. (2011). Repeated anaerobic microbial redox cycling of iron. *Appl Environ Microb* **77**: 6036-6042.
- Cusack DF, Silver WL, Torn MS, Burton SD, Firestone MK. (2011). Changes in microbial community characteristics and soil organic matter with nitrogen additions in two tropical forests. *Ecology* **92**: 621-632.
- Deangelis KM, Silver WL, Thompson AW, Firestone MK. (2010). Microbial communities acclimate to recurring changes in soil redox potential status. *Environ Microbiol* **12**: 3137-3149.
- Deangelis KM, Firestone MK. (2012). Phylogenetic clustering of soil microbial communities by 16s rna but not 16s rrna genes. *Appl Environ Microb* **78**: 2459-2461.
- Dhakal P, Matocha CJ, Huggins FE, Vandiviere MM. (2013). Nitrite reactivity with magnetite. *Environmental Science & Technology* **47**: 6206-6213.
- Dubinsky EA, Silver WL, Firestone MK. (2010). Tropical forest soil microbial communities couple iron and carbon biogeochemistry. *Ecology* **91**: 2604-2612.
- Embree M, Qiu Y, Shieu WD, Nagarajan H, O'neil R, Lovley D *et al.* (2014). The iron stimulon and fur regulon of geobacter sulfurreducens and their role in energy metabolism. *Appl. Environ. Microbiol.* **80**: 2918-2927.
- Fontes MR, Weed SB, Bowen LH. (1992). Association of microcrystalline goethite and humic-acid in some oxisols from brazil. *Soil Science Society of America Journal* **56**: 982-990.
- Gifford SM, Sharma S, Rinta-Kanto JM, Moran MA. (2011). Quantitative analysis of a deeply sequenced marine microbial metatranscriptome. *Isme J.* **5**: 461-472.

- Gorby YA, Yanina S, Mclean JS, Rosso KM, Moyles D, Dohnalkova A *et al.* (2006). Electrically conductive bacterial nanowires produced by *Shewanella oneidensis* strain MR-1 and other microorganisms. *Proc. Natl. Acad. Sci. U. S. A.* **103**: 11358-11363.
- Gotic M, Music S, Popovic S, Sekovanic L. (2008). Investigation of factors influencing the precipitation of iron oxides from Fe(II) containing solutions. *Croat Chem Acta* **81**: 569-578.
- Hanna K. (2007). Adsorption of aromatic carboxylate compounds on the surface of synthesized iron oxide-coated sands. *Appl Geochem* **22**: 2045-2053.
- Hansel CM, Benner SG, Nico P, Fendorf S. (2004). Structural constraints of ferric (hydr)oxides on dissimilatory iron reduction and the fate of Fe(II). *Geochim Cosmochim Acta* **68**: 3217-3229.
- Hansel CM, Benner SG, Fendorf S. (2005). Competing Fe(II)-induced mineralization pathways of ferrihydrite. *Environ Sci Technol* **39**: 7147-7153.
- Hassett JJBWL 1992. *Soils & their environments*, New Jersey, Prentice Hall.
- Hiemstra T, Mia S, Duhaut PB, Molleman B. (2013). Natural and pyrogenic humic acids at goethite and natural oxide surfaces interacting with phosphate. *Environmental Science & Technology* **47**: 9182-9189.
- Hutchison KJ, Hesterberg D. (2004). Dissolution of phosphate in a phosphorus-enriched ultisol as affected by microbial reduction. *J. Environ. Qual.* **33**: 1793-1802.
- Jiskra M, Wiederhold JG, Bourdon B, Kretzschmar R. (2012). Solution speciation controls mercury isotope fractionation of Hg(II) sorption to goethite. *Environ Sci Technol* **46**: 6654-6662.

- Kato S, Hashimoto K, Watanabe K. (2012). Microbial interspecies electron transfer via electric currents through conductive minerals. *P Natl Acad Sci USA* **109**: 10042-10046.
- Komlos J, Kukkadapu RK, Zachara JM, Jaffe PR. (2007). Biostimulation of iron reduction and subsequent oxidation of sediment containing fe-silicates and fe-oxides: Effect of redox cycling on fe(iii) bioreduction. *Water Res* **41**: 2996-3004.
- Kukkadapu RK, Zachara JM, Fredrickson JK, Mckinley JP, Kennedy DW, Smith SC *et al.* (2006). Reductive biotransformation of fe in shale-limestone saprolite containing fe(iii) oxides and fe(ii)/fe(iii) phyllosilicates. *Geochimica Et Cosmochimica Acta* **70**: 3662-3676.
- Larese-Casanova P, Kappler A, Haderlein SB. (2012). Heterogeneous oxidation of fe(ii) on iron oxides in aqueous systems: Identification and controls of fe(iii) product formation. *Geochim Cosmochim Ac* **91**: 171-186.
- Leang C, Adams LA, Chin KJ, Nevin KP, Methe BA, Webster J *et al.* (2005). Adaptation to disruption of the electron transfer pathway for fe(iii) reduction in geobacter sulfurreducens. *J. Bacteriol.* **187**: 5918-5926.
- Lehours A-C, Rabiet M, Morel-Desrosiers N, Morel J-P, Jouve L, Arbeille B *et al.* (2010). Ferric iron reduction by fermentative strain bs2 isolated from an iron-rich anoxic environment (lake pavin, france). *Geomicrobiology Journal* **27**: 714-722.
- Leung KM, Wanger G, El-Naggar MY, Gorby Y, Southam G, Lau WM *et al.* (2013). Shewanella oneidensis mr-1 bacterial nanowires exhibit p-type, tunable electronic behavior. *Nano Lett.* **13**: 2407-2411.
- Li XM, Liu TX, Li FB, Zhang W, Zhou SG, Li YT. (2012a). Reduction of structural fe(iii) in oxyhydroxides by shewanella decolorationis s12 and characterization of the surface properties of iron minerals. *J. Soils Sediments* **12**: 217-227.

- Li YC, Yu S, Strong J, Wang HL. (2012b). Are the biogeochemical cycles of carbon, nitrogen, sulfur, and phosphorus driven by the "fe-iii-fe-ii redox wheel" in dynamic redox environments? *J Soil Sediment* **12**: 683-693.
- Liang YT, Van Nostrand JD, N'guessan LA, Peacock AD, Deng Y, Long PE *et al.* (2012). Microbial functional gene diversity with a shift of subsurface redox conditions during in situ uranium reduction. *Appl Environ Microb* **78**: 2966-2972.
- Liptzin D, Silver WL. (2009). Effects of carbon additions on iron reduction and phosphorus availability in a humid tropical forest soil. *Soil Biol Biochem* **41**: 1696-1702.
- Liptzin D, Silver WL, Detto M. (2011). Temporal dynamics in soil oxygen and greenhouse gases in two humid tropical forests. *Ecosystems* **14**: 171-182.
- Loeppert RH, Inskeep WP 1996. Iron. In: SPARKS, D. L. (ed.) *Methods of soil analysis. Part 3: Chemical methods*. Madison Wisconsin: Soil Science Society of America.
- Lonergan DJ, Jenter HL, Coates JD, Phillips EJP, Schmidt TM, Lovley DR. (1996). Phylogenetic analysis of dissimilatory fe(iii)-reducing bacteria. *J. Bacteriol.* **178**: 2402-2408.
- Lovley DR. (2011). Live wires: Direct extracellular electron exchange for bioenergy and the bioremediation of energy-related contamination. *Energ Environ Sci* **4**: 4896-4906.
- Mahadevan R, Bond DR, Butler JE, Esteve-Nunez A, Coppi MV, Palsson BO *et al.* (2006). Characterization of metabolism in the fe(iii)-reducing organism *geobacter sulfurreducens* by constraint-based modeling. *Appl. Environ. Microbiol.* **72**: 1558-1568.
- Mallet M, Barthelemy K, Ruby C, Renard A, Naille S. (2013). Investigation of phosphate adsorption onto ferrihydrite by x-ray photoelectron spectroscopy. *J. Colloid Interface Sci.* **407**: 95-101.

- Mckeague JA, Day DH. (1966). Dithionite- and oxalate-extractable Fe and Al as aids in differentiating various classes of soils. *Canadian Journal of Soil Science* **46**: 13-&.
- Merkley ED, Wrighton KC, Castelle CJ, Anderson BJ, Wilkins MJ, Shah V *et al.* (2015). Changes in protein expression across laboratory and field experiments in *Geobacter bemidjensis*. *J. Proteome Res.* **14**: 1361-1375.
- Midgley DJ, Greenfield P, Shaw JM, Oytam Y, Li DM, Kerr CA *et al.* (2012). Reanalysis and simulation suggest a phylogenetic microarray does not accurately profile microbial communities. *Plos One* **7**.
- Mikutta C, Mikutta R, Bonneville S, Wagner F, Voegelin A, Christl I *et al.* (2008). Synthetic coprecipitates of exopolysaccharides and ferrihydrite. Part i: Characterization. *Geochim Cosmochim Acta* **72**: 1111-1127.
- Miller AJ, Schuur EaG, Chadwick OA. (2001). Redox control of phosphorus pools in hawaiian montane forest soils. *Geoderma* **102**: 219-237.
- Minyard ML, Bruns MA, Liermann LJ, Buss HL, Brantley SL. (2012). Bacterial associations with weathering minerals at the regolith-bedrock interface, Luquillo experimental forest, Puerto Rico. *Geomicrobiology Journal* **29**: 792-803.
- Murad E. (2010). Mossbauer spectroscopy of clays, soils and their mineral constituents. *Clay Minerals* **45**: 413-430.
- Nissen S, Liu XX, Chourey K, Hettich RL, Wagner DD, Pfiffner SM *et al.* (2012). Comparative c-type cytochrome expression analysis in *Shewanella oneidensis* strain MR-1 and *Anaeromyxobacter dehalogenans* strain 2CP-C grown with soluble and insoluble oxidized metal electron acceptors. *Biochem. Soc. Trans.* **40**: 1204-U1268.

- Pallud C, Kausch M, Fendorf S, Meile C. (2010). Spatial patterns and modeling of reductive ferrihydrite transformation observed in artificial soil aggregates. *Environ Sci Technol* **44**: 74-79.
- Park B, Dempsey BA. (2005). Heterogeneous oxidation of Fe(II) on ferric oxide at neutral pH and a low partial pressure of O<sub>2</sub>. *Environ Sci Technol* **39**: 6494-6500.
- Parsons CT, Couture R-M, Omeregbe EO, Bardelli F, Greneche J-M, Roman-Ross G *et al.* (2013). The impact of oscillating redox conditions: Arsenic immobilisation in contaminated calcareous floodplain soils. *Environmental Pollution* **178**: 254-263.
- Peretyazhko T, Sposito G. (2005). Iron(III) reduction and phosphorous solubilization in humid tropical forest soils. *Geochim Cosmochim Acta* **69**: 3643-3652.
- Pett-Ridge J, Firestone MK. (2005). Redox fluctuation structures microbial communities in a wet tropical soil. *Appl Environ Microb* **71**: 6998-7007.
- Pett-Ridge J, Silver WL, Firestone MK. (2006). Redox fluctuations frame microbial community impacts on N-cycling rates in a humid tropical forest soil. *Biogeochemistry* **81**: 95-110.
- Raich JW, Schlesinger WH. (1992). The global carbon-dioxide flux in soil respiration and its relationship to vegetation and climate. *Tellus Series B-Chemical and Physical Meteorology* **44**: 81-99.
- Refait P, Abdelmoula M, Trolard F, Génin J-MR, Ehrhardt JJ, Bourrié G. (2001). Mössbauer and XAS study of a green rust mineral; the partial substitution of Fe<sup>2+</sup> by Mg<sup>2+</sup>. *American Mineralogist* **86**: 731-739.
- Regelink IC, Weng L, Koopmans GF, Van Riemsdijk WH. (2013). Asymmetric flow field-flow fractionation as a new approach to analyse iron-(hydr)oxide nanoparticles in soil extracts. *Geoderma* **202–203**: 134-141.

- Reyes I, Torrent J. (1997). Citrate-ascorbate as a highly selective extractant for poorly crystalline iron oxides. *Soil Sci Soc Am J* **61**: 1647-1654.
- Richter K, Schicklberger M, Gescher J. (2012a). Dissimilatory reduction of extracellular electron acceptors in anaerobic respiration. *Appl. Environ. Microbiol.* **78**: 913-921.
- Richter LV, Sandler SJ, Weis RM. (2012b). Two isoforms of geobacter sulfurreducens pila have distinct roles in pilus biogenesis, cytochrome localization, extracellular electron transfer, and biofilm formation. *J. Bacteriol.* **194**: 2551-2563.
- Roden EE. (2006). Geochemical and microbiological controls on dissimilatory iron reduction. *Cr Geosci* **338**: 456-467.
- Roden EE. (2012). Microbial iron-redox cycling in subsurface environments. *Biochem. Soc. Trans.* **40**: 1249-1256.
- Saidy AR, Smernik RJ, Baldock JA, Kaiser K, Sanderman J. (2013). The sorption of organic carbon onto differing clay minerals in the presence and absence of hydrous iron oxide. *Geoderma* **209**: 15-21.
- Scharer M, De Grave E, Semalulu O, Sinaj S, Vandenberghe RE, Frossard E. (2009). Effect of redox conditions on phosphate exchangeability and iron forms in a soil amended with ferrous iron. *Eur J Soil Sci* **60**: 386-397.
- Schwertmann U, Schulze DG, Murad E. (1982). Identification of ferrihydrite in soils by dissolution kinetics, differential x-ray-diffraction, and mossbauer-spectroscopy. *Soil Science Society of America Journal* **46**: 869-875.
- Schwertmann U, Cornell RM 1991. *Iron oxides in the laboratory preparation and characterization.*

- Sexstone AJ, Revsbech NP, Parkin TB, Tiedje JM. (1985). Direct measurement of oxygen profiles and denitrification rates in soil aggregates. *Soil Sci Soc Am J* **49**: 645-651.
- Singer PC, Stumm W. (1970). Acid mine drainage: The rate-determining step. *Science* **167**: 1121-1123.
- Sjöstedt C, Persson I, Hesterberg D, Kleja DB, Borg H, Gustafsson JP. (2013). Iron speciation in soft-water lakes and soils as determined by exafs spectroscopy and geochemical modelling. *Geochimica et Cosmochimica Acta* **105**: 172-186.
- Smith JA, Lovley DR, Tremblay PL. (2013). Outer cell surface components essential for fe(iii) oxide reduction by geobacter metallireducens. *Appl. Environ. Microbiol.* **79**: 901-907.
- Song MK, Luo CL, Li FB, Jiang LF, Wang Y, Zhang DY *et al.* (2015). Anaerobic degradation of polychlorinated biphenyls (pcbs) and polychlorinated biphenyls ethers (pbdes), and microbial community dynamics of electronic waste-contaminated soil. *Sci. Total Environ.* **502**: 426-433.
- Steeffel CI, Vancappellen P. (1990). A new kinetic approach to modeling water-rock interaction - the role of nucleation, precursors, and ostwald ripening. *Geochim Cosmochim Ac* **54**: 2657-2677.
- Stewart BD, Nico PS, Fendorf S. (2009). Stability of uranium incorporated into fe (hydr)oxides under fluctuating redox conditions. *Environ Sci Technol* **43**: 4922-4927.
- Szeinbaum N, Burns JL, Dichristina TJ. (2014). Electron transport and protein secretion pathways involved in mn(iii) reduction by shewanella oneidensis. *Environ. Microbiol. Rep.* **6**: 490-500.
- Thompson A, Chadwick OA, Rancourt DG, Chorover J. (2006). Iron-oxide crystallinity increases during soil redox oscillations. *Geochim Cosmochim Ac* **70**: 1710-1727.

- Thompson A, Rancourt DG, Chadwick OA, Chorover J. (2011). Iron solid-phase differentiation along a redox gradient in basaltic soils. *Geochim Cosmochim Acta* **75**: 119-133.
- Tufano KJ, Benner SG, Mayer KU, Marcus MA, Nico PS, Fendorf S. (2009). Aggregate-scale heterogeneity in iron (hydr)oxide reductive transformations. *Vadose Zone J* **8**: 1004-1012.
- Tveit AT, Urich T, Svenning MM. (2014). Metatranscriptomic analysis of arctic peat soil microbiota. *Appl Environ Microb* **80**: 5761-5772.
- Wang YH, Morin G, Ona-Nguema G, Menguy N, Juillot F, Aubry E *et al.* (2008). Arsenite sorption at the magnetite-water interface during aqueous precipitation of magnetite: Exafs evidence for a new arsenite surface complex. *Geochim Cosmochim Acta* **72**: 2573-2586.
- Weiss JV, Emerson D, Megonigal JP. (2004). Geochemical control of microbial Fe(III) reduction potential in wetlands: Comparison of the rhizosphere to non-rhizosphere soil. *FEMS microbiology ecology* **48**: 89-100.
- Wu LL, Beard BL, Roden EE, Kennedy CB, Johnson CM. (2010). Stable Fe isotope fractionations produced by aqueous Fe(II)-hematite surface interactions. *Geochim Cosmochim Acta* **74**: 4249-4265.
- Wu T, Shelobolina E, Xu H, Konishi H, Kukkadapu R, Roden EE. (2012). Isolation and microbial reduction of Fe(III) phyllosilicates from subsurface sediments. *Environmental Science & Technology* **46**: 11618-11626.
- Zachara JM, Fredrickson JK, Li SM, Kennedy DW, Smith SC, Gassman PL. (1998). Bacterial reduction of crystalline Fe<sup>3+</sup> oxides in single phase suspensions and subsurface materials. *Am Mineral* **83**: 1426-1443.

## CHAPTER 2

### IRON(III) CRYSTALLINITY AND EXTRACELLULAR ELECTRON TRANSFER STRATEGIES OF IRON(III)-REDUCING BACTERIA ARE ALTERED BY REDOX CYCLING IN TROPICAL FOREST SOIL MICROCOSMS<sup>1</sup>

---

<sup>1</sup>Wilmoth, J.L., M.A. Moran and A. Thompson. To be submitted to the *International Society for Microbial Ecology* Journal.

## ABSTRACT

The reactivity of Fe(III)-(oxyhydr)oxides toward microbial Fe(III) reduction is dependent on reactive surface area and solubility, properties that can be altered during redox cycling. Although the role of Fe(III) solubility, reactivity and crystal structure on extracellular electron transfer by model Fe(III)-reducers has been investigated, microbial strategies necessary to access and utilize Fe(III) phases in redox-oscillating soils is poorly understood. We used a soil microcosm incubation of soils from the Bisley Watershed, Luquillo Critical Zone Observatory (LCZO), PR, to investigate the effects of O<sub>2</sub> flux rates on Fe(III)-(oxyhydr)oxide crystallinity and to characterize the activity of respiring Fe(III)-reducing bacteria under redox-oscillating conditions. <sup>57</sup>Fe-Mössbauer spectra show that the crystallinity of Fe(III) in (oxyhydr)oxides (9% of total Fe(III)) increased or a decreased depending on slow or fast oxidation rates, respectively, after exposure to multiple redox cycles. Soil RNA was isolated after multiple redox cycles, depleted of rRNA, then, mRNA was linearly amplified followed by *de novo* assembly of millions of paired-end Illumina reads. We annotated and tested the normalized relative abundance of putative *c*-type cytochrome, pilin, exopolysaccharide, chemotaxis, TCA cycle and carbon degradation transcripts that aligned to reference genomes of *Anaeromyxobacter*, *Geobacter* and *Desulfovibrio*. Our functional analysis suggests that Fe(III)-reducers belonging to these genera are active during Fe(III)-reduction in redox-oscillating tropical soils and that relative abundances of transcripts expected to be important for using native Fe(III)-(oxyhydr)oxides as terminal electron acceptors are affected by O<sub>2</sub> flux rates during redox-cycling. We provide spectroscopic and molecular evidence that native Fe(III)-respiring bacteria are capable of extracellular electron transfer, and potentially adapt using select strategies, to Fe(III)-(oxyhydr)oxides that undergo changes in crystallinity and reactivity during soil redox cycling.

## INTRODUCTION

The impact of redox cycling on Fe(III) mineral transformations and molecular mechanisms of extracellular electron transfer by Fe(III)-reducing microorganisms (e.g. *c*-type cytochromes, electrically conductive pili, biofilms and chemotaxis proteins) is environmentally relevant (Coby *et al.*, 2011; Richter *et al.*, 2012a; Parsons *et al.*, 2013; Smith *et al.*, 2013), especially in soils where mineral-microbial interactions govern nutrient and C cycling (Pett-Ridge *et al.*, 2006; Li *et al.*, 2012). Characterizing the interactions that arise between coevolving mineral and microbial species in redox-oscillating soils poses many analytical challenges when compared to model systems. In soils, Fe(III) atoms are distributed across solid phases with a continuum of crystalline order that in turn gives rise to a distribution in Fe(III) reactivity toward reductive dissolution (Bigham *et al.*, 1978; Hansel *et al.*, 2004; Pallud *et al.*, 2010; Thompson *et al.*, 2011; Sjöstedt *et al.*, 2013). Many different microbial taxa have the ability to reduce Fe(III) in soils and display a complex biological suite of extracellular electron transfer strategies. Modeling of microbial Fe(III) reduction kinetics in the lab (Roden, 2006; Bonneville *et al.*, 2009), and genome sequencing of model organisms such as *Geobacter sulfurreducens* (Mahadevan *et al.*, 2006), have elucidated select aspects of Fe biogeochemistry as they may occur in nature, however detailed studies of more environmentally relevant systems are lacking. Next generation RNA-sequencing (RNAseq) offers insight into the soil metatranscriptome of Fe(III)-reducers during prevailing conditions at near-instantaneous resolution with respect to activity, as the turnover rate of mRNA molecules is on the order of seconds to minutes (Gifford *et al.*, 2011). RNAseq analysis of Fe(III) reduction mechanisms during soil redox cycling remains a challenge in microbial ecology due in part to the presence of degraded organics, fermentation byproducts and metal cations that interfere with RNA isolation, purification and

cDNA library construction (Tveit *et al.*, 2014). Despite such difficulties, evaluating mechanistic coupling between changes in Fe(III) crystallinity/reactivity and the strategies of Fe(III)-reducers to utilize extracellular forms of Fe(III) during soil redox transitions will improve our conceptual model of biogeochemical cycling at the ecosystem level.

In surface soils, redox cycling can be perpetuated by O<sub>2</sub> fluctuations driven by periodic rainfall that infiltrates soil pore spaces (Liptzin *et al.*, 2011). Anoxic and/or O<sub>2</sub>-limited conditions that arise cause certain bacteria to use soluble and insoluble Fe(III) minerals in terminal electron accepting pathways to facilitate growth (Roden, 2012). Over successive alternating oxic and anoxic cycles, Fe(III) minerals can change in crystallinity (Thompson *et al.*, 2006). The exact mechanisms of these crystalline changes have not been comprehensively evaluated in soils (Thompson *et al.*, 2006; Komlos *et al.*, 2007; Scharer *et al.*, 2009). During the synthesis of Fe(III)-(oxyhydr)oxides, slower Fe(II) oxidation rates by O<sub>2</sub> tend to form more crystalline minerals as opposed to faster rates which favor more poorly organized crystalline phases (Carlson and Schwertmann, 1990; Steefel and Vancappellen, 1990; Schwertmann and Cornell, 1991). Oxidative transformations of Fe(II) occurring at the surface of solid Fe(III) phases also lead to the formation of secondary minerals and associated re-crystallization of primary minerals (Park and Dempsey, 2005). The reactive surface area of Fe(III)-(oxyhydr)oxides has been shown to be a dominant, perhaps the most important, constraint on microbial Fe(III) reduction kinetics (Roden, 2006) and is anticipated to be a critical variable dependent on changes in Fe(III) crystallinity during soil redox cycling (Zachara *et al.*, 1998; Tufano *et al.*, 2009; Roden, 2012).

Members of the Delta- and Gammaproteobacteria (e.g. *Geobacter* and *Shewanella*) have been used extensively to gauge microbial activity in Fe(III)-reducing environments and model systems (Childers *et al.*, 2002; Liang *et al.*, 2012; Leung *et al.*, 2013; Embree *et al.*, 2014;

Szeinbaum *et al.*, 2014). Representatives within these groups are specialized with regard to Fe(III) reduction, as they can use insoluble forms of extracellular Fe(III) as terminal electron acceptors coupled to ATP production through the TCA cycle. Other less specialized bacteria that rely on fermentation, as opposed to anaerobic respiration, are not known to derive as much energy during Fe(III) reduction (Lehours *et al.*, 2010). Species of *Geobacter* have gained much attention due to their versatile use of organic C as both electron donor and acceptor, insoluble Fe(III) phases and electrodes as terminal electron acceptors, and remediation of radionuclide and organic pollutants (Lovley, 2011; Richter *et al.*, 2012b). Unlike *Shewanella* and *Geothrix* that can produce soluble electron-shuttles and/or chelating moieties to transfer electrons to extracellular Fe(III), *Geobacter* has been shown to predominantly access extracellular Fe(III) surfaces by direct contact using outer-membrane *c*-type cytochromes, electrically conductive pili (e.g. microbial nanowires) and specialized chemotaxis directed toward Fe(II) generation (Leang *et al.*, 2005; Smith *et al.*, 2013). These features are thought to give *Geobacter* a competitive advantage over other Fe(III)-reducers in soils and sediments (Childers *et al.*, 2002). The model Fe(III)-reducers *Geobacter metallireducens* and *Geobacter sulfurreducens* also grow flagella and form multi-heme *c*-type cytochromes along electrically conductive pili, respectively, when grown on insoluble Fe(III) minerals (Childers *et al.*, 2002; Smith *et al.*, 2013). Many diverse bacteria including *Shewanella* have been shown to use surface cytochromes and electrically conductive pili in a similar manner, although the mechanisms and efficiency of electron transport across such components vary depending on the organism (Gorby *et al.*, 2006; Smith *et al.*, 2013). Cell-surface *c*-type cytochromes and associated Fe(III)-reducing functionality are thought to be poorly conserved among *Geobacter* species, with some species showing selective use of particular enzymes, while others show other unique preferences (Smith *et al.*, 2013). Therefore,

detection and characterization of specific outer-membrane *c*-type cytochromes belonging to specialized Fe(III)-reducers, in particular, offers a direct, well recognized, mechanistic approach to study the pathway of electron transfer between organic C and Fe(III) minerals at the mineral-microbial interface in soils.

Quantitative PCR-based studies of tropical forest soils from Puerto Rico, Luquillo Critical Zone Observatory, indicated that *Geobacter* and *Geothrix* were present at  $10^7$  and *Shewanella* at  $10^6$  cells  $g^{-1}$  soil in samples containing  $10^{12}$  bacterial cells total  $g^{-1}$  soil, however, activity of these organisms was not assessed (DeAngelis *et al.*, 2010). Based on such low cellular abundance estimates of Fe(III)-respiring organisms like *Geobacter*, *Geothrix* and *Shewanella*, Fe(III)-reduction in these highly active tropical soils has been speculated to be the net result of many taxonomically diverse organisms reducing Fe(III) in concert, where both anaerobic fermentation and respiration are expected to be involved. However, the insolubility and inaccessibility of soil Fe(III) pools is expected to limit electron acceptor availability for cell growth, and Fe(III)-reducers using specialized-extracellular electron transfer pathways coupled to higher ATP production through the TCA cycle should have a competitive advantage (Lehours *et al.*, 2010). Even at low cell counts in a diverse community, specialized Fe(III)-reducers like *Geobacter*, *Geothrix* and *Shewanella* might display high levels of activity that are environmentally relevant at the ecosystem-scale, the functionality of which cannot be deduced purely based on analysis of rRNA and/or rRNA genes (DeAngelis *et al.*, 2010; Midgley *et al.*, 2012).

This study explores two hypotheses related to redox-induced changes in Fe(III)-(oxyhydr)oxide crystallinity and the activity of specialized Fe(III)-reducers during soil redox cycles: Hypothesis **(1)**: The crystallinity of soil Fe(III) minerals increases during repeated redox

cycles that are generated by slow rates of Fe(II) oxidation following microbial reduction of Fe(III) minerals; and Hypothesis (2): Specialized (respiring) Fe(III)-reducing species are active during Fe(III)-reduction. Within the scope of these hypotheses, we set out to investigate the molecular strategies of specialized Fe(III)-reducers to interact with and transfer electrons to extracellular Fe(III) in soils. To test our hypotheses, we used incubated soils from the Luquillo Critical Zone Observatory (LCZO), Puerto Rico, that experience frequent shifts between oxic and anoxic conditions in the field (Peretyazhko and Sposito, 2005; Liptzin *et al.*, 2011). We used variable temperature  $^{57}\text{Fe}$  Mössbauer spectroscopy to evaluate changes in Fe mineral crystallinity and RNAseq of amplified mRNA to investigate the molecular strategies required for extracellular electron transfer to Fe(III).

## MATERIALS AND METHODS

### Sample Collection

Soils were collected from the Bisley Watershed, Luquillo Experimental Forest, Puerto Rico. Geographic coordinates, features and site-specific details including annual precipitation have been reported elsewhere (Hall *et al.*, 2013). The Bisley site is part of the NSF funded Long-Term Ecological Research (LTER) and Luquillo Critical Zone Observatory (LCZO) networks. A bulk sample of approximately 1 kg was excavated between 0 and 10 cm depth at an upland valley position (Peretyazhko and Sposito, 2005). Soil was placed in plastic sampling bags and allowed to air-dry prior to further processing. Crushed soil was passed through a 2 mm sieve and homogenized inside of a plastic sample bag before experiments were performed. Based on prior work, this procedure retains the Fe(III)-reducing capacity of the soil for up to 1 yr (Ginn *et al.*, 2014).

## Redox-Oscillation Treatments

Soils (2 g air-dried bottle<sup>-1</sup>) were incubated in sealed 120 ml dark amber serum bottles (Wheaton) for 31 d and exposed to three 24 hr pulses of air at three different delivery rates (treatments). Each treatment consisted of three replicates (trt=3, rep=3, n=9). The experiment was initiated as follows: The dry soil was placed in the serum bottles, which were then evacuated and filled with N<sub>2</sub> (x2 cycles) and finally with mixed 10% H<sub>2</sub>:90% N<sub>2</sub> (x1 cycle) before transferring to an anoxic glove chamber (Coy Labs; 4% H<sub>2</sub>:96% N<sub>2</sub>). Once in the chamber, 20 ml of anoxic 25 mM(MES + KCl) buffer (pH 6) was added to each bottle and the suspension sealed with a grey butyl stopper and aluminum crimp cap. Soil suspensions (microcosms) were mixed at 200 rpm on a rotary shaker within the anoxic chamber. After 7 d of anoxic incubation, air was pulsed into each microcosm over a 7 h period at a rate of either 1, 10 or 100 ml hr<sup>-1</sup> [21% O<sub>2</sub> air]<sub>atm</sub>. These O<sub>2</sub> addition rates will from this point on be referred to as *slow*, *medium*, and *fast* treatments respectively, denoting the relative rate at which Fe(II) was oxidized in each treatment. In total, 0.066, 0.66, and 6.6 mmol trt<sup>-1</sup> of O<sub>2</sub> (33, 3.3 x 10<sup>2</sup> and 3.3 x 10<sup>3</sup> mmol kg<sup>-1</sup> net O<sub>2</sub> added to soil) were injected during the initial 7 h of oxidation for the slow, medium and fast oxidation treatments, respectively. Based on a stoichiometric consumption of O<sub>2</sub> by Fe(II) oxidation to form Fe(III) (4 mol Fe(II) oxidized per mole O<sub>2</sub>), the net O<sub>2</sub> injected was sufficient to oxidize 1.32 x 10<sup>2</sup>, 10<sup>3</sup> and 10<sup>4</sup> mmol kg<sup>-1</sup> Fe(II) in the slow, medium and fast treatments respectively. After 24 hr under oxic conditions, all microcosms were moved into the anoxic chamber where all treatment caps and stoppers were removed and discarded; detectable O<sub>2</sub> levels in the anoxic chamber were allowed to drop below 1 ppm; and then the anoxic gas evacuation/fill sequence described above was repeated before resealing the bottles with new stoppers and caps inside the anoxic chamber.

## Incubation Sampling Scheme

Total elemental Fe concentration of the air-dried starting material was determined by lithium(Li)-metaborate fusion and digestion (ALS Minerals) prior to incubation. During incubation, 1 ml aliquots of the microcosm suspensions were collected using sterile 10 ml plastic syringes fitted with wide bore (16 ga; 1.2 mm id; sterile stainless steel) needles for Fe(II) chemical analysis at 0 d, at the end of each 7 d anoxic period, and after 1, 3 and 24 h during each oxic period. We also collected samples for Mössbauer spectroscopy (MBS) analysis at the 24 h point of the last oxic period. Soil suspensions remaining in microcosms at the end of the experiment (31 d) were collected for RNA analysis. For consistency, all sampling was performed in the anoxic chamber, which necessitated that for sampling during oxic periods the microcosms were moved temporarily into the anoxic chamber—without removing the seals. During sampling, sealed microcosms were first over-pressured by injection with anoxic chamber gas using an equal 1 ml volume to match the 1 ml suspension aliquot to be removed. Suspension samples for Fe(II) analysis were placed in 2 ml micro-centrifuge tubes fitted with rubber o-ring cap seals and the tubes were sealed inside the anoxic chamber before being transferred outside the anoxic chamber for centrifugation at 21,000 x g for 15 min to separate the aqueous and solid fractions. After centrifugation the samples were brought back into the anoxic chamber for collection of the aqueous phase and subsequent extraction of the remaining soil pellet with 0.5 M HCl (see below). Each separated aqueous phase was acidified in the anoxic chamber with trace-metal grade 7 M HCl (7 µl per 0.5 ml sample) and stored in a clean sealed micro-centrifuge tube in the dark. The soil pellet remaining after removal of the aqueous phase, was resuspended in 1 ml of 0.5 M HCl (trace metal grade) and vortexed on medium-high speed for 2 h in the dark. After extraction the tubes were centrifuged as previously described, and the acid supernatant was removed inside the

anoxic chamber and stored in a clean micro-centrifuge tube in the dark. The extracted soil pellets were dried on a hotplate at 90°C for 48 h and the final mass recorded. The total volume and mass of suspension components removed during each sample-point were recorded, including solution densities of the aqueous buffer and HCl, to calculate the system mass in each microcosm and Fe(II) concentrations. The ferrozine method was used to quantify Fe(II) in acidified aqueous and HCl extracts (Thompson *et al.*, 2006).

### Mössbauer Spectroscopy

Samples collected under oxic conditions for MBS at 24 d during the incubation were centrifuged as previously described and the supernatants subsequently removed in the anoxic chamber. Soil pellets remaining in o-ring-lid micro-centrifuge tubes were sealed under anoxic headspace and stored at -80°C until further analysis. Frozen samples were transferred to the anoxic chamber where rapid thawing occurred and the resulting highly viscous gel was used to prepare MBS mounts. For each treatment, replicate soil gels were mixed (180 mg total equivalent dry mass mount<sup>-1</sup>) within the cavity of a thin nylon ring and sealed between two layers of Kapton tape. MBS measurements always began immediately at 4.5 K to mitigate potential changes in mineralogy. <sup>57</sup>Fe Mössbauer absorption spectra of the air-dried soil and sampled incubation soils were collected in transmission mode with a variable temperature He-cooled cryostat (Janis Research Co.) and a 1024 channel detector. A <sup>57</sup>Co source (~50 mCi) embedded in a Rh matrix was used at room temperature. Velocity (i.e. gamma-ray energy) was calibrated using  $\alpha$ -Fe foil at 295 K and all center shift (CS) and peak positions are reported with respect to this standard. The transducer was operated in constant acceleration mode and folding to 512 channels was performed to achieve a flat background. Mössbauer spectral fitting was performed using Recoil<sup>TM</sup> software (ISA Inc.) with the Voigt-based fitting (VBF) method of

Rancourt and Ping (1991) for quadrupole splitting distributions (QSDs) and combined hyperfine field distributions (HFDs). The area ratios of sextet lines 1 through 6 were held at 3:2:1:1:2:3 and the linewidth (HWHM) was held at  $0.097 \text{ mm s}^{-1}$  corresponding to the minimum theoretical natural linewidth of  $^{57}\text{Fe}$ . All Mössbauer parameter definitions and a description of the relevant notation are given in Rancourt and Ping (1991) and Thompson *et al.* (2011).

### RNA Isolation and Sequencing

Samples collected for RNA analysis at 31 d were transferred inside the anoxic chamber directly from microcosms to Nalgene plastic bottles and sealed with a screw-cap over a thick layer of high-vacuum silicone grease applied between the threads of the bottle and cap. The newly sealed samples from each replicate per treatment ( $n=9$  sample bottles) were immediately lowered into liquid  $\text{N}_2$  and subsequently stored at  $-80^\circ\text{C}$  until further analysis. Samples were prepared for RNA extraction by fracturing each frozen disc of incubated suspension in the bottom of storage bottles that were embedded in dry ice. A ceramic rod was used to fracture the frozen samples and forceps were used to transfer the coarse frozen fragments to the supplied bead tubes (MoBio) on dry ice before beginning extraction. All equipment, gloves and surfaces were appropriately flamed, wiped with 70% EtOH and sprayed with RNaseZap (Sigma Aldrich) during all procedures. We chose to use only the fast and slow oxidized treatment samples for downstream RNA sequencing and analysis as these treatments likely represented the most biogeochemically informative differences, reserving the medium oxidized samples for evaluation during preliminary extraction trials. Total RNA was extracted from soils using the RNA PowerSoil<sup>®</sup> Total RNA Isolation Kit (MoBio) following the manufacturer's instructions. In trial runs using the medium oxidized replicates, different approaches comparing both separated and intact colloidal suspensions were used to establish the best procedure modifications to extract

RNA from the samples containing both aqueous buffer and soil. We found that the most effective extraction strategy yielding the purest high-yield RNA was to remove the aqueous phase by centrifugation and extract the remaining pellet (1 g dry mass equivalent extraction<sup>-1</sup>). Accordingly, both the fast and slow replicates began the extraction process on dry ice after the frozen fragments had been transferred to bead tubes as described above. A stream of N<sub>2</sub> was used to flush the headspace of each bead tube and then capped to prevent any dramatic redox changes in the steps that follow. Beginning extraction, the sealed N<sub>2</sub>-flushed tubes were alternately moved between ice and brief vortexing to rapidly induce thawing and homogenization. The samples were immediately placed in a 0°C centrifuge and spun at 4,000 x g for 7 min, known to effectively pellet bacterial cells in pure culture, and also used here to prohibit enzymatic activity. Removal of the separated aqueous phase after centrifugation marked the immediate transition to step 1 of total RNA extraction as detailed in the RNA PowerSoil<sup>®</sup> kit user protocol. All mass transfers that occurred before kit extraction were recorded during the procedure to calculate RNA yields on a dry soil basis. RNA yields and purity were measured on a NanoDrop spectrophotometer.

We used the Bacteria Ribo-Zero Magnetic Kit (Epicentre, Illumina) to deplete ribosomal RNA (rRNA) in extracted samples (1 µg starting RNA) (Bhagwat *et al.*, 2014) considering rRNA can make up more than 90% of prokaryotic RNA fractions (He *et al.*, 2010; Gifford *et al.*, 2011; Tveit *et al.*, 2014). Linear amplification of the re-suspended prokaryotic-rRNA-depleted samples was performed using the MessageAmp II-Bacteria Kit (Ambion) to finally enrich for mRNA. Yield and purity of RNA was again checked by spectrophotometer. Fragment size analysis and integrity of the mRNA-enriched samples were checked on a TapeStation 2200 (Agilent). Sequence cDNA libraries were constructed following quality control assessment on a

BioAnalyzer 2100 (Agilent) using the KAPA Stranded RNA-Seq kit (KAPA Biosystems) with TruSeq adapters (Illumina). Libraries were pooled and sequenced on four lanes using the NextSeq platform (Illumina) to generate 150 nt paired-end reads. Library construction, process quality control and sequencing were performed at the Georgia Genomics Facility (GGF).

### Sequence Data Processing and Annotation

Read quality was first evaluated using the program FastQC, and FastQC analysis was again used after each stage of subsequent processing to monitor changes in the dataset. Following initial assessment with FastQC, the program Trimmomatic was used to remove Illumina adapter sequences after manually confirming query-sequence homology with the TruSeq adapters used for library construction. Trimmomatic was also used to improve the average Q score of reads by using the sliding-window function with a 15 nt window and average Q score of 30 to trim at the point of falling below the specified threshold, after which paired reads containing fragments < 50 nt were removed from the dataset. The program Prinseq was then used to trim poly-A/T tails  $\geq 15$  nt from the ends of all read fragments (Tveit *et al.*, 2014) as poly-A extension can be excessive during linear amplification of RNA, and again remaining paired reads with fragments < 50 nt were removed. Assembly of processed reads was performed *de novo* using the open source software Rockhopper 2 (Tjaden, 2015). Rockhopper 2 was also used for statistical testing of differential expression for assembled sequences between the fast and slow oxidation treatments (see below). All assembled sequences from Rockhopper 2 output were converted into a fasta file. The program RiboPicker was used to remove rRNA (16S, 23S, 18S, 28S, 5S and 5.8S units) from the assembled dataset using the program's standalone non-redundant rRNA database (rrnadb) which includes current versions of SILVA, Ribosomal Database Project RDP-II, GreenGenes, NCBI archeal/bacterial complete genomes rRNA and

Rfam databases among others. Alignments for the assembled transcript sequences were performed with BLAST searches against the RefSeq database using BLASTN optimization. MEGAN5 software was used to taxonomically bin sequences and establish an interactive phylogenetic tree of the data based on BLASTN alignments (top hit, bit score  $\geq 50$ ). Sequences of interest were extracted using MEGAN5, concatenated into a fasta file, and the program Blast2GO was used to align and annotate the sequences using BLASTX searches against the RefSeq protein database. Hits were also linked to the corresponding online UniProt database page, comprised of links to related sub-branching databases that included Gene Ontology Consortium (GO terms), Clusters of Orthologous Groups (COG), InterPro, Pfam and KEGG among others. All BLASTX hits presented in the results have  $E$ -values  $\leq 10^{-3}$  unless otherwise indicated. The primary data handling and analyses were conducted through the Linux cluster at the Georgia Advanced Computing Resource Center (GACRC).

The majority of assembled transcripts were binned to prokaryotic genome sequences, with only 6.8% binning to eukaryotic organisms, including fungi and metazoa, and a single bin to the mycobacterium phage AnnaL29. Collector's curves (rarefaction curves) combining the fast and slow oxidation treatment contigs showed that the distribution of active taxa observed at both the phylum and species levels approached a moderate plateau, indicating that the assembled dataset adequately captured microbial diversity across taxonomic ranks (Appx. Fig. 2.1.). None of the assembled transcripts aligned to *Shewanella* reference genomes, and we only detected two transcripts that aligned to *Geothrix*, one of which encoded a vitamin b12-binding protein and the other a band 7 protein that both showed higher relative abundances in the fast oxidation treatment. We thus chose to focus our primary analysis and results only on transcripts that aligned to well-known Fe(III)-reducer reference genomes in Deltaproteobacteria, which included

members of *Anaeromyxobacter*, *Geobacter* and *Desulfovibrio*. More than 90% of all Deltaproteobacteria transcripts, combining both fast and slow oxidation treatments, were binned to these three genera. These sequences comprised several notable strain matches to well-known Fe(III)-reducers including *Anaeromyxobacter dehalogenans* 2CP-C and *Geobacter metallireducens* GS-15 (Appx. Fig. 2.2.) (Nissen *et al.*, 2012; Smith *et al.*, 2013). The prokaryotic contigs were also parsed according to significance based on higher relative abundance in one treatment over another ( $p; q < 0.05$ ) (Appx. Fig. 2.3.). We narrowed our final analysis of the corresponding annotated and assembled transcript sequences to those expected to be important for extracellular electron transfer to insoluble Fe(III)-(oxyhydr)oxides. Transcript contigs that encoded cytochrome, exopolysaccharide, pili, flagella, chemotaxis, carbon degradation, and TCA cycle proteins collectively binning to *Anaeromyxobacter*, *Geobacter* and *Desulfovibrio* were selected as they can give insight into molecular strategies used by Fe(III)-reducers coupled to mineral transformations and the carbon cycle.

### Statistical Analysis

Significance testing of differential relative abundance of contigs between fast and slow oxidation treatments was conducted in Rockhopper 2. We provide a brief description of Rockhopper 2's *de novo* assembly algorithm and data normalization for clarity, as it is relevant to data interpretation and significance testing. Refer to Tjaden (2015) for additional details and discussion of Rockhopper 2's procedures. Rockhopper 2 was used to assemble high quality candidate transcripts *de novo* by first entering all quality-processed paired-end reads and using  $k$ -mers within them to assemble candidate transcript contigs. Both a Burrows-Wheeler index and a de Bruijn graph are used together during assembly, the uniqueness and benefits of which are explained elsewhere (Tjaden, 2015). Second, the assembled transcripts were filtered for high

quality candidate contigs by selecting those sufficiently mapped by perfectly aligned paired-end reads. The resulting filtered assembled transcripts were then tested for differential abundance using only the corresponding perfectly mapped reads. Normalization was performed before statistical testing to account for differences in total reads between replicates and treatments using upper quartile normalization. Upper quartile normalization has been shown to be a robust technique for statistical testing, as it improves the sensitivity of detecting significant differences at low transcript abundances in RNAseq datasets over microarray datasets (Bullard *et al.*, 2010). There is also a positive correlation generally observed between read length and read count for a given transcript that must also be considered (Bullard *et al.*, 2010). This correlation can theoretically lead to overrepresented abundance of longer nt sequences compared to shorter nt sequences when based upon non-normalized read counts. Accordingly, upper quartile normalization, similar to the less sensitive reads/kilobase/million (RPKM) normalization procedure, divides raw read counts by the length of the corresponding assembled transcript in a replicate, but instead divides by the sum of reads under the 75<sup>th</sup> percentile (upper quartile) per replicate, as opposed to the absolute total read count used in RPKM (Bullard *et al.*, 2010; Tjaden, 2015). The key advantage of using upper quartile normalization, and the primary reason it improves sensitivity in statistical testing at low transcript levels, is that the sum of read counts under the upper quartile excludes the top few, most highly abundant transcripts. Alternatively, inclusion of few transcripts at extremely high relative abundance is unsatisfactory for differential testing, because these transcripts may not always be present at the same magnitude between replicates and/or treatments leading to extreme bias in the normalized values, especially affecting those transcripts present at low levels (Bullard *et al.*, 2010). Finally, Rockhopper 2 tests for differences in relative abundance between treatments by using the DESeq algorithm (Anders and

Huber, 2010), locally weighted scatter-plot smoothing (LOWESS) for the variances to be tested, the negative binomial distribution to compute *P*-values, and Benjamini-Hochberg procedure for adjusting *P*-values to *q*-values in order to control the false discovery rate. All transcript relative abundances and statistical differences shown in the results of this study are represented as upper quartile-normalized averages (n=3 reps trt<sup>-1</sup>) reported by Rockhopper 2.

## RESULTS

### Incubation Fe(II) Chemical Analysis

Over the first two anoxic intervals, the net rate of microbial Fe(III) reduction to Fe(II) followed a similar trend for all treatments in both the aqueous and 0.5 M HCl extractable pools (Fig. 2.1.). However, following the third anoxic interval, net Fe(II) concentrations were significantly lower for the slow oxidation treatment than the medium and fast treatments (*p* < 0.001). The total amount of Fe(II) oxidized by the end of the first redox cycle was similar for all treatments in both the aqueous and solid phases. Fe(II) concentration decreased more rapidly, and to a greater extent, under oxic conditions in the medium and fast oxidation treatments by the end of the second redox cycle compared to the slow treatment. Endpoint Fe(II) concentrations throughout the incubation remained similar for all treatments in both the aqueous and solid phases. Microbial reduction of Fe(III) led to continuously increasing amounts of Fe(II) in the solid phase upward of 300 mmol kg<sup>-1</sup>, whereas Fe(II)<sub>aq</sub> concentrations never increased beyond *ca.* 35 mmol kg<sup>-1</sup>. Total elemental Fe was determined to be 1162.5 mmol kg<sup>-1</sup> soil based on lithium(Li)-metaborate fusion and digestion, meaning that 29% of total soil Fe existed as extractable Fe(II) by the end of the incubation for all treatments.

## <sup>57</sup>Fe Mössbauer Characterization

There were no marked differences in the MBS spectra between the fast and medium oxidized samples at any of the collection temperatures. Consequently, we will hereafter focus on comparisons between the slow and fast oxidation treatments. The MBS spectra of the selected samples show, in general, four distinct Fe populations comprising two quadrupole (Q) sites of paramagnetic Fe(III) and paramagnetic Fe(II), and two hyperfine distribution (HFD) sites of magnetically ordered Fe(III) (Murad, 2010) (Fig. 2.2. and Appx. Table 2.1.). The Fe(III)-(oxyhydr)oxide hyperfine site (HFD-OxHy) that gives rise to relatively sharp sextet lines is similar to that of nano-goethite (Thompson *et al.*, 2006). The other hyperfine site displaying a very broad spectral line (HFD-(b)OxHy) most likely arises from more poorly ordered Fe(III)-(oxyhydr)oxide crystals near their blocking temperature (Wu *et al.*, 2012). The paramagnetic sites can theoretically represent Fe populations associated with disordered crystalline phases above their blocking temperature and/or displaying superparamagnetism, surface bound Fe, isomorphic substitutions in clay minerals or organo-metallic assemblages (Kukkadapu *et al.*, 2006; Mikutta *et al.*, 2008; Wu *et al.*, 2012). All the samples show a corresponding increase in sextet area as a function of decreasing temperature, indicating that highly disordered phases continue to magnetically order down to 4.5 K. Because the most ordered crystalline phases display a sextet at higher temperatures, and considering that the remaining sextet parameters (e.g.  $B_{\text{hf}}$  and quadrupole splitting (QS) values) in our spectra are very similar between samples, we use the sextet area at 140 K to compare changes in Fe(III) mineral crystallinity between treated samples. We interpret proportional increases or decreases in sextet area between treatments at 140 K as representing samples with more or less average crystallinity respectively, due to treatment effects. At 140 K, the sample exposed to slow oxidation has 47.6% of its spectra

contained in a sextet, whereas the fast oxidation sample has only 30.0% of its spectra contained in a sextet. Thus, we interpret that the slow oxidized sample contains a more highly ordered (i.e. more crystalline) Fe(III)-(oxyhydr)oxide population than the fast oxidized sample at the end of the incubation. We further show that there was an increase of 8.6% in the 140 K sextet area for the slow treatment compared to the starting material, and 9.0% decrease for the fast treatment compared to the starting material, confirming that the relative difference in crystallinity (nearly 105 mmol kg<sup>-1</sup> Fe(III); 9% total soil Fe) between the treatments had occurred due to both fast and slow Fe(II) oxidation rates during the incubation. It is also worth considering that a very small portion of Fe(II)<sub>aq</sub> remained in solution (12 mmol kg<sup>-1</sup>) for the slow treatment (Fig. 2.1.) that was removed from the MBS analysis of the separated solid phase. However, this amount is negligible when comparing Fe populations between treatments as it only accounts for 1% of the total Fe in the soil. The Fe(II) populations detected in the slow oxidation sample are unique in the fact that we can model the fraction of Fe(II) (HFD-Fe<sup>II</sup>) that displays weak magnetic ordering at 4.5 K (Kukkadapu *et al.*, 2006) (Fig. 2.2.). Of the total amount of Fe(II) remaining in the slow treatment after the last oxic interval, 67% of the Fe(II) was magnetically ordered at 4.5 K. There are also notable comparisons between the amounts of Fe(II) quantified by MBS and those measured in 0.5 M HCl extractions. The starting material soil contained 76 mmol kg<sup>-1</sup> Fe(II) based on MBS analysis, but less than 5 mmol kg<sup>-1</sup> Fe(II) was extracted by HCl. The fast oxidized sample contained 77 mmol kg<sup>-1</sup> Fe(II) based on MBS much like the starting material, yet 50 mmol kg<sup>-1</sup> was extracted by HCl. The amount of Fe(II) detected by MBS for the slow treatment, however, was equal to the corresponding HCl extractable amount (*ca.* 150 mmol kg<sup>-1</sup> Fe(II)). Considering that for the fast oxidation treatment 77 mmol kg<sup>-1</sup> Fe(II) was detected by MBS and only 50 mmol kg<sup>-1</sup> by HCl, 27 mmol kg<sup>-1</sup> Fe(II) was not susceptible to dissolution in the 0.5 M

HCl extraction. We can estimate the amount of magnetically ordered Fe(II) in the fast oxidation sample, even if we are unable to model it explicitly. The conservative estimated amount is equal to the difference in MBS paramagnetic Fe(II) detected at 140 K and 4.5 K for the fast treatment, which is equal to 2% (or 23 mmol kg<sup>-1</sup>). This estimated concentration of magnetically ordered Fe(II) for the fast treatment is nearly equal to the amount of Fe(II) that was resistant to extraction with 0.5 M HCl for the same treatment by the end of the incubation (27 mmol kg<sup>-1</sup> Fe(II)).

### Fe(III)-reducer Cytochrome Transcripts

We did not characterize RNA from the medium oxidation treatment because the fast and slow oxidation treatments offered the most distinct comparisons. None of the assembled transcripts aligned to *Shewanella* reference genomes, and we only detected two transcripts that aligned to *Geothrix* (see materials and methods). Our final analysis focused only on transcript contigs (Table 2.1.) that aligned to well-known Fe(III)-reducer reference genomes in Deltaproteobacteria, which comprised members of *Anaeromyxobacter*, *Geobacter* and *Desulfovibrio*. We identified a total of 16 cytochrome-related transcripts that binned collectively to *Anaeromyxobacter*, *Geobacter* and *Desulfovibrio* reference genomes, including detection of significant differences ( $p; q < 0.0001$ ) for several transcripts binning to *Anaeromyxobacter* and *Geobacter* between the fast and slow oxidation treatments (Fig. 2.3. and Appx. Table 2.2.). Transcripts encoding *c*-type cytochromes similar to OmcS (Gbem\_1116 and GSU2504) and OmcA/MtrC (Gmet\_0571) that binned to *G. bemidjiensis* and *G. metallireducens* respectively were detected in both the fast and slow oxidation treatments, but at significantly different levels. The relative abundance of the OmcS-like transcript was significantly higher in the slow oxidation treatment, while relative abundance of the OmcA/MtrC-like transcript was significantly higher in the fast oxidation treatment. OmcS is an outer-membrane, multi-heme, *c*-

type cytochrome-surface protein that is part of the geobacter nanowire electron transfer (g-net) family of proteins and has been shown to align along the length of conductive pili in *G. sulfurreducens* when grown on Fe(III)-oxides (Leang *et al.*, 2010). OmcS has primarily been studied in the model organism *G. sulfurreducens*, with no reported homolog of OmcS in *G. metallireducens* (Smith *et al.*, 2013). However, OmcS has five known homologs in *G. bemidjiensis*, one of which is encoded by Gbem\_1116 and has been implicated to be important for the reduction of Fe(III)-citrate, bulk hydrous ferric oxide (HFO) and nano-particulate HFO (Merkley *et al.*, 2015). Deletion mutants that lack *omcS* in *G. sulfurreducens* show a marked decrease in their ability to transfer electrons to electrode surfaces and insoluble Fe(III)- and Mn(IV)-oxides compared to wild-type cells. Deletion of *omcS* has not been shown to decrease the reduction of soluble Fe(III)-citrate, but does cause a slight decrease in the reduction of the humic substance analog AQDS (Richter *et al.*, 2012a). Regarding the OmcA/MtrC (Gmet\_0571) transcript, up-regulation of Gmet\_0571 has previously been shown to have a 16.5 fold increase in *G. metallireducens* when grown on Fe(III)-oxide compared to Fe(III)-citrate (Smith *et al.*, 2013). The Gmet\_0571 gene encodes a *c*-type cytochrome with predicted periplasmic or extracellular localization in *G. metallireducens*, and is reported to contain 26 heme-binding sites (Smith *et al.*, 2013). The protein is related to OmcA and MtrC, multi-heme *c*-type cytochromes that are part of an outer membrane surface complex in *Shewanella oneidensis* important for extracellular electron transfer. *S. oneidensis* mutants with deletions in either *omcA* or *mtrC* show a marked decrease in electron transfer to electrode surfaces and insoluble Fe(III)- and Mn(IV)-oxides (Richter *et al.*, 2012a). In addition to the OmcS- and OmcA/MtrC-like transcripts present in our incubations, we also detected another putative *c*-type cytochrome transcript, binned to *G. bemidjiensis*, that was detected only in the slow oxidation treatment.

We detected a putative *c<sub>551</sub>*-type cytochrome transcript in both the fast and slow oxidation treatments that binned to *Anaeromyxobacter*. The relative abundance of the transcript was significantly higher in the slow oxidation treatment. The cytochrome *c<sub>551</sub>* transcript encodes an enzyme similar to a distinct family of di-heme peroxidases that can be used to reduce H<sub>2</sub>O<sub>2</sub> to H<sub>2</sub>O without forming a semi-stable free radical. In *Pseudomonas aeruginosa*, a similar di-heme peroxidase (PsCCP) located in the periplasm provides protection against toxic peroxides without forming a semi-stable free radical for catalysis (Fulop V, 1995, *Structure Jnl*). The periplasmic, di-heme *c<sub>551</sub>*-type peroxidase of *S. oneidensis*, encoded by *ccpA*, is expressed during anaerobic growth with Fe(III)-citrate or MnO<sub>2</sub> as terminal electron acceptors (Nissen *et al.*, 2012). A *c<sub>551</sub>*-type peroxidase was also shown to be up-regulated in OmcB-deficient *G. sulfurreducens* mutants grown with Fe(III)-citrate as the terminal electron acceptor. OmcB is an outer-membrane *c* type cytochrome important for *G. sulfurreducens* wild-type growth on insoluble Fe(III)-oxide (Leang *et al.*, 2005). The exact role of peroxidase enzymes during growth under anoxic conditions is unclear, but both peroxidase and oxidase enzymes (such as *cbb<sub>3</sub>*-type cytochromes) appear to be important during soluble and insoluble metal reduction by *S. oneidensis*, where *cbb<sub>3</sub>*-type cytochromes are more highly expressed during reduction of insoluble MnO<sub>2</sub>. Higher expression of *cbb<sub>3</sub>*-type cytochromes during reduction of insoluble MnO<sub>2</sub> with *A. dehalogenans* compared to Fe(III)-citrate has also been shown (Nissen *et al.*, 2012). In our study, transcripts encoding enzymes similar to both *c<sub>551</sub>*-peroxidase and *cbb<sub>3</sub>*-oxidase that binned to *Anaeromyxobacter* species showed a higher relative abundance in the slow oxidation treatment. We also detected a putative *c<sub>552</sub>*-type cytochrome, nitrite reductase, transcript in both treatments that binned to *Anaeromyxobacter*, with a significantly higher relative abundance in the slow oxidation treatment. Expression of nitrite reductases has also been reported during growth of *A.*

*dehalogenans* and *S. oneidensis* cells under both Fe(III)-citrate and MnO<sub>2</sub> reducing conditions (Nissen *et al.*, 2012). The study showed that cell cultures of *S. oneidensis* expressed higher levels of an outer-membrane nitrite reductase during reduction of MnO<sub>2</sub>, while *A. dehalogenans* cells expressed higher levels of a periplasmic nitrite reductase during reduction of Fe(III)-citrate. It was suggested that nitrite reductases may alternatively serve as electron transfer intermediates during both Fe(III) and Mn(IV) reduction (Nissen *et al.*, 2012). We note that the physical location (i.e. periplasmic or outer-membrane) of the nitrite reductases may also play a critical role, as the outer-membrane nitrite reductase in *S. oneidensis* in the previous study seems to have been more important for reduction of insoluble MnO<sub>2</sub>. However, we cannot confirm the cellular location of the enzyme encoded by the putative *c*<sub>552</sub>-type nitrite reductase transcript detected in our study. We also detected the significantly higher relative abundance of a putative ResB/cytochrome *c* biosynthesis transcript, and the presence of another putative cytochrome *c* biogenesis transcript, in the slow oxidation treatment that binned to *Anaeromyxobacter*.

Several other putative cytochrome transcripts that binned to *Anaeromyxobacter* and *Desulfovibrio* were detected in our study. Regarding *Anaeromyxobacter*, two transcripts annotated each as multiheme cytochrome *c* showed higher relative abundance in either the fast oxidation or the slow oxidation treatment. Multiheme *c*-type cytochromes are expressed in *A. dehalogenans* during growth with both soluble and insoluble electron acceptors (Nissen *et al.*, 2012). A putative cytochrome *bd* ubiquinol oxidase subunit I transcript was detected only in the slow oxidation treatment. Ubiquinol oxidase has been shown to be up-regulated in OmcB-deficient *G. sulfurreducens* mutants grown with Fe(III)-citrate (Leang *et al.*, 2005). It is unclear what functional role in Fe(III) reduction, if any, was served by the other remaining putative cytochrome *c* transcripts (class III, *c*<sub>554</sub>- and *c*-types) that binned to *Anaeromyxobacter* in our

experiment. Regarding *Desulfovibrio*, we detected putative b5 and lipoprotein multiheme cytochrome *c* transcripts that binned to *D. magneticus*. These transcripts were present in both treatments, but showed higher relative abundances in the fast oxidation treatment. The annotated lipoprotein multiheme cytochrome *c* transcript is similar to that encoded by GSU0702 of *G. sulfurreducens* containing 35 heme-binding sites, and displayed the highest relative abundance in both treatments compared to all other detected cytochrome transcripts. It has been suggested that an important function of multiheme *c*-type cytochromes might be the accumulation and storage of electrons, serving as biochemical capacitors to generate a favorable potential gradient between cell surface components and extracellular electron acceptors (Leang *et al.*, 2010).

#### Pilin, Flagellin, Exopolysaccharide and Chemotaxis Transcripts

We detected several putative type IV pilus assembly transcripts that binned to *Anaeromyxobacter* (Fig. 2.4. and Appx. Table 2.3.). All of the PilA and PilZ transcripts showed higher relative abundance in the slow oxidation treatment. We also detected a significantly higher relative abundance of a PilZ transcript in the slow oxidation treatment. Type IV pili are important for many functions including twitching motility, adhesion, pathogenicity, transformation, biofilm formation, chemotaxis and cell-to-cell (social) coordination. PilA serves as the major protein subunit of helical polymers that make up type IV pili, and PilZ is a type IV regulatory and biogenesis protein (Dunger *et al.*, 2014). Type IV pili composed of PilA polymers in *Geobacter* (i.e. nanowires) are essential for long-range extracellular electron transfer, reduction of insoluble Fe(III)-oxides and graphite anodes, optimal electric current in microbial fuel cells and thick biofilm formation on various surfaces (Richter *et al.*, 2012b). A PilA transcript that was detected in both treatments showed similarity to PilA sequences that contain type II secretion regions in *Finegoldia magna* and *G. lovleyi*. Type II secretion in Fe(III)-

reducers is important for translocation of cellular components across the membrane layers (e.g. for assembly of cell-surface appendages), and deletion of type II secretion genes in *S. oneidensis* leads to lower expression of OmcA and MtrC surface cytochromes that are needed for Fe(III) reduction (Shi *et al.*, 2008). To our knowledge, no relevant characterizations of *Anaeromyxobacter* have yet been conducted regarding involvement of PilA and PilZ in Fe(III)-reduction. Our results indicate that both type II secretion/PilA and PilZ expression, based on transcripts that binned to *Anaeromyxobacter*, was important during Fe(III)-reducing conditions in the incubated soils. As mentioned above, type IV pili are also important for the formation of biofilms that can facilitate close proximity of cells to the surface of extracellular electron acceptors. We detected the significant relative abundance of a putative exopolysaccharide synthesis transcript and presence of a putative polysaccharide deacetylase transcript in the slow oxidation treatment. Expression of both transcripts could be important for the formation of biofilms, and it was recently shown that deacetylases in Proteobacteria are important for maintaining the adhesion of cells to extracellular surfaces (Wan *et al.*, 2013). A putative flagellin FlgL transcript was detected only in the fast oxidation treatment that binned to *Geobacter* (Fig. 2.4.). Up-regulation of an FlgL coding gene in *G. metallireducens* (Gmet\_0439) has also been shown to have a 52.7 fold increase when grown with Fe(III)-oxide compared to Fe(III)-citrate (Smith *et al.*, 2013). Three putative CheY chemotaxis transcripts that binned to *Anaeromyxobacter* were only detected in the slow oxidation treatment in our study. CheY is the response regulator in a two-component signal transduction system, including CheA, used to induce cellular movement during reaction to environmental stimuli. Deletion of *cheA-3*, a gene necessary for behavioral response during Fe(III)-reduction in *S. oneidensis*, causes loss of reversed flagellar rotation that is thought to be important for cell sensing of Fe(III)/(II) and

congregation in the vicinity of extracellular electron acceptors during anaerobic growth (Harris *et al.*, 2012).

### Carbon Degradation Transcripts

We selected transcript sequences that may be linked to the degradation of environmentally relevant C sources (i.e. C sources with some likelihood of originating from outside the cell) for further analysis (Fig. 2.5. and Appx. Table 2.4.). We excluded transcripts that most likely encode enzymes for amino acid C degradation for example, because there is no definitive way in our study to tell whether or not this type of C comes from outside the organism for respiration or is part of the organism's intracellular amino acid turnover. We detected five putative C degrading transcripts that binned to *Anaeromyxobacter* including protein annotations for an aromatic hydrocarbon/outer-membrane porin, an extradiol dioxygenase, a 2-nitropropane dioxygenase, a lactate permease and a chitinase. These transcripts showed higher relative abundance in the slow oxidation treatment with significant differences for the putative aromatic hydrocarbon/outer-membrane porin, 2-nitropropane dioxygenase and chitinase transcripts. We also detected a putative ATZ/TRZ chlorohydrolase transcript that binned to *Geobacter*, which showed the highest relative abundance of all selected C degradation transcripts in the slow oxidation treatment. Proteins necessary for the degradation of aromatic hydrocarbons (a class of relatively stable organic C species) under Fe(III)-reducing conditions have been shown to be important for the removal of benzene in contaminated environments (Zhang *et al.*, 2014). Extradiol dioxygenases are used by bacteria that take part in lignin-degradation pathways. The bacterium *Sphingobium* sp. SYK-6, a member of the Proteobacteria, uses extradiol 4,5-dioxygenase LigAB for aromatic ring-opening during metabolism of lignin-derived compounds (Barry *et al.*, 2015). Nitro compounds, such as 2-nitropropane, are used for industrial products

including solvents, fuels and chemical intermediates, but can also be produced naturally by certain plants. The toxic compound 2-nitropropane is an additive in solvents that is known to cause mutagenesis in bacteria and is a powerful hepatocarcinogen in rats. The enzyme 2-nitropropane dioxygenase breaks down nitro-compounds and is unique in that it splits the dioxygen pair of the nitro-group and incorporates each oxygen atom into one of two separate products including HNO<sub>2</sub> (rather than incorporating oxygen into just one product) (Gorlatova *et al.*, 1998). Lactate permeases are required for uptake of lactate into the cell to carry out respiration, and lactate is often used as a model electron donor for Fe(III)-reducing bacteria during anaerobic growth in soils (Song *et al.*, 2015). Chitin is an integral protein component of the cell walls of fungi and nematodes in soil. Chitinase enzymes are used by some soil bacteria to break down and metabolize chitin for growth (Cretoiu *et al.*, 2015). Chlorohydrolase ATZ/TRZ-family enzymes catalyze hydrolytic dechlorination of chlorinated organic compounds (including Atrazine (ATZ), a chlorinated herbicide). The up-regulation of both 2-nitropropane dioxygenase and ATZ/TRZ-family chlorohydrolase genes in an OmcB-deletion mutant of *G. sulfurreducens*, GSU1877 and GSU1708 respectively, was shown during anaerobic growth with acetate as electron donor and Fe(III)-citrate as electron acceptor (Leang *et al.*, 2005).

#### TCA Cycle of *Anaeromyxobacter*

Several transcripts encoding enzymes of the TCA cycle binning to *Anaeromyxobacter* are present in the dataset (Fig. 2.6.(a)). We detected putative *Anaeromyxobacter* transcripts similar to succinate dehydrogenase (EC:6.2.1.5), malate dehydrogenase (EC:1.1.1.37), dihydrolipoamide/pyruvate dehydrogenase complex (EC:2.3.1.12), isocitrate dehydrogenase (EC:1.1.1.42), aconitate hydratase (EC:4.2.1.3) and fumarate hydratase (EC:4.2.1.2). Malate dehydrogenase, dihydrolipoamide/pyruvate dehydrogenase complex, isocitrate dehydrogenase

and fumarate hydratase transcripts were more highly expressed in the slow oxidation treatment ( $p;q < 0.0001$ ) with malate dehydrogenase and fumarate hydratase transcripts showing the highest expression levels (Fig. 2.6.(b) and Appx. Table 2.5.). Only trace expression levels of malate dehydrogenase were detected for the fast oxidation treatment. We also detected a transcript of *Anaeromyxobacter* similar to a 90 aa subunit of F0F1-ATPase (pfam09527) at a higher expression level in the slow oxidation treatment ( $p;q < 0.0001$ ) compared to trace levels in the fast oxidation treatment.

## DISCUSSION

### Redox Induced Fe Chemical and Solid Phase Transformations

We hypothesized that slower rates of Fe(II)-oxidation by  $O_2$  would lead to the formation of more ordered Fe(III) crystals. The MBS data collected at 140 K support this hypothesis, as larger sextet areas at this temperature, representing a higher proportion of more crystalline Fe(III)-(oxyhydr)oxides, were observed for the slow oxidation treatment than for the fast oxidation treatment (Fig. 2.2. and Appx. Table 2.1.). The time under oxic and anoxic conditions were constrained to relatively short durations, because reactive Fe(III) minerals can undergo Ostwald ripening to more crystalline structures under static conditions (Steefel and Vancappellen, 1990; Frierdich *et al.*, 2011). We held the length of time under anoxic conditions consistent between treatments to control for changes in Fe(III)-(oxyhydr)oxide crystallinity during microbial Fe(III) reduction (Fig. 2.1.). Bacteria have been shown to induce changes in Fe(III)-(oxyhydr)oxide crystallinity under static anoxic conditions (Hansel *et al.*, 2005). By using repeated short redox cycles (7:1 anoxic:oxic) equivalent between treatments to control for transformation of iron phases by Fe(II), we demonstrate that the rate of Fe(II)-oxidation during

redox cycling in soils can alter the crystallinity of native Fe minerals. We expected accumulation of more SRO Fe(III) phases would lead to higher levels of Fe(III) reduction in the fast oxidation treatment compared to the slow oxidation treatment. This expectation was in part based on the general observation that a decrease in crystalline order is often associated with an increase in reactive surface area (Steeffel and Vancappellen, 1990; Roden, 2006). However, the Fe(II) concentrations measured at each anoxic time-point for both treatments over the course of the incubation were nearly identical. A possible explanation for the similar anoxic endpoint Fe(II) concentrations between treatments is that by the end of seven days, microbial Fe(III)-reduction generated sufficient amounts of Fe(II) at Fe(III)-(oxyhydr)oxide surfaces to pacify, or insulate from, efficient transfer of electrons to the constituent Fe(III) (Roden, 2006). This explanation is supported by the presence of an Fe(II) phase displaying weak-magnetic ordering at 4.5 K in the slow oxidation MBS sample (Fig. 2.2. and Appx. Table 2.1.), that may arise from adsorbed Fe(II) in close proximity to the  $B_{hf}$  field of neighboring Fe(III) atoms in adsorbent (oxyhydr)oxides. Comparisons between our MBS and chemical extraction data indicate that the estimated Fe(II) of a similar phase in the fast oxidation treatment was less susceptible to 0.5 M HCl extraction. Accordingly, we consider the possibility that these magnetically ordered Fe(II) populations represent the formation of some secondary mineral, rind or mixed-valence feature associated with reduced Fe(III) minerals, such as nano-magnetite or nano-siderite. There was an aqueous Fe(II) saturation level of *ca.*  $35 \text{ mmol kg}^{-1} \text{ Fe(II)}_{aq}$  that would have caused a rapid accumulation of Fe(II) in the solid phase throughout the experiment (Fig. 2.1.). Another possibility is that similar Fe(II) levels, despite changes in Fe(III) crystallinity, reflect the strategies of Fe(III)-reducers to adjust to and capitalize on the availability of diverse Fe(III) terminal electron acceptors during soil redox cycling. Finally, the frequency of redox cycling

used in our study played a major role in regulating the net amount of O<sub>2</sub> accumulation during each oxic interval and the net amount of Fe(II) during each anoxic interval. We expect that structural heterogeneity in intact soils would lead to analogous conditions, where O<sub>2</sub> diffusion rates among adjacent aggregate units would be variable due to aggregate structural features (i.e. size, density, pore space etc.) during oxic conditions and microbial Fe(III) reduction would be initiated during periodic infiltration of rainwater. Similar periods of oxic and anoxic conditions used in this study have been documented in the field (DeAngelis *et al.*, 2010; Liptzin *et al.*, 2011).

#### Specialized Fe(III)-reducers Active in Tropical Soil Microcosms

The qPCR results reported in a recent microarray study of LCZO soils indicated that Fe(III)-reducer abundances in cells g<sup>-1</sup> soil belonging to *Geobacter*, *Shewanella* and *Geothrix* make up less than 1% of total bacterial cells g<sup>-1</sup> soil. Further, microarray results could not confirm the presence of 16S rRNA and rRNA genes from these genera during soil redox cycling (DeAngelis *et al.*, 2010). However, considering the competitive advantage of these organisms over other less specialized Fe(III)-reducers (Smith *et al.*, 2013), we hypothesized that these specialized Fe(III)-reducers would be active during Fe(III)-reduction in LCZO soils. In our incubations, we observed transcripts aligning to *Geobacter* species, including sequence similarities with *G. bemidjiensis*, *G. daltonii*, *G. sulfurreducens* and *G. metallireducens*, but not to *Shewanella* or *Geothrix* under the prevailing redox conditions imposed in the lab. This result is consistent with the observation that *Geobacter* species are highly specialized and competitive toward Fe(III)-reduction in soils and sediments, often representing the predominant species in anoxic subsurface environments (Childers *et al.*, 2002). Many of the transcripts in our study were binned to the species *Anaeromyxobacter dehalogenans* (Appx. Fig. 2.2.). *Anaeromyxobacter*

species have been isolated from a variety of terrestrial environments, where they have now been implicated in Fe(III) and U(VI) reduction (Thomas *et al.*, 2008). Members of this genus have also been shown to utilize a diverse range of organic electron donors and acceptors, similar to that used by *Geobacter* (Nissen *et al.*, 2012). The genome of *Anaeromyxobacter* also indicates that related organisms of the Deltaproteobacteria may have evolved from a common aerobic ancestor (Thomas *et al.*, 2008). In line with this observation, both *Anaeromyxobacter* and *Geobacter* species have recently been shown to live using O<sub>2</sub> as a terminal electron acceptor and contain genes required to survive under oxic conditions (Mahadevan *et al.*, 2006). These observations contradict the past notion that organisms like *Geobacter* are constrained to completely anoxic environments (Mahadevan *et al.*, 2006). The third largest distribution of assembled transcripts within the Deltaproteobacteria in our study binned to *Desulfovibrio*. In addition to the reduction of SO<sub>4</sub><sup>2-</sup> for primary growth, *Desulfovibrio* reduces soluble forms of Fe(III) that can cross the outer cell membrane. Among the query genome nucleotide (nt) matches we observed for *Desulfovibrio* species, *D. magneticus* is a magnetotactic species belonging to Deltaproteobacteria that is capable of forming distinct morphologies of magnetite within the cell under Fe(III)-reducing conditions.

#### Redox Cycling Significantly Alters Relative Abundances of *c*-type Cytochromes in

#### *Anaeromyxobacter* and *Geobacter*

The model genomes of *Anaeromyxobacter dehalogenans* 2CP-C, *Geobacter sulfurreducens* and *Shewanella oneidensis* MR-1 are reported to encode 69, >100 and 40 *c*-type cytochrome genes respectively (Nissen *et al.*, 2012; Richter *et al.*, 2012a; Smith *et al.*, 2013), indicating a large molecular network for diverse electron transfer capabilities. Outer surface and multiheme *c*-type cytochromes are particularly important for extracellular reduction of insoluble

forms of Fe(III). However, outer surface *c*-type cytochromes and functionality are thought to be poorly conserved among *Geobacter* species. Examples include homologous genes shared between *Geobacter sulfurreducens* and *Geobacter metallireducens* that are only essential for insoluble Fe(III) oxide reduction in *Geobacter metallireducens* (Smith et al., 2013). More than half of the *c*-type cytochromes necessary for using insoluble MnO<sub>2</sub> as a terminal electron acceptor by *Anaeromyxobacter dehalogenans* 2CP-C and *Shewanella oneidensis* MR-1 are also used during the reduction of soluble Fe(III)-citrate (Nissen et al., 2012). Despite the complex and largely uncharacterized involvement of *c*-type cytochromes in Fe(III) reduction pathways, several genes have been implicated as being favored for electron transfer to insoluble Fe(III) and Mn(IV) in model systems (Nissen et al., 2012; Smith et al., 2013). We observed the significantly higher relative abundance of putative *c*-type cytochrome peroxidase and biogenesis transcripts binned to *Anaeromyxobacter* in the slow oxidation treatment (Fig. 2.3.). We also detected a *cbb*<sub>3</sub>-type cytochrome oxidase transcript binned to *Anaeromyxobacter dehalogenans* 2CP-C with higher relative abundance in the slow oxidation treatment. Peroxidase enzymes allow organisms to convert O<sub>2</sub> and H<sub>2</sub>O<sub>2</sub> to H<sub>2</sub>O (Ekici et al., 2012). Higher expression of *cbb*<sub>3</sub>-type cytochromes in *Anaeromyxobacter dehalogenans* 2CP-C and *Shewanella oneidensis* MR-1 has been shown during growth on insoluble MnO<sub>2</sub> compared to soluble Fe(III)-citrate (Nissen et al., 2012). The transcript (2\_359) observed at higher relative abundances in our slow oxidation treatment is similar to that encoded by *omcS* of *Geobacter sulfurreducens* (Fig. 2.3.), a gene that has no known homolog in *Geobacter metallireducens* (Smith et al., 2013). Gene *omcS* (GSU2504) encodes an important outer-membrane *c*-type cytochrome OmcS that can be easily sheared from the outer surface of *Geobacter sulfurreducens*, is important for electricity production and has been shown to be expressed during growth with insoluble Fe(III) but not soluble Fe(III)-citrate in

wild-type cells. However, *omcS* had the highest expression levels in an OmcB-deficient mutant of *Geobacter sulfurreducens* during growth with soluble Fe(III)-citrate following mutagenesis and adaptation (Leang *et al.*, 2005). High expression of *omcS* in the mutant over the wild-type under acetate-limiting conditions was concomitant with expression of an Atz/Trz family chlorohydrolase (GSU1708) of unknown function (Leang *et al.*, 2005). We also observed the high relative abundance of a putative Atz family chlorohydrolase transcript that binned to *Geobacter*. The significantly expressed *c*-type cytochrome transcript (148\_9) at higher levels in our fast oxidation treatment is similar to gene GMET\_0571 of *Geobacter metallireducens*. This gene is known to be expressed by at least a two-fold increase during growth with Fe(III) oxide compared to Fe(III)-citrate (Smith *et al.*, 2013). Overall, we observed the expression of putative *c*-type cytochromes likely required for insoluble Fe(III) reduction in both the fast and slow oxidation treatments.

#### Potential for Fe(III)-reducers to Adapt to Changes in Fe(III) Crystal Order

We observed that the majority of putative *c*-type cytochrome, type IV pilin, biofilm, chemotaxis, C degradation and TCA cycle transcripts combined were present predominantly in the slow oxidation treatment that were binned to *Anaeromyxobacter* and *Geobacter* (Fig. 2.3. to 2.6.). In contrast, transcripts that binned to *Desulfovibrio* showed higher cytochrome-transcript relative abundance in the fast oxidation treatment (Fig. 2.3.). Our MBS data suggests the crystallinity of Fe(III)-(oxyhydr)oxide increased as a result of slower Fe(II) oxidation rates during redox cycling (Fig. 2.2. and Appx. Table 2.1.). We expect that an increase in crystalline order is associated with a decrease in reactivity and microbial Fe(III) reduction kinetics (Rodén, 2012). Relevant observations to our study were recently made in a whole-genome microarray analysis of *Geobacter metallireducens* grown with either insoluble Fe(III) oxide or soluble

Fe(III)-citrate under static anoxic conditions, where flagella, pili and chemotaxis transcripts had higher relative abundance during growth on insoluble Fe(III)-oxide (Smith *et al.*, 2013). However, the tolerance and use of O<sub>2</sub> may be limited, and have a direct impact on the persistence of certain Fe(III)-reducers. In our study, the effects of long-term exposure to O<sub>2</sub> were controlled and mitigated in treatments by our selection of redox cycle frequency that used a longer anoxic dwell time compared to the oxic dwell time. Over our 31 d experiment, 28 out of 31 days, or 90% of the total incubation time, was carried out under O<sub>2</sub>-limited and/or anoxic conditions for both treatments. Accordingly, the possibility exists that changes in Fe(III) crystalline order imparted direct adaptive pressure on *Anaeromyxobacter*, *Geobacter* and *Desulfovibrio* to express select transcripts needed for extracellular electron transfer during Fe(III)-reduction in the slow oxidation and fast oxidation treatments. We further show that changes in C degradation and TCA cycle transcript expression are linked to redox cycling in these soils, and may also be coupled to the energy demands of Fe(III)-reducers during reduction of Fe(III)-(oxyhydr)oxides (Fig. 2.5. and 2.6.). We also detected a putative bacterioferritin transcript in the slow oxidation treatment that likely encodes for a ferroxidase (EC:1.16.3.1) in *Anaeromyxobacter sp. K* (locus *AnaeK\_0202*) involved in cellular Fe homeostasis. This ferroxidase is responsible for binding Fe(II), oxidizing it to Fe(III), and subsequently forming an Fe(III)-oxide mineral in the cavity of the protein (Pfam: PF00210). We suspect that this protein was important in the slow oxidation treatment because Fe(II) concentrations were overall more persistent in both the aqueous and solid phases during the incubation. *Anaeromyxobacter* may have used ferroxidase to cope with exposure to relatively higher more prolonged levels of Fe(II) during growth in the slow oxidation treatment than in the fast oxidation treatment.

## CONCLUSIONS

Interactions between Fe(III) minerals and Fe(III)-reducing bacteria in the environment play a critical role in determining the stability of C and availability of plant nutrients. This role is uniquely dynamic in highly active, highly weathered, humid tropical forest soils because of repeated redox cycling occurring as the result of precipitation frequency, OC pulses from overlying vegetation, reactivity of Fe(III)-(oxyhydr)oxides and microbial communities adapted to such conditions. In this study, we conducted a soil microcosm incubation of soils from the Bisley Watershed, Luquillo Critical Zone Observatory (LCZO), PR, to determine the effects of Fe(II) oxidation kinetics on Fe(III)-(oxyhydr)oxide crystallinity by O<sub>2</sub> flux and to characterize the metatranscriptome of specialized Fe(III)-reducing bacteria under redox-oscillating conditions. We find that Fe(III)-(oxyhydr)oxides increase or decrease in crystalline order as a function of slow or fast O<sub>2</sub>-induced Fe(II) oxidation rates respectively after exposure to multiple redox cycles as measured by variable temperature <sup>57</sup>Fe-Mössbauer spectroscopy. We annotated and tested the differential relative abundance of several *c*-type cytochrome, pilin, exopolysaccharide, chemotaxis, TCA cycle and carbon degradation transcripts that aligned to *Anaeromyxobacter*, *Geobacter* and *Desulfovibrio* to establish a better mechanistic, conceptual understanding of how native Fe(III)-reducers potentially interact with soil Fe(III) phases. Functional analysis of the assembled mRNA transcripts supports the role of these organisms to interact with and transfer electrons to Fe(III), perhaps even as an adaptive response to transformations in Fe(III)-(oxyhydr)oxide crystallinity that occur during redox cycling. We show that Fe(III)-reducer mediated C degradation, including aromatic hydrocarbons, chlorinated organics and stable C compounds such as chitin, and metabolism are altered during soil redox cycling. Finally, considering that recent whole genome sequencing and functional analysis of *Anaeromyxobacter*

and *Geobacter* species have uncovered the presence of genes required for the use of O<sub>2</sub> as an electron acceptor and possible evolutionary branching from an ancient aerobic ancestor, our data emphasizes the importance of continued research to elucidate the current role and evolution of these organisms in redox oscillating tropical soils.

#### ACKNOWLEDGEMENTS

We thank Katherine Sandlin and Roger Nilsen of the Georgia Genomics Facility (GGF), Athens, GA for cDNA library construction, Illumina sequencing and consultation. We also acknowledge the Georgia Advanced Computing Resource Center (GACRC) at the University of Georgia (UGA) for Linux system use during meta-data handling and processing. Sequencing was partially funded by the UGA graduate school Innovative and Interdisciplinary Research Award. Important funding was provided through the USDA-AFRI Soil Processes Program, NSF Geobiology and Low-Temperature Geochemistry, and NSF Critical Zone Observatory Programs.

#### LITERATURE CITED

- Anders S, Huber W. (2010). Differential expression analysis for sequence count data. *Genome Biol.* **11**.
- Barry KP, Ngu A, Cohn EF, Cote JM, Burroughs AM, Gerbino JP *et al.* (2015). Exploring allosteric activation of ligab from sphingobium sp strain syk-6 through kinetics, mutagenesis and computational studies. *Arch. Biochem. Biophys.* **567**: 35-45.
- Bhagwat A, Ying, Z., Smith, A. (2014). Evaluation of ribosomal rna removal protocols for salmonella rna-seq projects. *Advances in Microbiology* **4** 25-32.

- Bigham JM, Golden DC, Bowen LH, Buol SW, Weed SB. (1978). Iron-oxide mineralogy of well-drained ultisols and oxisols .1. Characterization of iron-oxides in soil clays by mossbauer-spectroscopy, x-ray-diffractometry, and selected chemical techniques. *Soil Science Society of America Journal* **42**: 816-825.
- Bonneville S, Behrends T, Van Cappellen P. (2009). Solubility and dissimilatory reduction kinetics of iron(iii) oxyhydroxides: A linear free energy relationship. *Geochim Cosmochim Acta* **73**: 5273-5282.
- Bullard JH, Purdom E, Hansen KD, Dudoit S. (2010). Evaluation of statistical methods for normalization and differential expression in mrna-seq experiments. *BMC Bioinformatics* **11**.
- Carlson L, Schwertmann U. (1990). The effect of co<sub>2</sub> and oxidation rate on the formation of goethite versus lepidocrocite from an fe(ii) system at ph-6 and ph-7. *Clay Miner* **25**: 65-71.
- Childers SE, Ciuffo S, Lovley DR. (2002). Geobacter metallireducens accesses insoluble fe(iii) oxide by chemotaxis. *Nature* **416**: 767-769.
- Coby AJ, Picardal F, Shelobolina E, Xu HF, Roden EE. (2011). Repeated anaerobic microbial redox cycling of iron. *Appl Environ Microb* **77**: 6036-6042.
- Cretoiu MS, Berini F, Kielak AM, Marinelli F, Van Elsas JD. (2015). A novel salt-tolerant chitobiosidase discovered by genetic screening of a metagenomic library derived from chitin-amended agricultural soil. *Applied Microbiology and Biotechnology* **99**: 8199-8215.
- Deangelis KM, Silver WL, Thompson AW, Firestone MK. (2010). Microbial communities acclimate to recurring changes in soil redox potential status. *Environ Microbiol* **12**: 3137-3149.

- Dunger G, Guzzo CR, Andrade MO, Jones JB, Farah CS. (2014). Xanthomonas citri subsp citri type iv pilus is required for twitching motility, biofilm development, and adherence. *Mol. Plant-Microbe Interact.* **27**: 1132-1147.
- Ekici S, Pawlik G, Lohmeyer E, Koch HG, Daldal F. (2012). Biogenesis of cbb(3)-type cytochrome c oxidase in rhodobacter capsulatus. *Biochim. Biophys. Acta-Bioenerg.* **1817**: 898-910.
- Embree M, Qiu Y, Shieu WD, Nagarajan H, O'neil R, Lovley D *et al.* (2014). The iron stimulon and fur regulon of geobacter sulfurreducens and their role in energy metabolism. *Appl. Environ. Microbiol.* **80**: 2918-2927.
- Friedrich AJ, Luo Y, Catalano JG. (2011). Trace element cycling through iron oxide minerals during redox-driven dynamic recrystallization. *Geology* **39**: 1083-1086.
- Gifford SM, Sharma S, Rinta-Kanto JM, Moran MA. (2011). Quantitative analysis of a deeply sequenced marine microbial metatranscriptome. *Isme J.* **5**: 461-472.
- Ginn BR, Habteselassie MY, Meile C, Thompson A. (2014). Effects of sample storage on microbial fe-reduction in tropical rainforest soils. *Soil Biol Biochem* **68**: 44-51.
- Gorby YA, Yanina S, Mclean JS, Rosso KM, Moyles D, Dohnalkova A *et al.* (2006). Electrically conductive bacterial nanowires produced by shewanella oneidensis strain mr-1 and other microorganisms. *Proc. Natl. Acad. Sci. U. S. A.* **103**: 11358-11363.
- Gorlatova N, Tchorzewski M, Kurihara T, Soda K, Esaki N. (1998). Purification, characterization, and mechanism of a flavin mononucleotide-dependent 2-nitropropane dioxygenase from neurospora crassa. *Appl. Environ. Microbiol.* **64**: 1029-1033.

- Hall SJ, McDowell WH, Silver WL. (2013). When wet gets wetter: Decoupling of moisture, redox biogeochemistry, and greenhouse gas fluxes in a humid tropical forest soil. *Ecosystems* **16**: 576-589.
- Hansel CM, Benner SG, Nico P, Fendorf S. (2004). Structural constraints of ferric (hydr)oxides on dissimilatory iron reduction and the fate of Fe(II). *Geochim Cosmochim Acta* **68**: 3217-3229.
- Hansel CM, Benner SG, Fendorf S. (2005). Competing Fe(II)-induced mineralization pathways of ferrihydrite. *Environ Sci Technol* **39**: 7147-7153.
- Harris HW, El-Naggar MY, Nealson KH. (2012). *Shewanella oneidensis* Mr-1 chemotaxis proteins and electron-transport chain components essential for congregation near insoluble electron acceptors. *Biochem. Soc. Trans.* **40**: 1167-U1129.
- He SM, Wurtzel O, Singh K, Froula JL, Yilmaz S, Tringe SG *et al.* (2010). Validation of two ribosomal rna removal methods for microbial metatranscriptomics. *Nat. Methods* **7**: 807-U858.
- Komlos J, Kukkadapu RK, Zachara JM, Jaffe PR. (2007). Biostimulation of iron reduction and subsequent oxidation of sediment containing Fe-silicates and Fe-oxides: Effect of redox cycling on Fe(III) bioreduction. *Water Res* **41**: 2996-3004.
- Kukkadapu RK, Zachara JM, Fredrickson JK, McKinley JP, Kennedy DW, Smith SC *et al.* (2006). Reductive biotransformation of Fe in shale-limestone saprolite containing Fe(III) oxides and Fe(II)/Fe(III) phyllosilicates. *Geochimica Et Cosmochimica Acta* **70**: 3662-3676.
- Leang C, Adams LA, Chin KJ, Nevin KP, Methe BA, Webster J *et al.* (2005). Adaptation to disruption of the electron transfer pathway for Fe(III) reduction in *Geobacter sulfurreducens*. *J. Bacteriol.* **187**: 5918-5926.

- Leang C, Qian X, Mester T, Lovley DR. (2010). Alignment of the c-type cytochrome omcs along pili of geobacter sulfurreducens. *Appl. Environ. Microbiol.* **76**: 4080-4084.
- Lehours A-C, Rabiet M, Morel-Desrosiers N, Morel J-P, Jouve L, Arbeille B *et al.* (2010). Ferric iron reduction by fermentative strain bs2 isolated from an iron-rich anoxic environment (lake pavin, france). *Geomicrobiology Journal* **27**: 714-722.
- Leung KM, Wanger G, El-Naggar MY, Gorby Y, Southam G, Lau WM *et al.* (2013). *Shewanella oneidensis* mr-1 bacterial nanowires exhibit p-type, tunable electronic behavior. *Nano Lett.* **13**: 2407-2411.
- Li YC, Yu S, Strong J, Wang HL. (2012). Are the biogeochemical cycles of carbon, nitrogen, sulfur, and phosphorus driven by the "fe-iii-fe-ii redox wheel" in dynamic redox environments? *J Soil Sediment* **12**: 683-693.
- Liang YT, Van Nostrand JD, N'guessan LA, Peacock AD, Deng Y, Long PE *et al.* (2012). Microbial functional gene diversity with a shift of subsurface redox conditions during in situ uranium reduction. *Appl Environ Microb* **78**: 2966-2972.
- Liptzin D, Silver WL, Detto M. (2011). Temporal dynamics in soil oxygen and greenhouse gases in two humid tropical forests. *Ecosystems* **14**: 171-182.
- Lovley DR. (2011). Live wires: Direct extracellular electron exchange for bioenergy and the bioremediation of energy-related contamination. *Energ Environ Sci* **4**: 4896-4906.
- Mahadevan R, Bond DR, Butler JE, Esteve-Nunez A, Coppi MV, Palsson BO *et al.* (2006). Characterization of metabolism in the fe(iii)-reducing organism geobacter sulfurreducens by constraint-based modeling. *Appl. Environ. Microbiol.* **72**: 1558-1568.

- Merkley ED, Wrighton KC, Castelle CJ, Anderson BJ, Wilkins MJ, Shah V *et al.* (2015). Changes in protein expression across laboratory and field experiments in geobacter bemidjiensis. *J. Proteome Res.* **14**: 1361-1375.
- Midgley DJ, Greenfield P, Shaw JM, Oytam Y, Li DM, Kerr CA *et al.* (2012). Reanalysis and simulation suggest a phylogenetic microarray does not accurately profile microbial communities. *Plos One* **7**.
- Mikutta C, Mikutta R, Bonneville S, Wagner F, Voegelin A, Christl I *et al.* (2008). Synthetic coprecipitates of exopolysaccharides and ferrihydrite. Part i: Characterization. *Geochim Cosmochim Acta* **72**: 1111-1127.
- Murad E. (2010). Mossbauer spectroscopy of clays, soils and their mineral constituents. *Clay Minerals* **45**: 413-430.
- Nissen S, Liu XX, Chourey K, Hettich RL, Wagner DD, Pfiffner SM *et al.* (2012). Comparative c-type cytochrome expression analysis in shewanella oneidensis strain mr-1 and anaeromyxobacter dehalogenans strain 2cp-c grown with soluble and insoluble oxidized metal electron acceptors. *Biochem. Soc. Trans.* **40**: 1204-U1268.
- Pallud C, Kausch M, Fendorf S, Meile C. (2010). Spatial patterns and modeling of reductive ferrihydrite transformation observed in artificial soil aggregates. *Environ Sci Technol* **44**: 74-79.
- Park B, Dempsey BA. (2005). Heterogeneous oxidation of fe(ii) on ferric oxide at neutral ph and a low partial pressure of O<sub>2</sub>. *Environ Sci Technol* **39**: 6494-6500.
- Parsons CT, Couture R-M, Omoregie EO, Bardelli F, Greneche J-M, Roman-Ross G *et al.* (2013). The impact of oscillating redox conditions: Arsenic immobilisation in contaminated calcareous floodplain soils. *Environmental Pollution* **178**: 254-263.

- Peretyazhko T, Sposito G. (2005). Iron(III) reduction and phosphorous solubilization in humid tropical forest soils. *Geochim Cosmochim Acta* **69**: 3643-3652.
- Pett-Ridge J, Silver WL, Firestone MK. (2006). Redox fluctuations frame microbial community impacts on n-cycling rates in a humid tropical forest soil. *Biogeochemistry* **81**: 95-110.
- Rancourt DG, Ping JY. (1991). Voigt-based methods for arbitrary-shape static hyperfine parameter distributions in mossbauer-spectroscopy. *Nucl. Instrum. Methods Phys. Res. Sect. B-Beam Interact. Mater. Atoms* **58**: 85-97.
- Richter K, Schicklberger M, Gescher J. (2012a). Dissimilatory reduction of extracellular electron acceptors in anaerobic respiration. *Appl. Environ. Microbiol.* **78**: 913-921.
- Richter LV, Sandler SJ, Weis RM. (2012b). Two isoforms of *Geobacter sulfurreducens* pila have distinct roles in pilus biogenesis, cytochrome localization, extracellular electron transfer, and biofilm formation. *J. Bacteriol.* **194**: 2551-2563.
- Roden EE. (2006). Geochemical and microbiological controls on dissimilatory iron reduction. *Cr Geosci* **338**: 456-467.
- Roden EE. (2012). Microbial iron-redox cycling in subsurface environments. *Biochem. Soc. Trans.* **40**: 1249-1256.
- Scharer M, De Grave E, Semalulu O, Sinaj S, Vandenberghe RE, Frossard E. (2009). Effect of redox conditions on phosphate exchangeability and iron forms in a soil amended with ferrous iron. *Eur J Soil Sci* **60**: 386-397.
- Schwertmann U, Cornell RM 1991. *Iron oxides in the laboratory preparation and characterization.*

- Shi L, Deng S, Marshall MJ, Wang ZM, Kennedy DW, Dohnalkova AC *et al.* (2008). Direct involvement of type ii secretion system in extracellular translocation of shewanella oneidensis outer membrane cytochromes mtrc and omca. *J. Bacteriol.* **190**: 5512-5516.
- Sjöstedt C, Persson I, Hesterberg D, Kleja DB, Borg H, Gustafsson JP. (2013). Iron speciation in soft-water lakes and soils as determined by exafs spectroscopy and geochemical modelling. *Geochimica et Cosmochimica Acta* **105**: 172-186.
- Smith JA, Lovley DR, Tremblay PL. (2013). Outer cell surface components essential for fe(iii) oxide reduction by geobacter metallireducens. *Appl. Environ. Microbiol.* **79**: 901-907.
- Song MK, Luo CL, Li FB, Jiang LF, Wang Y, Zhang DY *et al.* (2015). Anaerobic degradation of polychlorinated biphenyls (pcbs) and polychlorinated biphenyls ethers (pbdes), and microbial community dynamics of electronic waste-contaminated soil. *Sci. Total Environ.* **502**: 426-433.
- Steeffel CI, Vancappellen P. (1990). A new kinetic approach to modeling water-rock interaction - the role of nucleation, precursors, and ostwald ripening. *Geochim Cosmochim Ac* **54**: 2657-2677.
- Szeinbaum N, Burns JL, Dichristina TJ. (2014). Electron transport and protein secretion pathways involved in mn(iii) reduction by shewanella oneidensis. *Environ. Microbiol. Rep.* **6**: 490-500.
- Thomas SH, Wagner RD, Arakaki AK, Skolnick J, Kirby JR, Shimkets LJ *et al.* (2008). The mosaic genome of anaeromyxobacter dehalogenans strain 2cp-c suggests an aerobic common ancestor to the delta- proteobacteria. *Plos One* **3**.
- Thompson A, Chadwick OA, Rancourt DG, Chorover J. (2006). Iron-oxide crystallinity increases during soil redox oscillations. *Geochim Cosmochim Ac* **70**: 1710-1727.

- Thompson A, Rancourt DG, Chadwick OA, Chorover J. (2011). Iron solid-phase differentiation along a redox gradient in basaltic soils. *Geochim Cosmochim Acta* **75**: 119-133.
- Tjaden B. (2015). De novo assembly of bacterial transcriptomes from rna-seq data. *Genome Biol.* **16**.
- Tufano KJ, Benner SG, Mayer KU, Marcus MA, Nico PS, Fendorf S. (2009). Aggregate-scale heterogeneity in iron (hydr)oxide reductive transformations. *Vadose Zone J* **8**: 1004-1012.
- Tveit AT, Urich T, Svenning MM. (2014). Metatranscriptomic analysis of arctic peat soil microbiota. *Appl Environ Microb* **80**: 5761-5772.
- Wan Z, Brown PJB, Elliott EN, Brun YV. (2013). The adhesive and cohesive properties of a bacterial polysaccharide adhesin are modulated by a deacetylase. *Mol. Microbiol.* **88**: 486-500.
- Wu T, Shelobolina E, Xu H, Konishi H, Kukkadapu R, Roden EE. (2012). Isolation and microbial reduction of fe(iii) phyllosilicates from subsurface sediments. *Environmental Science & Technology* **46**: 11618-11626.
- Zachara JM, Fredrickson JK, Li SM, Kennedy DW, Smith SC, Gassman PL. (1998). Bacterial reduction of crystalline fe<sup>3+</sup> oxides in single phase suspensions and subsurface materials. *Am Mineral* **83**: 1426-1443.
- Zhang T, Tremblay PL, Chaurasia AK, Smith JA, Bain TS, Lovley DR. (2014). Identification of genes specifically required for the anaerobic metabolism of benzene in geobacter metallireducens. *Front. Microbiol.* **5**.

## TABLES AND FIGURES

Table 2.1. Extracted, processed and assembled transcript parameters.

<b>Parameter</b>	<b>Avg</b>	<b>±Stdv</b>
<b>Extracted RNA</b>		
RNA $\mu\text{g g}^{-1}$ dry soil	3.07	0.36
<i>Abs</i> 260/280 (RNA purity)	1.9	0.1
aaRNA $\mu\text{g g}^{-1}$ dry soil	26.01	5.50
<i>Abs</i> 260/280 (aaRNA purity)	2.4	0.1
<b>Sequenced &amp; Processed Paired-End Reads</b>		
Reads sequenced ( $10^6$ )	14.187	1.655
Reads after quality processing ( $10^6$ )	10.748	1.170
Predominant read length range (nt)	125 - 150	
<b>Assembled &amp; Filtered Paired-End Reads</b>		
Perfectly aligned, assembled reads ( $10^6$ )	3.904	0.594
Imperfectly aligned, non-assembled reads ( $10^6$ ) removed from subsequent analysis	6.848	1.12
Transcript contigs in assembly (total)	3984	
<b>Removed rRNA Contigs from Assembly</b>		
rRNA contigs removed (total)	315	
rRNA reads mapped to rRNA contigs ( $10^6$ ) not used in subsequent analysis	0.165	0.103
<b>Transcript Contigs Retained for Final Analysis</b>		
Final transcript contigs (total)	3669	
Reads ( $10^6$ ) mapped to final contigs	3.739	0.687

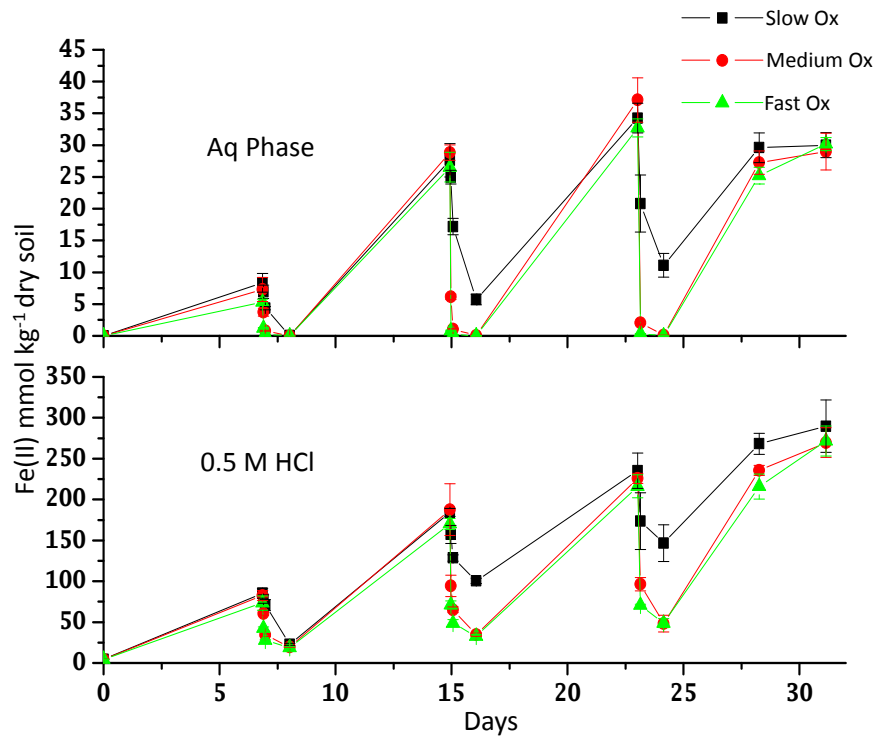


Figure 2.1. Fe(II) concentrations measured in the aqueous (top) and 0.5 M HCl extracted solid (bottom) phases during incubation. Redox cycling followed 7 d anoxic:1 d oxic oscillations throughout. Slow, Medium and Fast oxidation treatments were performed by air injections of 1, 10 and 100 ml hr<sup>-1</sup> over a 7 hr period during oxic conditions. Error bars represent averages  $\pm$ sdev (n=3).

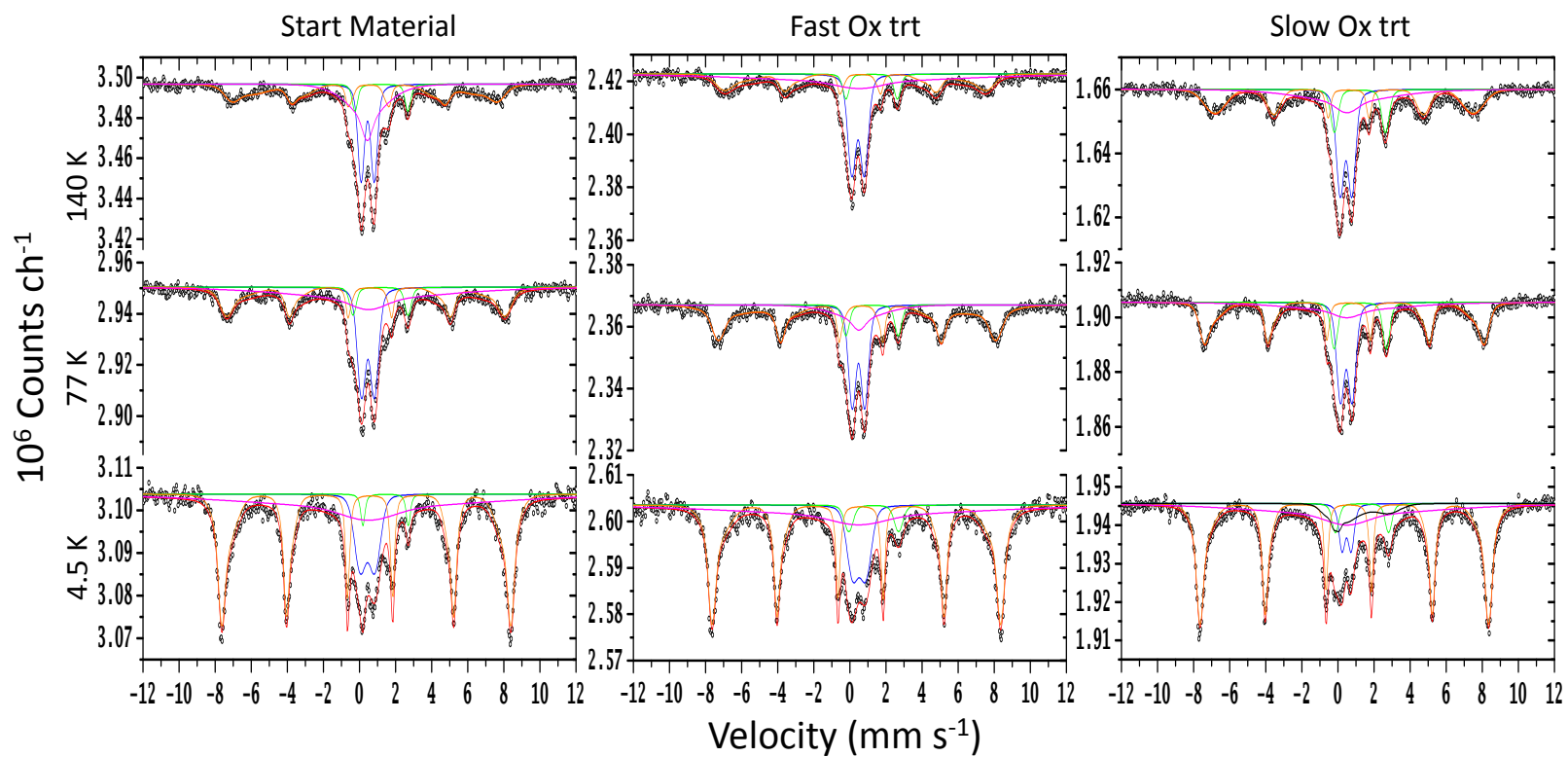


Figure 2.2.  $^{57}\text{Fe}$  Mössbauer spectra collected at 140, 77 and 4.5 K for Starting Material and endpoint samples collected from the Fast and Slow oxidation treatments at 24 d under oxic conditions. Raw spectral data points are shown as black open circles. Modeled Fe site populations are indicated as colored lines: Q-FeIII (blue), Q-FeII (green), HFD-OxHy (orange), HFD-(b)OxHy (violet), HFD-FeII

(black) and total fit (red). Comparison of the samples shows that the slow oxidation treatment spectra display larger, more sharply defined, sextet lines compared to the central Fe(III) doublet at all temperatures. This comparison shows that the slow oxidation treatment bulk Fe-(oxyhydr)oxides underwent increases in crystal order as a function of slower Fe(II)-oxidation during redox cycling.

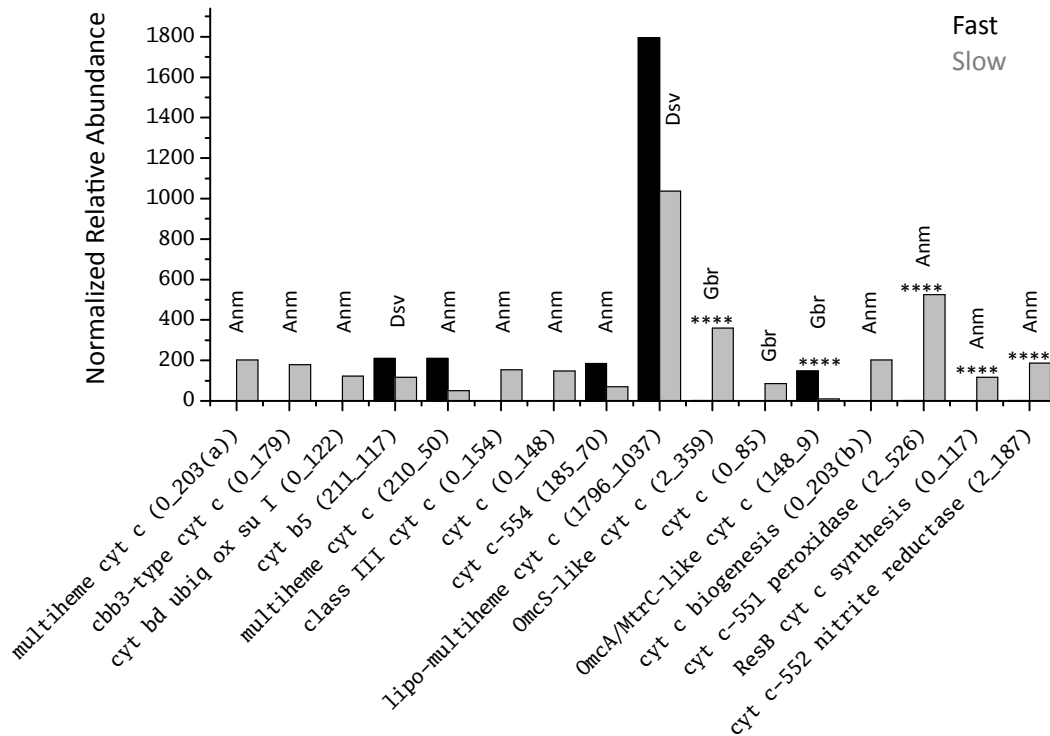


Figure 2.3. Upper quartile normalized, assembled transcripts of putative c-type cytochrome-related sequences showing differential relative abundance between the fast and slow oxidation treatments (\*\*\*\*(p;q < 0.0001)) (n=3) (Rockhopper 2 output). Genus assignments based on BLASTn hits are displayed as abbreviations Anm, Gbr and Dsv (*Anaeromyxobacter*, *Geobacter* and *Desulfovibrio* respectively). X-axis labels of individually distinct (see Results) transcripts indicate putative functionality based on similarity to BLASTx hits in the RefSeq\_proteins database and information provided through links to other databases generated during Blast2GO annotation. Details describing each functional annotation are presented in the Results section and refer to the fast and slow oxidation treatment relative abundances shown here in parenthesis on the x-axis labels.

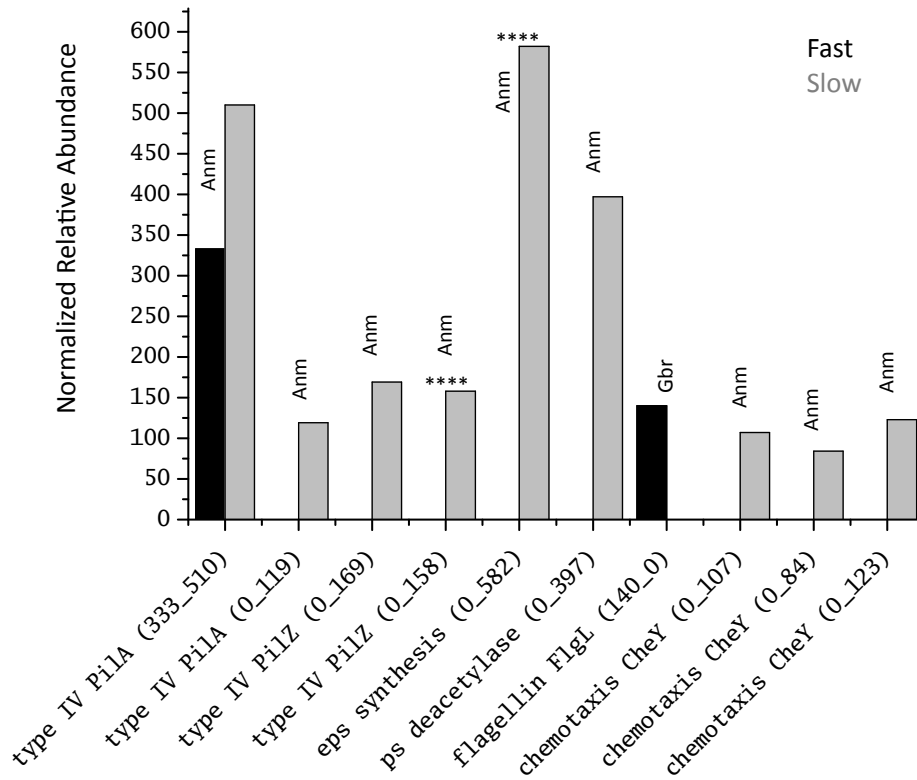


Figure 2.4. Upper quartile normalized, assembled transcripts of putative type IV pilin, flagella, biofilm and chemotaxis related sequences showing differential relative abundance between the fast and slow oxidation treatments (\*\*\*\*(p;q <0.0001)) (n=3) (Rockhopper 2 output). Genus assignments based on BLASTn hits are displayed as abbreviations Anm and Gbr (*Anaeromyxobacter* and *Geobacter* respectively). X-axis labels of individually distinct (see Results) transcripts indicate putative functionality based on similarity to BLASTx hits in the RefSeq\_proteins database and information provided through links to other databases generated during Blast2GO annotation. Details describing each functional annotation are presented in the Results section and refer to the fast and slow oxidation treatment expression levels shown here in parenthesis on the x-axis labels.

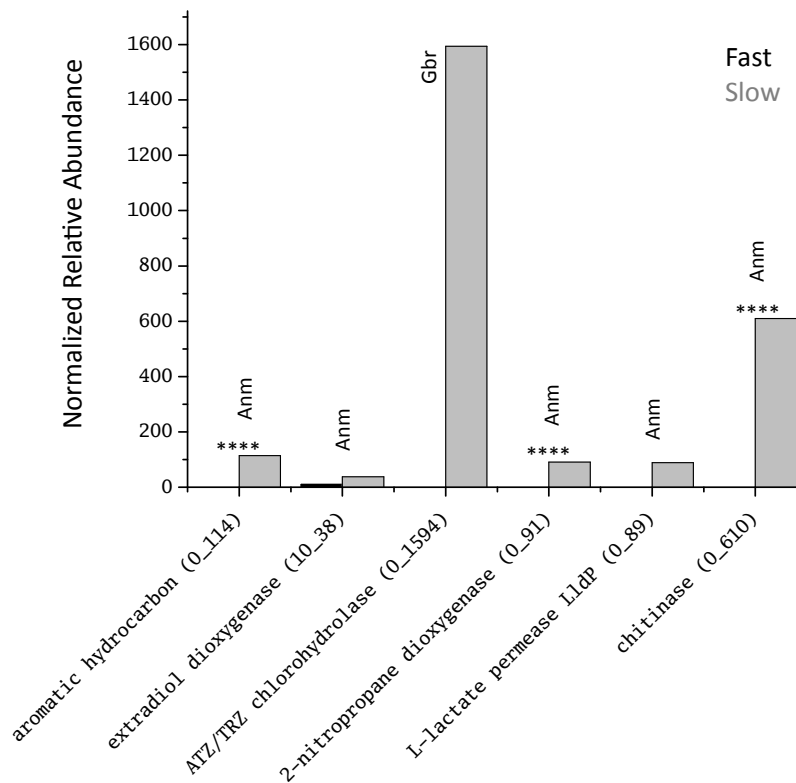


Figure 2.5. Upper quartile normalized, assembled transcripts of putative environmental-C degradation-related sequences showing differential relative abundance between the fast and slow oxidation treatments (\*\*\*( $p; q < 0.0001$ )) ( $n=3$ ) (Rockhopper 2 output). Genus assignments based on BLASTn hits are displayed as abbreviations Anm and Gbr (*Anaeromyxobacter* and *Geobacter* respectively). X-axis labels of individually distinct (see Results) transcripts indicate putative functionality based on similarity to BLASTx hits in the RefSeq\_proteins database and information provided through links to other databases generated during Blast2GO annotation. Details describing each functional annotation are presented in the Results section and refer to the fast and slow oxidation treatment expression levels shown here in parenthesis on the x-axis labels.

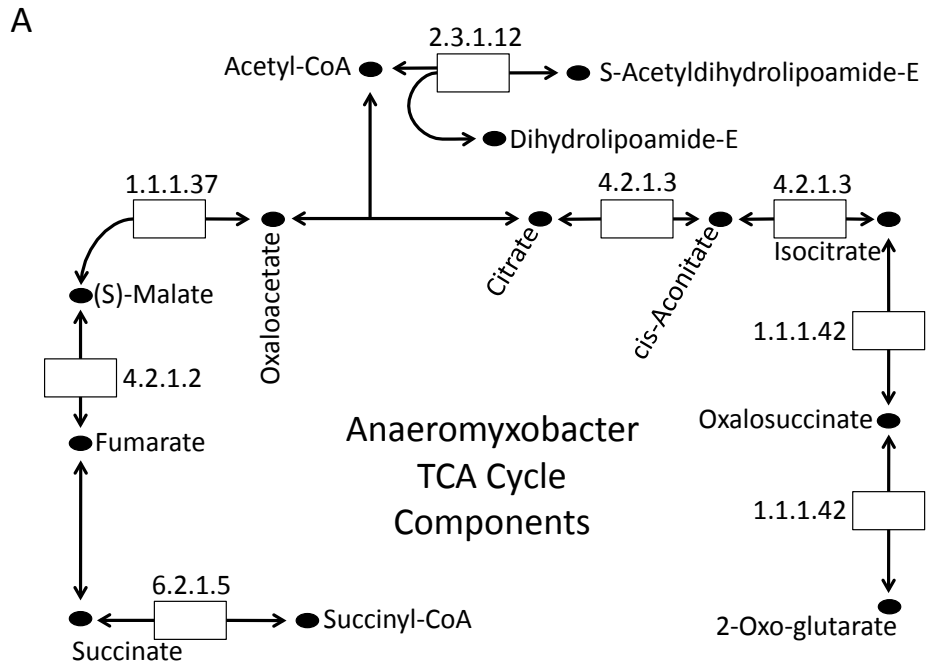


Figure 2.6. See below next figure pane (B) for full description.

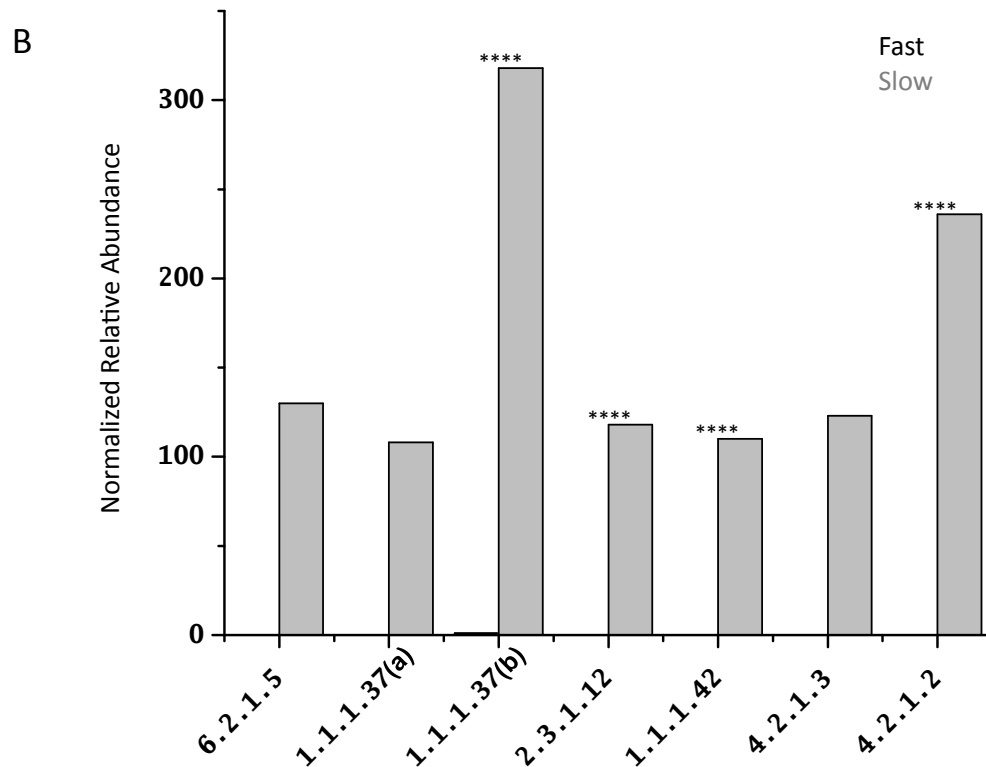
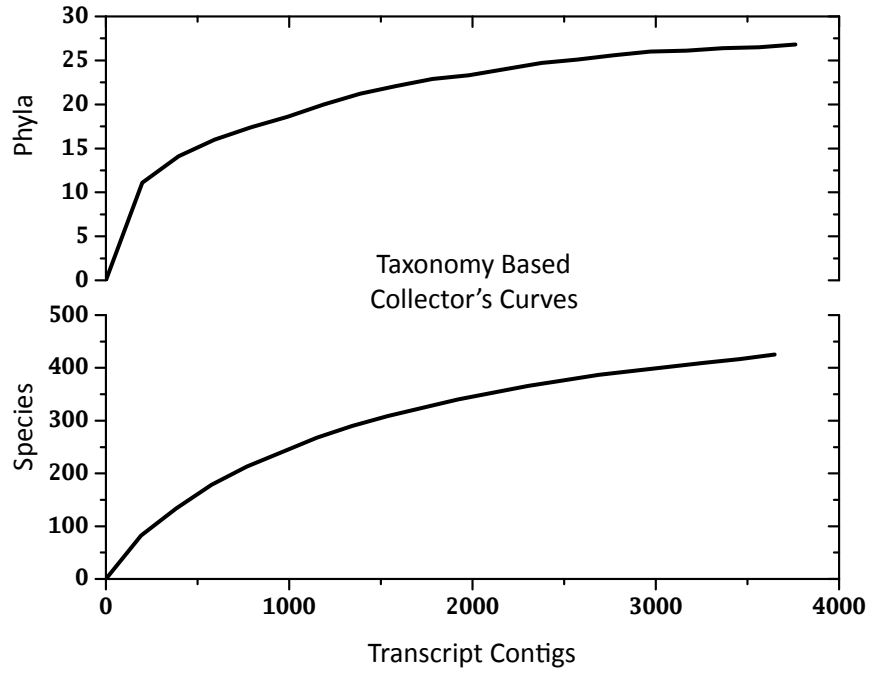
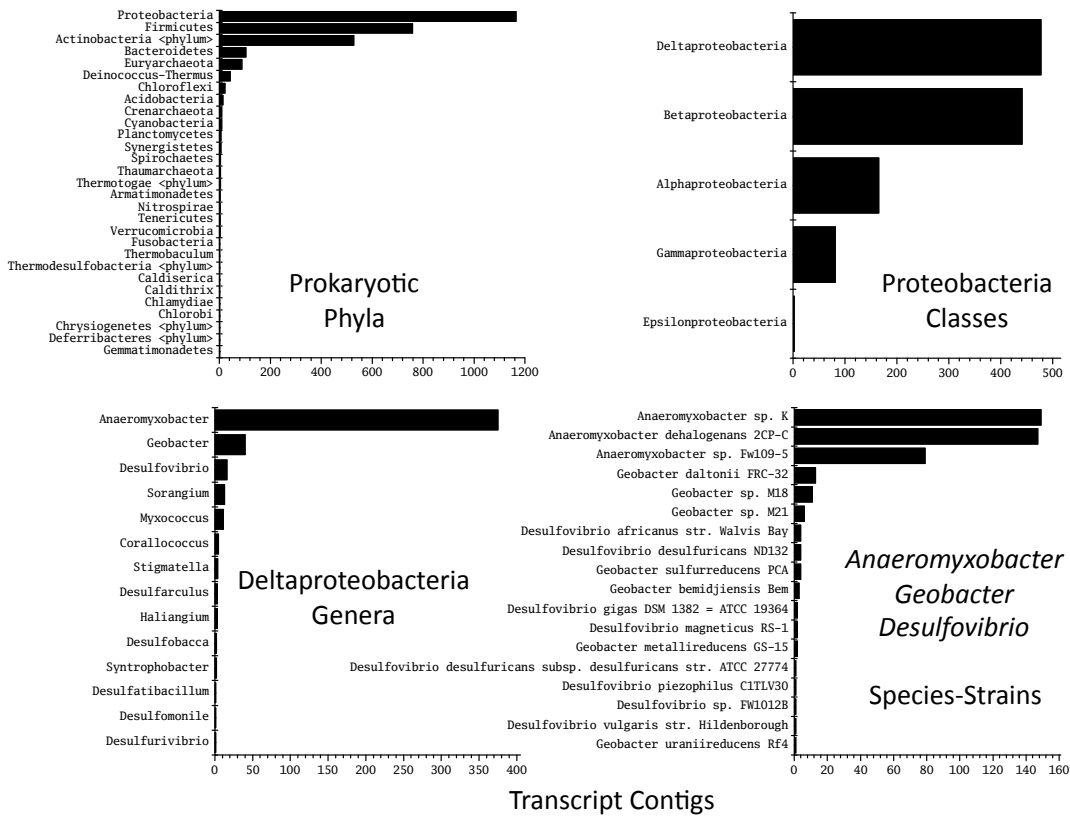


Figure 2.6. (A) Pathway of detected TCA cycle enzyme transcripts binning to *Anaeromyxobacter* (derived from KEGG map 00020, 9/25/14, (c) Kanehisa Laboratories) (B) Upper quartile normalized, assembled transcripts of putative TCA cycle related sequences showing differential relative abundance between the fast and slow oxidation treatments (\*\*\*\*(p;q <0.0001)) (n=3) (Rockhopper 2 output). X-axis labels of individually distinct (see Results) transcripts are shown as enzyme commission (EC) numbers assigned during Blast2GO annotation. Details describing each functional annotation are presented in the Results section and refer to the EC numbers shown here.

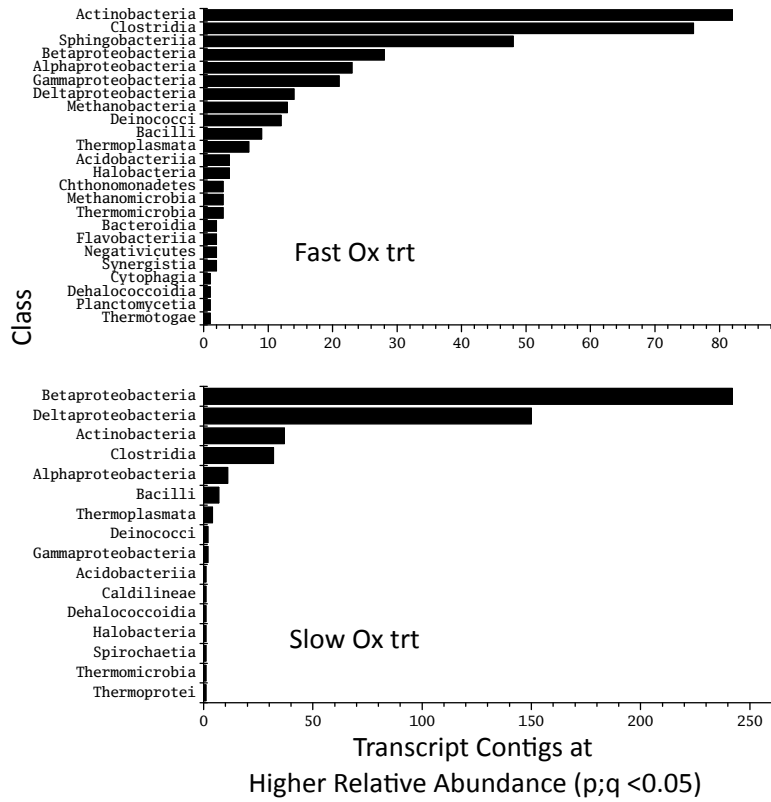
APPENDIX



Appx. Figure 2.1. Taxonomy-based collector's curves at the phylum and species ranks combining assembled transcript contigs from the fast and slow oxidation treatments for each curve.



Appx. Figure 2.2. Count of assembled transcript contigs, from the fast and slow oxidation treatments combined, binning to prokaryotic phyla, by Proteobacteria class, by Deltaproteobacteria genus and to the top three (Fe(III)-reducing) genera at the species-strain level representing *Anaeromyxobacter*, *Geobacter* and *Desulfovibrio*.



Appx. Figure 2.3. Count of assembled transcript contigs that were at significantly higher relative abundance in either the fast or slow oxidation treatment ( $p; q < 0.05$ ) ( $n=3$ ) at the class level that binned to prokaryotes.

Appx. Table 2.1. MBS parameters.

Sample	Temp K	Phase	Spectral Area		$\delta_0$ mm/s	$\epsilon_0$ mm/s	P %	$\Delta$ or H mm/s or T	$\sigma$ mm/s or T	<i>Red- X<sup>2</sup></i>	<CS> mm/s	< $\epsilon$ > mm/s	<QS> or <H> mm/s or T	s.d. mm/s or T
			MC*mm/s	%										
<b>Start Material</b> (2Q, 2H)	140	Q-Fe <sup>III</sup>	0.052(6)	25.8(24)	0.452(74)	n/a	100*	0.724(15)	0.268(32)	0.785	0.452	n/a	0.724	0.266
		Q-Fe <sup>II</sup>	0.013(2)	6.50(87)	1.215(24)	n/a	100*	2.934(47)	0.213(56)		1.215	n/a	2.934	0.213
		HFD-OxHy	0.079(4)	39.0(20)	0.398(32)	-0.103(31)	31.6*	45.75(43)	2.19(73)	0.398	-0.103	41.335	6.099	
		(BG = 3.497 MC/ch)	HFD-(b)OxHy	0.058(6)	28.7(23)	0.433(32)	0*	100*	39.3(21)	6.2(11)	0.433	0	(Peak H 45.39 T)	7.269
<b>Start Material</b> (2Q, 2H)	77	Q-Fe <sup>III</sup>	0.057(2)	28.6(20)	0.470(11)	n/a	100*	0.719(15)	0.384(18)	1.142	0.47	n/a	0.728	0.367
		Q-Fe <sup>II</sup>	0.012(2)	6.08(92)	1.163(27)	n/a	100*	3.05(5)	0.272(66)		1.163	n/a	3.05	0.272
		HFD-OxHy	0.068(7)	34.0(31)	0.462(20)	-0.114(20)	45.43*	47.88(26)	1.80(39)	0.462	-0.114	45.866	4.805	
		(BG = 2.95 MC/ch)	HFD-(b)OxHy	0.063(10)	31.4(37)	0.5*	0*	100*	55(14)	44.2(17)	0.5	0	(Peak H 47.77 T)	28.661
<b>Start Material</b> (2Q, 2H)	4.5	Q-Fe <sup>III</sup>	0.031(3)	14.6(12)	0.443(26)	n/a	100*	0.810(41)	0.559(61)	0.995	0.443	n/a	0.847	0.502
		Q-Fe <sup>II</sup>	0.006(1)	2.71(60)	1.445(33)	n/a	100*	2.516(65)	0.124(96)		1.445	n/a	2.516	0.124
		HFD-OxHy	0.112(4)	51.9(22)	0.483(6)	-0.104(6)	40.73*	49.71(8)	0.81(13)	0.483	-0.104	48.787	2.602	
		(BG = 3.104 MC/ch)	HFD-(b)OxHy	0.066(8)	30.8(26)	0.5*	0*	100*	59(6)	48.15(33)	0.5	0	(Peak H 49.67 T)	43.753

Sample	Temp K	Phase	Spectral Area		$\delta_0$	$\epsilon_0$	P	$\Delta$ or H	$\sigma$	Red- $\chi^2$	<CS>	< $\epsilon$ >	<QS> or <H>	s.d.
			MC*mm/s	%	mm/s	mm/s	%	mm/s or T	mm/s or T		mm/s	mm/s	mm/s or T	mm/s or T
<b>Fast Ox trt</b> (2Q, 2H)	140	Q-Fe <sup>III</sup>	0.049(2)	31.3(22)	0.45(1)	n/a	100*	0.695(14)	0.364(18)	0.636	0.453	n/a	0.703	0.349
		Q-Fe <sup>II</sup>	0.010(2)	6.6(10)	1.207(27)	n/a	100*	2.841(53)	0.267(67)		1.207	n/a	2.841	0.267
(BG = 2.423 MC/ch)		HFD-OxHy	0.047(6)	30.0(30)	0.438(36)	-0.141(35)	51*	45.20(54)	2.5(12)		0.438	-0.141	42.127	5.255
								49(56)	38.9(73)	5.4(38)			(Peak H 44.88 T)	
		HFD-(b)OxHy	0.050(9)	32.0(39)	0.5*	0*	100*	0*	46.3(89)		0.5	0	36.934	27.9
<b>Fast Ox trt</b> (2Q, 2H)	77	Q-Fe <sup>III</sup>	0.041(4)	27.3(25)	0.477(11)	n/a	100*	0.698(16)	0.333(30)	0.671	0.477	n/a	0.702	0.324
		Q-Fe <sup>II</sup>	0.012(2)	7.7(10)	1.231(29)	n/a	100*	2.899(54)	0.288(64)		1.231	n/a	2.899	0.288
(BG = 2.367 MC/ch)		HFD-OxHy	0.076(4)	50.9(27)	0.508(18)	-0.107(18)	44.78*	47.72(19)	1.85(27)		0.508	-0.107	45.295	6.718
								55(6)	43.3(19)	8.4(14)			(Peak H 47.67 T)	
		HFD-(b)OxHy	0.021(5)	14.1(28)	0.5*	0*	100*	0*	11.6(46)		0.5	0	9.29	0.995
<b>Fast Ox trt</b> (2Q, 2H)	4.5	Q-Fe <sup>III</sup>	0.027(3)	15.2(15)	0.516(42)	n/a	100*	0.727(64)	0.55(11)	0.836	0.516	n/a	0.776	0.482
		Q-Fe <sup>II</sup>	0.008(2)	4.6(11)	1.319(62)	n/a	100*	2.76(12)	0.40(13)		1.319	n/a	2.76	0.4
(BG = 2.604 MC/ch)		HFD-OxHy	0.095(4)	54.1(30)	0.477(69)	-0.115(7)	48.38*	49.62(8)	0.93(13)		0.477	-0.115	48.76	2.991
								52(6)	47.95(47)	3.89(48)			(Peak H 49.60 T)	
		HFD-(b)OxHy	0.046(8)	26.1(36)	0.5*	0*	100*	0*	55(15)		0.5	0	43.652	32.98

Sample	Temp K	Phase	Spectral Area		$\delta_0$ mm/s	$\epsilon_0$ mm/s	P %	$\Delta$ or H mm/s or T	$\sigma$ mm/s or T	Red- $\chi^2$	<CS> mm/s	< $\epsilon$ > mm/s	<QS> or <H> mm/s or T	s.d. mm/s or T
			MC*mm/s	%										
<b>Slow Ox trt</b> (2Q, 2H)	140	Q-Fe <sup>III</sup>	0.038(5)	26.8(29)	0.452(9)	n/a	100*	0.652(15)	0.317(32)	0.72	0.452	n/a	0.656	0.307
		Q-Fe <sup>II</sup>	0.018(1)	12.9(11)	1.212(20)	n/a	100*	2.810(36)	0.357(42)		1.212	n/a	2.81	0.357
(BG = 1.66 MC/ch)		HFD-OxHy	0.067(4)	47.6(28)	0.448(27)	-0.133(27)	50.3*	44.76(31)	2.98(61)		0.448	-0.133	40.091	7.368
								50(21)	35.4(39)		7.5(32)			(Peak H 44.49 T)
		HFD-(b)OxHy	0.018(4)	12.7(28)	0.5*	0*	100*	0*	9.1(42)		0.5	0	7.272	5.494
<b>Slow Ox trt</b> (2Q, 2H)	77	Q-Fe <sup>III</sup>	0.045(2)	27.5(15)	0.461(9)	n/a	100*	0.646(13)	0.340(17)	0.841	0.461	n/a	0.653	0.325
		Q-Fe <sup>II</sup>	0.020(1)	12.2(9)	1.238(14)	n/a	100*	2.890(28)	0.295(34)		1.238	n/a	2.89	0.295
(BG = 1.906 MC/ch)		HFD-OxHy	0.068(5)	41.9(22)	0.476(11)	-0.117(11)	48.05*	48.15(16)	1.29(27)		0.476	-0.117	46.587	2.973
								52(16)	45.1(11)		3.34(63)			(Peak H 48.02 T)
		HFD-(b)OxHy	0.030(5)	18.4(28)	0.5*	0*	100*	0*	26.1(82)		0.5	0	20.814	15.73
<b>Slow Ox trt</b> (2Q, 3H)	4.5	Q-Fe <sup>III</sup>	0.001(1)	4.95(72)	0.48*	n/a	100*	0.5*	0.25*	0.966	0.48	n/a	0.504	0.241
		Q-Fe <sup>II</sup>	0.009(2)	4.45(93)	1.334(35)	n/a	100*	2.944(64)	0.282(76)		1.334	n/a	2.944	0.282
(BG = 1.946 MC/ch)		HFD-OxHy	0.101(3)	52.3(24)	0.477(4)	-0.123(5)	52.23*	49.62(6)	0.844(99)		0.477	-0.123	49.108	2.364
								48(59)	48.55(32)		3.21(39)			(Peak H 49.60 T)
		HFD-(b)OxHy	0.057(6)	29.2(25)	0.5*	0*	100*	0*	41.9(71)		0.5	0	33.42	25.25
		HFD-Fe <sup>II</sup>	0.018(5)	9.1(24)	0.90(11)	1*	100*	5.432*	3.859*		0.901	1	5.71	3.434

Appx. Table 2.2. Cytochrome annotations.

BLASTn RefSeq			BLASTx RefSeq & UniProt Hit Information						
Transcript ID	Assembled Length (nt)	Genome	Protein Annotation	<i>E</i>	Sim (%)	Length (aa)	Proteome	Locus/Gene	EC & Database Codes
0_203(a)	3319	<i>A. dehalogenans</i> 2CP-C	multiheme cytochrome <i>c</i>	1.3E-106	58	563	<i>A. dehalogenans</i> 2CP-C	-	pfam09698
0_179	747	<i>A. dehalogenans</i> 2CP-C	cytochrome <i>c</i> , class I; <i>cbb<sub>3</sub></i> -type subunit III domain	1.5E-3	53	97	<i>A. dehalogenans</i> 2CP-C	Adeh_1425	pfam13442
0_122	3383	<i>A. dehalogenans</i> 2CP-C	cytochrome <i>bd</i> ubiquinol oxidase subunit I	8.0E-152	83	448	<i>A. dehalogenans</i> 2CP-1	A2cp1_0997	pfam01654
211_117	298	<i>D. magneticus</i> RS-1	cytochrome <i>b5</i>	2.2E-30	85	75	<i>Desulfarculus sp.</i> SPR	-	-
210_50	1388	<i>A. dehalogenans</i> 2CP-C	multiheme cytochrome <i>c</i>	2.8E-3	32	670	<i>Desulfitobacterium metallireducens</i> DSM 15288	DESME_09155	pfam09699
0_154	291	<i>A. sp.</i> FW109-5	cytochrome <i>c</i> , class III	7.7E-14	83	93	<i>A. sp.</i> FW109-5	Anae109_2108	IPR002322; cd08168
0_148	3050	<i>A. sp.</i> FW109-5	cytochrome <i>c</i>	2.2E-59	45	1329	<i>A. dehalogenans</i>	-	pfam09698
185_70	2736	<i>A. sp.</i> K	cytochrome <i>c</i> , class III; <i>C<sub>564</sub></i> domain; carboxypeptidase regulation domain	4.5E-4	36	904	<i>A. sp.</i> FW109-5	-	pfam13435; pfam13620
1796_1037	3480	<i>D. magneticus</i> RS-1	lipoprotein multiheme cytochrome <i>c</i> ; three heme-binding motifs & 35 heme-binding sites	3.7E-2	60	1916	<i>G. sulfurreducens</i> PCA	GSU0702	pfam09698
2_359	1410	<i>G. bemidjiensis</i> BEM	cytochrome <i>c</i> , OmcS-like	0.0	76	441	<i>G. bemidjiensis</i> BEM	Gbem_1116	-
			OmcS	2.4E-138	63	432	<i>G. sulfurreducens</i>	GSU2504; <i>omcS</i>	TCDB:5.B.3.1.1.
0_85	501	<i>G. bemidjiensis</i> BEM	cytochrome <i>c</i>	5.1E-25	69	321	<i>G. bemidjiensis</i> BEM	-	-
148_9	1231	<i>G. metallireducens</i> GS-15	multiheme cytochrome <i>c</i> ; deca-heme OmcA/MtrC region	2.6E-55	56	1848	<i>G. metallireducens</i> GS-15	Gmet_0571	cdd:274617; pfam09698
0_203(b)	1594	<i>A. sp.</i> K	transmembrane cytochrome <i>c</i> biogenesis protein	5.3E-125	87	471	<i>A. sp.</i> K	AnaeK_0626	EC:1.8.1.8
2_526	1121	<i>A. sp.</i> FW109-5	cytochrome <i>C<sub>551</sub></i> peroxidase	8.8E-48	65	357	<i>Candidatus nitrospira defluvii</i>	<i>ccpA</i>	EC:1.11.1.5; pfam03150
0_117	1943	<i>A. sp.</i> K	ResB required for cytochrome <i>c</i> biosynthesis	4.2E-167	84	392	<i>A. sp.</i> K	-	cdd:263727
2_187	2265	<i>A. sp.</i> K	multiheme cytochrome <i>C<sub>552</sub></i> , nitrite reductase; class III heme-binding domain	0.0	88	557	<i>A. sp.</i> K	AnaeK_2987	EC:1.7.2.2; cdd:277621; pfam02335

Appx. Table 2.3. Pili, flagella, exopolysaccharide and chemotaxis annotations.

BLASTn RefSeq			BLASTx RefSeq & UniProt Hit Information						
Transcript ID	Assembled Length (nt)	Genome	Protein Annotation	<i>E</i>	Sim (%)	Length (aa)	Proteome	Locus/Gene	EC & Database Codes
333_510	410	<i>A. dehalogenans</i> 2CP-C	pilin, type IV, PilA; type II secretion system, protein G region	1.3E-2	48	135	<i>Finegoldia magna</i>	HMPREF0391_11291	pfam08334
			type IV pilin N-terminus methylation site; PulG, pseudopilin, type II secretory pathway region	2.5E-2	47	182	<i>G. lovleyi</i>	Glov_0974	pfam13544; cdd:225076
0_119	509	<i>A. sp.</i> FW109-5	type IV pilin N-terminus methylation site	5.4E-22	69	190	<i>A. sp.</i> K	-	pfam13544
			pilin, type IV, PilA	1.0E-12	66	179	<i>Nitrospira defluvii</i>	-	pfam13544; pfam14245
0_169	580	<i>A. sp.</i> K	type IV pilus assembly, PilZ	1.9E-38	68	127	<i>A. sp.</i> K	AnaeK_3079	pfam07238
0_158	1047	<i>A. dehalogenans</i> 2CP-C	type IV pilus assembly, PilZ	4.0E-31	51	277	<i>A. dehalogenans</i> 2CP-1	A2cp1_4399	pfam07238
0_582	2027	<i>A. sp.</i> K	exopolysaccharide biosynthesis protein; polyprenyl glycosylphosphotransferase	0.0	80	470	<i>A. sp.</i> K	AnaeK_2858	EC:2.7.8.6; TIGR03025; cdd:277520; pfam02397
0_397	1721	<i>A. sp.</i> K	polysaccharide deacetylase	2E-30	50	267	<i>Streptomyces glaucescens</i>	SGLAU_07610	IPR011330; IPR002509; pfam01522
140_0	230	<i>G. sulfurreducens</i> PCA	flagellin, hook-associated FigL	5.0E-14	84	387	<i>Thermotoga sp.</i> 2812B	-	cdd:224263; pfam00669; pfam00700
0_107	1016	<i>A. dehalogenans</i> 2CP-C	chemotaxis, CheY	1.2E-65	100	132	<i>A. dehalogenans</i> 2CP-1	A2cp1_1223	cdd:223816; cdd:238088
0_84	319	<i>A. dehalogenans</i> 2CP-C	chemotaxis, CheY	1.9E-19	67	113	<i>A. dehalogenans</i> 2CP-1	A2cp1_0445	cdd:238088
0_123	734	<i>A. sp.</i> K	chemotaxis, CheY	9.9E-42	81	125	<i>A. sp.</i> K	AnaeK_3907	cdd:238088

Appx. Table 2.4. Carbon degradation annotations.

Transcript ID	Assembled Length (nt)	BLASTn RefSeq	BLASTx RefSeq & UniProt Hit Information						
		Genome	Protein Annotation	<i>E</i>	Sim (%)	Length (aa)	Proteome	Locus/Gene	EC & Database Codes
0_114	2641	<i>A. dehalogenans</i> 2CP-C	aromatic hydrocarbon degradation protein, outer membrane porin	2.8E-109	67	407	<i>A. dehalogenans</i> 2CP-C	-	cdd:277538
10_38	206	<i>A. dehalogenans</i> 2CP-C	extradiol dioxygenase; class III, 4,5-DOPA-dioxygenase	1.0E-7	67	264	<i>A. dehalogenans</i> 2CP-C	-	cdd:153375
0_1594	179	<i>G. daltonii</i> FRC-32	N-ethylammeline chlorohydrolase; ATZ/TRZ hydrolase region	1.87	60	443	<i>Syntrophothermus lipocalidus</i>	-	cdd:238623
0_91	1383	<i>A. sp.</i> FW109-5	2-nitropropane dioxygenase	1.6E-175	85	391	<i>A. dehalogenans</i> 2CP-1	A2cp1_0274	cdd:240081
0_89	1234	<i>A. dehalogenans</i> 2CP-C	L-lactate permease, LldP region	7.4E-147	88	558	<i>A. dehalogenans</i> 2CP-C	Adeh_2974	cdd:224535
0_610	367	<i>A. dehalogenans</i> 2CP-C	chitinase	2.9E-2	76	626	<i>Myxococcus fulvus</i>	-	cdd:263970

Appx. Table 2.5. TCA cycle annotations.

BLASTn RefSeq			BLASTx RefSeq & UniProt Hit Information						
Transcript ID	Assembled Length (nt)	Genome	Protein Annotation	<i>E</i>	Sim (%)	Length (aa)	Proteome	Locus/Gene	EC & Database Codes
0_130	1433	<i>A. sp.</i> FW109-5	succinate dehydrogenase	4.9E-118	94	388	<i>Anaeromyxobacter</i>	sucC	EC:6.2.1.5
0_108(a)	431	<i>A. sp.</i> FW109-5	malate dehydrogenase	1.6E-44	95	312	<i>A. sp.</i> FW109-5	mdh	EC:1.1.1.37
1_318(b)	448	<i>A. dehalogenans</i> 2CP-C	malate dehydrogenase	5.6E-51	95	316	<i>A. dehalogenans</i> 2CP-C	mdh	EC:1.1.1.37
0_118	1312	<i>A. dehalogenans</i> 2CP-C	branched-chain alpha-keto acid dehydrogenase subunit E2, pyruvate dehydrogenase complex	2.2E-28	90	456	<i>Halorhodospira halophila</i>	Hhal_1036	EC:2.3.1.12
0_110	1899	<i>A. sp.</i> FW109-5	isocitrate dehydrogenase	0.0	95	437	<i>A. sp.</i> FW109-5	Anae109_2186	EC:1.1.1.42
0_123	3127	<i>A. sp.</i> K	aconitate hydratase	0.0	87	945	<i>A. dehalogenans</i> 2CP-C	Adeh_3665	EC:4.2.1.3
0_236	1923	<i>A. dehalogenans</i> 2CP-C	fumarate hydratase	4.6E-80	97	540	<i>A. dehalogenans</i> 2CP-C	Adeh_2068	EC:4.2.1.2

## CHAPTER 3

# MICROBIAL FE(III)-REDUCTION IS MODULATED BY OXYGEN PULSE RATES IN REDOX-FLUCTUATING SOIL SLURRIES<sup>1</sup>

---

<sup>1</sup>Wilmoth, J.L., K. Livi and A. Thompson. To be submitted to *Environmental Science and Technology* Journal.

## ABSTRACT

In homogeneous systems, the rate of aqueous Fe(II)-oxidation by O<sub>2</sub> often governs the crystal order of the resulting Fe(III) solids and their reactivity toward microbial Fe(III) reduction. However, it remains unclear if this same behavior occurs during Fe(II)-oxidation in complex, multi-phase systems such as soils. We tested two hypotheses related to this question: (1) Higher rates of Fe(II)-oxidation lead to higher rates of subsequent Fe(III)-reduction during recurring anoxic conditions; and (2) recently precipitated Fe(III) solids are more available for microbial Fe(III) reduction than bulk Fe phases. We tested hypothesis (1) by adding aqueous FeCl<sub>2</sub> to soil slurries from the Bisley Watershed, Luquillo Critical Zone Observatory (LCZO), PR under anoxic conditions and then introduced air at 1 ml h<sup>-1</sup>, 10 ml h<sup>-1</sup>, or 100 ml h<sup>-1</sup> over 24 h and then again exposed to anoxic conditions to measure microbial Fe(III)-reduction rates. We tested hypothesis (2) by tracking the behavior of <sup>57</sup>Fe(II) that had been added to anoxic suspensions during a 7 d anoxic:1 d oxic:7 d anoxic cycle. Mössbauer spectra of control and enriched samples compared at 140 K show that 61 ± 2% of the added <sup>57</sup>Fe atoms partitioned mainly to short-range-ordered Fe(III) during oxidation and 35.8 ± 0.8% was preferentially utilized as a terminal electron acceptor during microbial Fe(III)-reduction. A portion of the <sup>57</sup>Fe(II) generated during microbial Fe(III)-reduction displayed weak magnetic order and quadrupole splitting at low temperature consistent with Fe(II) on the surface and/or internal structure of short-range-order Fe(III)-(oxyhydr)oxides. We also found that 25.9 ± 4.4% of added <sup>57</sup>Fe(III) had become more magnetically ordered at 140 K following microbial Fe(III)-reduction. Electron microscopy and XRD indicated distinct goethite, lepidocrocite and trace hematite phases during the incubation, however Fe-(oxyhydr)oxides under both oxic and anoxic conditions existed as 3 to 8 nm grains.

## INTRODUCTION

Soil Fe(III)-(oxyhydr)oxides influence ecosystem function by regulating the fate of carbon and plant nutrients in the environment (Chacon *et al.*, 2005; Peretyazhko and Sposito, 2005; Hanna, 2007; Scharer *et al.*, 2009; Saïdy *et al.*, 2013). In tropical soils with high biological activity that receive large inputs of organic material from overlying vegetation, the turnover rate of C and plant available nutrients can be extremely rapid (Cusack *et al.*, 2011). Rainfall patterns in humid tropical forest systems modulate soil O<sub>2</sub>-levels over time and diverse microbial populations can thrive under Fe(III)-reducing conditions that occur during redox cycling (DeAngelis *et al.*, 2010; Liptzin *et al.*, 2011). Soil Fe(III)-(oxyhydr)oxides in highly weathered systems serve as abundant terminal electron acceptors for anaerobic microbial growth (Miller *et al.*, 2001; Hutchison and Hesterberg, 2004; Hall *et al.*, 2013). Microbial reduction of Fe(III) in the solid phase leads to the production of Fe(II) as aqueous Fe<sup>2+</sup> ions or complexes or as species adsorbed or structurally incorporated into solid phases (Morgan and Lahav, 2007). Adsorbed Fe(II) under anoxic conditions can catalyze secondary chemical reactions including rapid Fe atom exchange, recrystallization and accelerated Ostwald ripening by mediating the abiotic transfer of electrons to Fe(III)-(oxyhydr)oxides (Williams and Scherer, 2004; Friedrich *et al.*, 2011; Tishchenko *et al.*, 2015). A primary factor controlling microbial Fe(III)-reduction, adsorption and precipitation reactions at the mineral interface is the reactive surface area of Fe(III) solids (Hansel *et al.*, 2004; Roden, 2006; Bonneville *et al.*, 2009). Reactivity is a function of the particle-size and atomic order of Fe(III) minerals, which is controlled by dissolution and Fe(II)-driven recrystallization mechanisms during microbial Fe(III)-reduction, and by oxidation of Fe(II) in solution and in the solid phase (Larese-Casanova *et al.*, 2012; Sjöstedt *et al.*, 2013).

In the circum-neutral pH range of soils and aqueous environments, Fe(II)-oxidation rates proceed very rapidly in the presence of atmospheric O<sub>2</sub> (Singer and Stumm, 1970; Morgan and Lahav, 2007). Rapid oxidation of Fe(II) by O<sub>2</sub> leads to the formation of short-range-order Fe(III) crystals that have low interfacial free energies (Carlson and Schwertmann, 1990; Steefel and Vancappellen, 1990; Schwertmann and Cornell, 1991; Cabot *et al.*, 2007; Gotic *et al.*, 2008). Formation rates of Fe(III) solid phases are dependent on both the homogeneous oxidation of Fe(II) in the aqueous phase and the heterogeneous oxidation rate in the solid phase (Park and Dempsey, 2005; Jones *et al.*, 2014). Consequently, differences in the rate of Fe(II)-oxidation in soils are expected to affect changes in the atomic order and reactivity of the resulting Fe(III) solid phases. Considering that microbial Fe(III)-reduction rates are primarily controlled by reactive surface area and bio-accessibility of Fe(III)-(oxyhydr)oxides, both the atomic order and spatial distribution/location of surface reactive and bulk Fe(III) that develop during Fe(II)-oxidation in soils are expected to alter subsequent microbial Fe(III)-reduction rates.

Spectroscopic analysis of O<sub>2</sub>-induced Fe(II)-oxidation in FRC sediments collected from Oak Ridge, TN showed that little change occurred in Fe phase crystal order over an 81 d oxic cycle (using atm O<sub>2</sub>) following prolonged anoxic conditions (Komlos *et al.*, 2007). Repeated redox cycles in soils from Hawaii using slow pulses of 21% O<sub>2</sub>, that facilitated slower oxidation rates than those that would result from rapid and continuous O<sub>2</sub> exposure, were shown to induce increased atomic order in Fe(III)-(oxyhydr)oxides (Thompson *et al.*, 2006). It has been postulated that the slower pulsed addition of O<sub>2</sub> in the Hawaii soils, that caused slower rates of Fe(II)-oxidation, was the primary mechanism that led to higher crystalline order in Fe(III) solid phases, although that mechanism was not directly tested. We have observed that microbial Fe(III)-reduction rates in laboratory incubations of tropical forest soils collected from the Bisley

Watershed, Luquillo Critical Zone Observatory (LCZO), PR continue to increase over repeated anoxic:oxic cycles following rapid exposure of Fe(II) to a 21% O<sub>2</sub> headspace (Ginn et al., data in prep). A possible explanation for the continued increase in Fe(III)-reduction levels during repeated redox cycling in LCZO soils is that rapid Fe(II)-oxidation during exposure to 21% O<sub>2</sub> leads to decreases in Fe(III) crystalline order, providing Fe(III)-reducing microorganisms with more reactive Fe(III) terminal electron acceptors during recurring anoxic conditions. In the experiments using either the Hawaii or LCZO soils, multiple repeated cycles may have facilitated cumulative effects on Fe(III) crystalline order and reactivity (i.e. facilitating greater abundance of affected Fe(III) pools over time), rendering them more pronounced during analysis. In contrast, changes in bulk Fe crystallinity and reactivity may not be as prominent after a single anoxic:oxic transition as measured by bulk chemical and spectroscopic methods (Komlos *et al.*, 2007). Isotopic tracer experiments using added <sup>57</sup>Fe in the presence of Fe(III)-(oxyhydr)oxides have successfully been used to elucidate discrete surface and bulk atomic-scale interactions that occur via the mineral-solution interface under environmentally relevant conditions (Williams and Scherer, 2004; Fox *et al.*, 2013; Tishchenko *et al.*, 2015). The corresponding chemical and spectroscopic data from this work has been collected under anoxic conditions, focusing on interactions between adsorbed Fe(II) and Fe(III) at Fe(III)-(oxyhydr)oxide surfaces. Accordingly, a similar <sup>57</sup>Fe tracer approach could be used to selectively investigate O<sub>2</sub>-induced Fe(II)-oxidation and microbial Fe(III)-reduction in soils during redox transitions with improved analytical resolution.

For the present study, we hypothesized that (1) higher rates of Fe(II)-oxidation in soil lead to higher rates of subsequent microbial Fe(III)-reduction if the soils become anoxic; and (2) recently precipitated Fe(III) is more available for microbial reduction than bulk soil Fe phases.

We tested the first hypothesis by adding aqueous  $\text{FeCl}_2$  to tropical soils under anoxic conditions, injecting air at rates spanning three orders of magnitude to induce different rates of oxidation, and then re-exposing the slurries to anoxic conditions to measure microbial  $\text{Fe(III)}$ -reduction rates. We tested hypothesis (2) by adding isotopically-labeled  $^{57}\text{Fe(II)}$  to soil suspensions undergoing redox fluctuations and tracking the label through a complete redox cycle (oxidation followed by reduction) via ICP-MS and documenting the solid-phase speciation of the label using  $^{57}\text{Fe}$  Mössbauer spectroscopy. To our knowledge, this work presents the first mechanistic study that examines how  $\text{Fe(II)}$ -oxidation rate by  $\text{O}_2$  impacts subsequent microbial  $\text{Fe(III)}$ -reduction rates and  $\text{Fe(III)}$  availability following an anoxic:oxic transition in soil.

## MATERIALS AND METHODS

### Sample Collection

Soils were collected from the Bisley Watershed, Luquillo Experimental Forest, Puerto Rico. Geographic coordinates, features and site-specific details including annual precipitation have been reported elsewhere (Hall *et al.*, 2013). The Bisley site is part of the NSF-funded Long-Term Ecological Research (LTER) and Critical Zone Observatory (Luquillo CZO) networks. A bulk soil sample (*ca* 1 kg) was excavated from the upper 10 cm of soil of an upland valley position (Peretyazhko and Sposito, 2005). The collected soil was placed in plastic sampling bags and allowed to air-dry before further processing. Air-dried soils were manually crushed and passed through a 2 mm sieve, then homogenized inside of a plastic sample bag before experiments were performed.

## Oxidation Rate Experiment (Testing Hypothesis 1)

### Fe(II) Sorption Isotherm

Prior to the oxidation experiment, we developed an Fe(II)-sorption isotherm for this soil across aqueous Fe(II) concentrations ranging from 0 to 50 mM (as FeCl<sub>2</sub>•4HCl) under anoxic conditions (Coy glovebox, see sections below). Soils were mixed in a 10:1 solution:solid ratio for 2 h on a rotary shaker at 200 rpm with 25 mM MES buffer adjusted to final pH 6.0 and final ionic strength of standard solutions was adjusted with KCl to equal that of the 50 mM aqueous Fe(II) standard. Solid and aqueous phase Fe(II) was measured by a modified ferrozine method (see description below) after centrifugation at 28,000 *rcf* for 15 min., and extraction via 0.5M HCl, respectively. Based on the Fe(II)-sorption data (Appx. Fig. 3.1.) and our previous observations of microbial Fe(III)-reduction in LCZO soils that can generate 100 mmol kg Fe(II) after several weeks under anoxic conditions, we concluded that adding Fe(II) at a concentration of *ca* 100 mmol kg<sup>-1</sup> dry soil would be an effective starting concentration for testing our Fe(II)-oxidation rate hypothesis, as this would provide representative Fe(II) concentrations in both the aqueous and adsorbed solid phases.

### Fe(II) Oxidation Experiment

The Fe(II)-oxidation experiment was conducted by beginning with anoxic soil microcosms containing 2 g air-dry LCZO soil in 120 ml dark amber serum bottles (Wheaton) that had been purged under 3 x vacuum/N<sub>2</sub> and 20 ml anoxic MES buffer added as prepared above, including 10 mM FeCl<sub>2</sub>•4HCl to supply initial Fe(II) at a final concentration of 106 ± 5 mmol kg<sup>-1</sup> dry soil *trt*<sup>-1</sup>. Microcosms were purged by evacuating and filling with N<sub>2</sub> (x2 cycles) and finally with mixed 10% H<sub>2</sub>:90% N<sub>2</sub> (x1 cycle) before transferring to the working compartment of the chamber (Coy Labs; 4% H<sub>2</sub>:96% N<sub>2</sub>). Each microcosm suspension was

closed with a grey butyl stopper and aluminum crimp cap in the glovebox. The soil microcosms were mixed on a rotary shaker (200 rpm) in the glovebox for 24 h to equilibrate the added Fe(II) across the solid and aqueous phases under anoxic conditions prior to air injections. Then duplicate samples were pulsed with air ( $[\text{O}_2]_{\text{atm}}$  ca. 21%  $\text{O}_2$ ) for an initial 7 h period (i.e. at the onset of oxidation) at a rate of either 1, 10 or 100 ml  $\text{hr}^{-1}$  (0.21, 2.1 and 21 ml  $\text{O}_2$   $\text{hr}^{-1}$  respectively) or left permanently anoxic throughout the incubation (in all,  $\text{trt}=4$ ,  $\text{rep}=2$ ).

During  $\text{O}_2$  pulses, microcosms were removed from the anoxic chamber and 10 ml sterile syringes were fitted with 22 ga, sterile stainless steel needles to inject  $\text{O}_2$  into the slow and medium treatment microcosms. The appropriate amount of  $\text{O}_2$  was pulsed by first injecting to create slight overpressure in each sealed microcosm, pumping the syringe (x3), and removing an equal volume to avoid overpressure after mixing. The fast treatment microcosms were exposed to  $\text{O}_2$  every hr by intermittent removal of caps and stoppers with swirling (x3) in the presence of  $\text{O}_2$  (100 ml total exposed and mixed headspace volume), then resealed with new stoppers and caps. All treatments were maintained in  $\text{O}_2$ -exposed suspension on a horizontal shaker for a total of 24 h until reintroduced into the anoxic chamber. Upon reentry into the anoxic chamber, all treatment caps and stoppers were removed and discarded, detectable  $\text{O}_2$  levels allowed to drop to 0 ppm, anoxic gas evacuation/fill to restore anoxic conditions at atm pressure, then new stoppers and caps were fitted to begin a new anoxic period for evaluating the effects of prior Fe(II)-oxidation rate on subsequent microbial Fe(III)-reduction.

The  $\text{O}_2$  addition rates of 0.21, 2.1 and 21 ml  $\text{hr}^{-1}$  will from this point on be referred to as *slow*, *medium*, and *fast* treatments respectively, denoting the relative rate at which Fe(II) was oxidized in each treatment. In total, 0.066, 0.66, and 6.6 mmol  $\text{trt}^{-1}$  of  $\text{O}_2$  (33,  $3.3 \times 10^2$  and  $3.3 \times 10^3$  mmol  $\text{kg}^{-1}$  net  $\text{O}_2$  added to soil) were injected during the initial 7 h of oxidation for the slow,

medium and fast oxidation treatments, respectively. Based on a stoichiometric consumption of  $O_2$  by Fe(II) oxidation to form Fe(III) (4 mol Fe(II) oxidized per mole  $O_2$ ), the net  $O_2$  injected was sufficient to oxidize  $1.32 \times 10^2$ ,  $10^3$  and  $10^4$  mmol  $kg^{-1}$  Fe(II) in the slow, medium and fast treatments, respectively, which was in excess of the total aqueous and solid Fe(II) ( $106 \pm 5$  mmol  $kg^{-1}$   $trt^{-1}$ ) added during equilibration.

#### Isotopically-labeled $^{57}Fe$ Addition Experiment (Testing Hypothesis 2)

We used microcosms as described above, except that  $FeCl_2$  was not added to the original buffer, during a 15 d incubation of LCZO soils that incorporated  $^{57}Fe$ -enrichment. Inside the anoxic chamber, each microcosm suspension was closed with a grey butyl stopper and aluminum crimp cap after measured  $O_2$  levels had decreased below 1 ppm (reading 0 on our meter). Soil microcosms were shaken on a rotary shaker as described above in the anoxic chamber to begin incubation. Prior to establishing the controls and added  $^{57}Fe$ -label treatment, we first pre-incubated the microcosms under anoxic conditions for 7 d.

#### $^{57}Fe$ -label and Control Treatments During Soil Redox Cycling

We established three controls and a primary  $^{57}Fe$ -label treatment in triplicate at the end of the 7 d anoxic pre-incubation period (controls +  $trt = 4$ ,  $rep = 3$ ,  $n = 12$ ): (1) an undisturbed microcosm control; (2) a primary, centrifuged,  $^{57}Fe$ -enriched treatment, (3) an analogous centrifuged,  $FeCl_2 \cdot 4HCl$  amended control and (4) a centrifuged-only control that did not involve removal of the original microcosm supernatant. Control (1) was an important baseline control for all other microcosms. Treatment (2) and control (3) were necessary for quantitative comparison between  $^{57}Fe$ -enriched and non-enriched phases under similar conditions for subsequent  $^{57}Fe$  Mössbauer spectroscopy (MBS) analysis, and control (4) was important to assess any negative impact on microbial Fe(III)-reduction that may have occurred as the result of centrifugation.

Control (1) soil microcosms remained undisturbed in the anoxic glovebox for the duration of the experiment. All remaining soil microcosms were each transferred to individual 50 ml round-bottom centrifuge tubes in the anoxic glove box. The tubes containing total microcosm suspensions were then capped with a fitted rubber o-ring to form a seal under anoxic headspace. The tubes were then transferred outside the glovebox and centrifuged at 28,000 rcf for 15 min. After centrifugation, the tubes were reintroduced into the anoxic glovebox as described above. Treatment (2), the primary  $^{57}\text{Fe}$ -enrichment treatment, was established by first removing the separated aqueous phase that contained  $\text{Fe(II)}_{\text{aq}}$  generated during the initial 7 d anoxic pre-incubation. A prepared solution containing enriched  $^{57}\text{Fe(II)}$  in MES buffer at pH 6.0 was then added to soil pellets to replace the exact volume of original suspension removed from centrifuge tubes. The  $^{57}\text{Fe}$ -enriched MES buffer solution was prepared in advance, prior to the aqueous microcosm transfer. The  $^{57}\text{Fe}$  buffer was prepared by slowly mixing an anoxic stock solution of 100 mM  $^{57}\text{Fe(II)}/0.1\text{ M HCl}$  (>96% isotopic abundance) with 25 mM MES that had previously been adjusted to pH 6.0 with 6 M KOH, and also contained the exact amount of KCl necessary to achieve a final ionic strength equivalent to that of the original microcosm buffer. Before adding the required volume of acidified  $^{57}\text{Fe}$  stock solution to MES buffer, for a final target concentration of 0.7 mM  $^{57}\text{Fe(II)}$ , an equivalent volume of 0.1 M KOH was added first and thoroughly mixed. The target pH of the final  $^{57}\text{Fe}$ -enriched MES buffer was confirmed after preparation, and colorimetric analysis using ferrozine confirmed the target concentration of total Fe(II) (see below for details of ferrozine analysis). Control (3) was established by replacing another set of microcosm supernatant solutions with a solution that had been prepared exactly as the  $^{57}\text{Fe}$  transfer buffer described above, except that the Fe(II)-bearing stock solution contained standard  $\text{FeCl}_2\cdot 4\text{HCl}$  at natural isotopic abundance. When  $^{57}\text{Fe}$ -label and  $\text{FeCl}_2\cdot 4\text{HCl}$  was added

to soils at the end of 7 d by replacing the original buffer solution, care was taken to mitigate drastic changes in total Fe mass balance in the soil by making sure that total Fe in the added buffers closely matched that of the pre-incubation supernatants. The primary reason for this closely matched total Fe concentration during buffer transfer was to prevent adsorption of newly added Fe(II), which could cause changes to the solid phase through dynamic processes such as precipitation, atom-exchange and/or recrystallization. Control (4) was established by using the remaining set of tubes containing pre-incubation supernatants, however, no aqueous transfer was performed. All tubes were finally re-suspended by brief shaking and returned to their corresponding serum bottles as before centrifugation at the end of the 7 d pre-incubation.

#### Induced Redox Transitions Following Microcosm Treatment

After control and treatment microcosms were completely established by the end of the 7 d pre-incubation, all microcosms were shaken and allowed to equilibrate for 2 hrs. Following the 2 hr equilibration, microcosm solutions were removed from the anoxic glove box and exposed to a 21% O<sub>2</sub> atmosphere for 24 hrs while shaking. After 24 hrs of oxidation, we exposed the soils to a 7 d anoxic period and measured changes in Fe(II) concentration and Fe isotopic composition in the aqueous and 0.5M HCl-extractable pools.

#### Incubation Sampling Scheme

Samples were collected for Fe(II) chemical analysis at at the beginning of the experiment (t=0 d) using starting material soil; at the end of the 7 d anoxic pre-incubation period; 2 h after the establishment of the <sup>57</sup>Fe label treatment and control solutions; and then every 24 h during the final anoxic period until the end of the experiment. We collected oxic and anoxic samples for <sup>57</sup>Fe Mössbauer spectroscopy (MBS) and high resolution transmission electron microscopy (HRTEM) analysis immediately following the 24 h oxidation (oxic) and from the end of the

experiment (anoxic). Sterile 10-ml polypropylene syringes fitted with wide bore (16 ga; 1.2 mm id; sterile stainless steel) needles were used to sample 1-ml aliquots of the suspension from the microcosms during sampling. All sampling was performed in the anoxic chamber (during oxic conditions samples were moved temporarily into the anoxic chamber for sampling) and was proceeded by first over-pressurizing the sealed microcosms by injecting 1-ml of anoxic chamber gas. Aliquots were collected in 2-ml micro-centrifuge tubes fitted with rubber o-ring cap seals, which were sealed before being transferred outside of the anoxic chamber for centrifugation at 21,000 rcf for 15 min to separate the aqueous and solid fractions. The centrifuged samples were then returned to the anoxic chamber where the aqueous phase was collected and the pellet was subsequently extracted with 0.5 M HCl. Aqueous phase samples were acidified within the anoxic chamber with trace purity 7 M HCl (7  $\mu$ l/0.5 ml sample) and stored in a clean sealed micro-centrifuge tube in the dark. Trace purity 0.5 M HCl (1 ml) was added to the remaining soil pellet and sealed in the anoxic chamber. The 0.5 M HCl extractions were then vortexed on medium-high speed for 2 hrs in the dark outside the anoxic chamber, after which the extractions were centrifuged as previously described, and the acid supernatant was removed inside the chamber and stored in a clean micro-centrifuge tube in the dark. The HCl-extracted soil pellets were dried on a hotplate at 90°C for 48 hrs and the final mass recorded. The total volume and mass of suspension components removed during each sample-point were recorded, including solution densities of the aqueous buffer and HCl, to calculate the system mass in each microcosm and Fe(II) concentrations.

#### Fe(II) and Fe Isotope Chemical Analysis

A modified ferrozine method was used to quantify Fe(II) in acidified aqueous and HCl extracts (Thompson *et al.*, 2006). The total signal strength of each individual isotope (54, 56, 57

and 58 Fe isotopes) in acidified extracts was measured by inductively-coupled plasma, mass spectrometry, dynamic reaction cell (ICP-MS-DRC, Perkin Elmer) analysis using ppb dilutions of the NIST 1000 ppb Fe standard. Samples analyzed by ICP-MS were measured in an optimized DRC mode using reactive NH<sub>3</sub> gas to minimize potential interferences from Ar, O, and H containing complexes that could convolute the mass-to-charge signal of Fe isotopes. Total elemental Fe concentration in the soil was determined by lithium(Li)-metaborate fusion and digestion (ALS Minerals).

#### <sup>57</sup>Fe-Mössbauer Spectroscopy (MBS)

Samples collected at the end of the oxic and anoxic periods for MBS analysis were centrifuged for 15 min at 21,000 rcf and the supernatants were subsequently removed in the anoxic chamber. Samples for MBS were collected from the <sup>57</sup>Fe-enriched treatment; the FeCl<sub>2</sub>•4HCl amended control; and the centrifuged-only control. Soil pellets remaining in o-ring-lid micro-centrifuge tubes were sealed under an anoxic headspace and stored at -20°C until placed in the Mössbauer spectrometer as follows. Frozen samples were transferred to the anoxic chamber and allowed to thaw. This resulted in a highly viscous gel, which was combined with all similar replicate samples and loaded into the cavity of a 1.25-cm i.d., 1-mm thick nylon ring and sealed between two layers of Kapton tape (180 mg total equivalent dry mass mount<sup>-1</sup>). Prepared sample mounts were immediately placed on ice, transferred to the MBS sample rod and finally placed into a 4.5 K cryostat within the spectrometer for analysis.

<sup>57</sup>Fe Mössbauer absorption spectra of the air-dried soil and sampled incubation soils were collected in transmission mode with a variable temperature He-cooled cryostat (Janis Research Co.) and a 1024 channel detector. A <sup>57</sup>Co source (~50 mCi) embedded in a Rh matrix was held at room temperature. Velocity (i.e. gamma-ray energy) was calibrated using  $\alpha$ -Fe foil at 295 K and

all center shift (CS) and peak positions are reported with respect to this standard. The transducer was operated in constant acceleration mode and spectra were collected across 512 channels and folded against calibration standards to achieve a flat background. Mössbauer spectral fitting was performed using Recoil<sup>TM</sup> software (ISA Inc.) with the Voigt-based fitting (VBF) method of Rancourt and Ping (1991) for quadrupole splitting distributions (QSDs) and combined hyperfine field distributions (HFDs). The area ratios of sextet lines 1 through 6 were held at 3:2:1:1:2:3 and the linewidth (HWHM) was held at 0.097 mm s<sup>-1</sup> corresponding to the minimum theoretical natural linewidth of <sup>57</sup>Fe. All MBS parameter definitions and a description of the relevant notation are given in Rancourt and Ping (1991). A brief description of the MBS fitting methodology is included in the supplementary information section of Tishchenko *et al.* (2015).

#### X-ray diffraction (XRD)

XRD was performed on the air-dry starting material using a Bruker Advance diffractometer with a Co-K $\alpha$  source. Clay-size samples were prepared according to Moore and Reynolds (1997). Clay suspensions were prepared by centrifugation, followed by vacuum filtration and filter-clay-transfer to glass slides, avoiding preferential sedimentation. Scan parameters included a 0.02° increment at 2°/min using a 0.6 mm slit and a 2 $\theta$  interval of 2-70°. Data analysis was performed using the EVA software package (Bruker). All peak assignments were primarily referenced based on parameters reported in Chen (1977).

#### Electron Microscopy

Samples collected for HRTEM were taken from the undisturbed microcosm treatment under oxic and anoxic conditions at 8 d and 15 d respectively. Samples were centrifuged as previously described and the supernatants subsequently removed in the anoxic chamber. Soil pellets remaining in o-ring-lid micro-centrifuge tubes were sealed under anoxic headspace and

stored at  $-20^{\circ}\text{C}$  until further analysis. The frozen soil pellets from both oxic and anoxic time-points were placed on dry ice during transport to the High-Resolution Analytical Electron Microbeam (HRAEM) Facility at Johns Hopkins University. Samples were prepared following the general procedures of Wang *et al.* (2008). Briefly, one selected replicate from each time-point was suspended and diluted in absolute ethanol, dispersed by ultrasonication, deposited onto carbon-coated grids, then transferred to the vacuum chamber of the electron microscope. HRTEM, energy dispersive X-ray spectroscopy (EDXS), selective area electron diffraction (SAED) and electron energy loss spectroscopy (EELS) analyses were performed using an FEI CM 300 FEG electron microscope equipped with Gatan EELS 200 and Oxford EDXS detectors. Electron energies were tuned within the range of 100 to 300 keV depending on specific optimization for each type of measurement.

## RESULTS

### Experiment #1: Influence of Fe(II)-Oxidation Rate on Fe(III)-Reduction Rates

At the end of the Fe(II)-oxidation event in the first experiment, Fe(II) concentrations were below detection in the aqueous phase and lowered to  $23.4 \pm 6 \text{ mmol kg}^{-1}$  in the 0.5M HCl extractable phase, indicating that *ca* 80% of the supplied Fe(II)  $\text{trt}^{-1}$  from  $\text{FeCl}_2 \cdot 4\text{H}_2\text{O}$  at the beginning of the experiment was completely oxidized after 24 h following introduction of  $\text{O}_2$  (Fig. 3.1.). Over the subsequent 14 d anoxic period, Fe(II) concentrations increased across all treatments, with the highest peak values observed in the fast oxidation treatment with  $39 \pm 6.4$  and  $191.5 \pm 40.1 \text{ mmol Fe(II) kg}^{-1}$  in the aqueous and 0.5M HCl extractable pools respectively. The highest total microbial Fe(III)-reduction rate occurred in the fast oxidation treatment at 0.62

$\pm 0.14 \text{ mmol Fe(II) kg}^{-1} \text{ hr}^{-1}$  and was found to be significantly higher than that of the slow treatment ( $0.29 \pm 0.05$ ;  $p = 0.0383$ ) and the anoxic control ( $0.25 \pm 0.005$ ;  $p = 0.0267$ ) (Fig. 3.2.).

### Experiment #2: Characterization of Recently Precipitated $^{57}\text{Fe}$

Overall, Fe(II) concentrations measured in the  $^{57}\text{Fe}$ -label treatment and controls only differed marginally in both the aqueous and solid phases over the last two days of incubation (Fig. 3.3.). However, the Fe(II) concentrations for the  $^{57}\text{Fe}$ -label treatment and analogous  $\text{FeCl}_2 \cdot 4\text{HCl}$  control overlapped and were slightly lower in concentration, whereas the other two treatments overlapped and were at slightly higher concentrations overall. This decrease in Fe reduction rate for the treatments with added Fe may have resulted from several factors. Since we removed the original buffer solution before adding the Fe, any constituents that dissolved during the pre-treatment would not be present in the Fe-addition treatments. Importantly however, the  $^{57}\text{Fe}$ -enrichment treatment and analogous  $\text{FeCl}_2 \cdot 4\text{HCl}$  treatment overlapped in aqueous and HCl Fe(II) concentrations at every time-point within error.

### Iron Isotope Dynamics Following the $^{57}\text{Fe}$ -Label Addition

After the establishment of treatments at the end of 7 d pre-treatment period, and immediately following 24 hrs oxidation of Fe(II) under 21%  $\text{O}_2$  by 8 d, Fe(II) fell below detection in the aqueous phase (Fig. 3.4.). An increase in both aqueous and solid phase Fe(II), following oxidation, was not observed until 13 d. The total aqueous and HCl Fe(II) at 13 d showed an initial increase of  $40 \text{ mmol Fe(II)}_{\text{T}} \text{ kg}^{-1}$  marking the onset of Fe(III)-reduction (Fig. 3.3.). The aqueous  $^{57/54}\text{Fe}$  ratio at 13 d showed a corresponding increase to  $2.94 \pm 0.75$  that was higher than the HCl-extractable  $^{57/54}\text{Fe}$  ratio of  $1.59 \pm 0.19$  at 13 d (Fig. 3.4.), demonstrating that a small concentration of  $^{57}\text{Fe}$ -label atoms ( $0.18 \pm 0.15 \text{ mmol } ^{57}\text{Fe} \text{ kg}^{-1}$ ) (Fig. 3.5.)) in the solid

phase were more available than all other  $^{57}\text{Fe}$ -label atoms at the onset of Fe(III)-reduction and Fe(II) solubilisation.

Comparison of Fe(II) concentrations immediately before and after the  $^{57}\text{Fe}$ -label addition show that no net mass transfer of Fe(II) occurred as a result of our Fe-addition (Fig 3.3.). However, the  $^{57}\text{Fe}$ (II) enrichment did display isotopic exchange. The initial  $^{57}\text{Fe}$ -label buffer solution contained *ca* 0.97  $^{57}\text{Fe}$ /total Fe ( $\text{Fe}_T$ ) isotopic ratio, but this decreased to *ca* 0.22  $^{57}\text{Fe}/\text{Fe}_T$  after 2 hrs of mixing (Fig. 3.5.). Therefore, a large proportion of added  $^{57}\text{Fe}$  underwent exchange with native Fe prior to the oxidation event. This decrease in aqueous  $^{57}\text{Fe}/\text{Fe}_T$  isotopic ratio corresponds to  $^{57}\text{Fe}$ -label ( $6.5 \pm 0.1 \text{ mmol kg}^{-1}$ ) that adsorbed to the solid phase during 2 hr mixing. Only  $^{57}\text{Fe}$ -label at  $0.8 \pm 0.05 \text{ mmol kg}^{-1}$  remained in the aqueous phase just prior to oxidation. We estimate that the minimum rate (i.e. net rate) of  $^{57}\text{Fe}$ (II)-label exchange between the aqueous and solid phases, calculated by dividing the  $^{57}\text{Fe}$ -label concentration that moved into the solid phase by the mixing time, was  $6.5 \text{ mmol kg}^{-1} 2 \text{ hrs}^{-1}$  (or  $3.25 \text{ mmol kg}^{-1} \text{ hr}^{-1}$ ).

We were able to account for all added  $^{57}\text{Fe}$  ( $7.26 \pm 0.1 \text{ mmol kg}^{-1}$  dry soil) just prior to oxidation, after summing the concentrations between the aqueous and 0.5 M HCl-extractable solid phases at the end of the pre-treatment period, 0.8 and  $6.5 \text{ mmol kg}^{-1}$  dry soil respectively, equivalent to  $^{57}\text{Fe}$ -label added at  $7.3 \text{ mmol kg}^{-1}$  on average during enrichment (Fig. 3.5.). For 48 hrs after oxidation, the HCl-extractable  $^{57}\text{Fe}$ -label decreased from 6 to  $5 \text{ mmol kg}^{-1}$ , but remained relatively constant at  $5 \text{ mmol kg}^{-1}$  for the remainder of the experiment. This was despite a large decrease in the  $\text{Fe}_T$  extracted by HCl, which at first decreased from 120 to  $45 \text{ mmol kg}^{-1}$  in the first 48h following oxidation, and then increased to  $120 \text{ mmol kg}^{-1}$  by the end of the experiment. This increase was positively correlated with Fe(II) production (Fig. 3.3.) and is consistent with microbial Fe(III)-reduction. Evidently, oxidation renders total Fe less susceptible to 0.5 M HCl

dissolution than when the soil is anoxic. This dissolution behaviour of HCl-extractable  $\text{Fe}_T$  influences the calculation of  $^{57}\text{Fe}\%$  measured relative to all isotopes. This effect can clearly be seen when comparing the  $^{57}\text{Fe}\%$  and HCl  $\text{Fe}_T$  graphs for the solid phase (HCl column, Fig. 3.5.). By including the added  $^{57}\text{Fe}$ -label graph to the comparison, we see that added  $^{57}\text{Fe}$  does not change between 10 d and 15 d, confirming that large changes in HCl-extractable  $\text{Fe}_T$  over the same period influence calculation of mixed native and enriched isotope proportions. This also may explain the slight decrease in  $^{57/54}\text{Fe}$  ratios for the solid phase during microbial Fe(III)-reduction toward the end of the experiment (Fig. 3.4.).

### $^{57}\text{Fe}$ -Mössbauer Spectroscopy (MBS)

We compared the 140 and 4.5 K Mössbauer spectra of the  $^{57}\text{Fe}$ -label treatment and  $\text{FeCl}_2$  control samples to quantify which Fe phases became enriched during oxic and anoxic conditions. We assumed that any differences between treatment and control spectra represent accumulation of the added  $^{57}\text{Fe}$ -label compared to natural abundance  $^{57}\text{Fe}$  in those portions of the spectra, after taking into account the different total concentrations of  $^{57}\text{Fe}$  in the treatment and the control samples. We performed these comparisons for examining added  $^{57}\text{Fe}$  between spectra collected at 140 and 4.5 K, because data collected at cryo-temperatures should theoretically show the highest recoilless fraction of all  $^{57}\text{Fe}$  atoms in the samples. Our 140 K data show that following oxidation,  $61 \pm 2\%$  added  $^{57}\text{Fe}$ -label was enriched in paramagnetic Fe(III) (Fig 3.6. and Fig. 3.7.; Appx. Table 3.1.). At 4.5 K,  $55.2 \pm 2.0\%$  of the oxidized  $^{57}\text{Fe}$ -label displayed a sextet, while  $17.3 \pm 0.9\%$  remained as paramagnetic Fe(III). Taken together, these results are consistent with our chemical analyses that show much of the  $^{57}\text{Fe}$ -label remained in more disordered solid phases after oxidation. Paramagnetic Fe(III) that magnetically orders into a sextet upon cooling from 140 K to 4.5 K represents more disordered forms of Fe(III) minerals. In general, we interpret the

Fe(III) doublet at 140 K as representing the proportion of  $^{57}\text{Fe}$  associated with more short-range-order phases (Fig. 3.8. and Fig. 3.9.; Appx. Table 3.1.). We found that after 7 d of microbial Fe(III)-reduction, the Fe(III) doublet at 140K decreased with a corresponding increase in a Fe(II)-doublet ( $35.8 \pm 0.8\%$   $^{57}\text{Fe}$ -label Fe(III) reduced to Fe(II)). This shows overall that the  $^{57}\text{Fe}$ -label was incorporated in highly disordered Fe(III) phases following oxidation that were reduced by microorganisms during subsequent Fe(III)-reduction. We observed that  $25.9 \pm 4.4\%$  added  $^{57}\text{Fe}$  had become more crystalline following Fe(III)-reducing conditions, as the area of the  $^{57}\text{Fe}$ -label sextet at 140 K increased over the course of the anoxic period. We also found that  $^{57}\text{Fe}$ -label Fe(II) ( $11.6 \pm 2.7\%$   $^{57}\text{Fe}$ -label) at 4.5 K was magnetically ordered, indicating that much of the reduced  $^{57}\text{Fe}$ -label had formed at the surface of more magnetically-ordered Fe(III)-(oxyhydr)oxides and/or was incorporated in a disordered magnetic phase such as nano-magnetite, however, the actual species could not be confirmed. Despite detecting low intensity primary peaks of goethite and lepidocrocite in our XRD pattern of the soil clay-fraction (Appx. Fig. 3.2.), we could not distinguish these individual phases in the MBS spectra.

### Electron Microscopy

We found no distinguishing differences in electron microscopy analyses between samples collected at the end of the oxidation event and the end of subsequent the anoxic period. HRTEM images from both samples revealed clusters of 3-8 nm Fe-(oxyhydr)oxide crystals aggregated together with similar morphology (Appx. Fig. 3.3. and Appx. Fig. 3.4.). Subsequent analyses carried out on the oxidized sample by energy dispersive spectroscopy (EDXS) revealed relatively small contributions of Al and Si in the bulk structure (Appx. Fig. 3.5.). Selective area electron diffraction (SAED) patterns collected near the edges of the cluster suggested possible contributions of hematite, although hematite was not detected or assigned in our XRD and MBS

analyses (Fig. 3.10.). Electron energy loss spectroscopy (EELS) of these nano-Fe clusters in both oxic and anoxic samples did not show any conclusive differences between Fe(II)/Fe(III) ratios collected under different experimental conditions (Appx. Fig. 3.6.). We expected that Fe(II)/Fe(III) ratios would be higher in the anoxic samples, consistent with our MBS and chemical data. However, if Fe(II) atoms were located in thin layers (e.g. as in mono-layers) on bulk mineral surfaces or were otherwise dilute relative to neighboring Fe(III) atoms, the EELS analysis may have lacked the sensitivity to detect the associated Fe(II) (Wang *et al.*, 2008).

## DISCUSSION

Rapid oxidation of Fe(II) by O<sub>2</sub> leads to the formation of short-range-order Fe(III) crystals that have low interfacial free energies (Carlson and Schwertmann, 1990; Steefel and Vancappellen, 1990; Schwertmann and Cornell, 1991; Cabot *et al.*, 2007; Gotic *et al.*, 2008). Consequently, differences in the rate of Fe(II)-oxidation in soils are expected to affect changes in the crystallinity and reactivity of the resulting Fe(III) solid phases. Although spectroscopic and chemical studies of O<sub>2</sub>-induced Fe(II)-oxidation in soils and sediments have been performed (Thompson *et al.*, 2006; Komlos *et al.*, 2007), and the effects of Fe(III)-mineral speciation, reactivity and system heterogeneity on Fe(III)-reduction examined (Zachara *et al.*, 1998; Roden, 2006; Pallud *et al.*, 2010), to our knowledge there have been no direct tests to validate that Fe(II)-oxidation rate by O<sub>2</sub> is a primary mechanism for subsequent changes in microbial Fe(III)-reduction rates and enhanced availability of recently precipitated Fe(III) to microbial cells under recurring anoxic conditions in soil.

### Role of Oxidation Rate in Fe(III) Reactivity

In our present study, we found that higher Fe(II)-oxidation rates by O<sub>2</sub> led to higher rates of microbial Fe(III)-reduction during subsequent anoxic conditions in soils (Fig. 3.1. and 3.2.). This result is consistent with the formation of Fe(III)-minerals of lower crystallinity in the fast Fe(II)-oxidation rate treatment. One reason we suspect that the anoxic control did not display higher Fe(III)-reduction rates over time is that added Fe(II) likely blocked Fe(III)-surface sites in the soil, effectively insulating the native Fe(III)-(oxyhydr)oxides from accepting electrons. Chemical and solid phase data using <sup>57</sup>Fe enrichment and controls indicated several relevant and dynamic reaction pathways during Fe-redox cycling that contribute to transformations in Fe(III)-(oxyhydr)oxides and corresponding changes in reactivity toward microbial Fe(III)-reduction.

After mixing and rapid oxidation of suspensions containing added <sup>57</sup>Fe, we found that the majority of enriched isotope was present in non-magnetically ordered Fe(III) at 140 K (Fig 3.6. and 3.8.). A smaller portion of the added <sup>57</sup>Fe-label formed a solid phase that magnetically ordered at 140 K with a peak hyperfine field strength ( $B_{hf}$ ) of 49.5 T and a quadrupole splitting value of  $-0.107 \text{ mm s}^{-1}$ , suggestive of micro-crystalline goethite (Kukkadapu *et al.*, 2001; Thompson *et al.*, 2006; Wu *et al.*, 2012). This phase increased in abundance following subsequent microbial Fe(III)-reduction, which might represent a general ripening of the <sup>57</sup>Fe label to more crystalline phases after exposure to aqueous and adsorbed Fe(II) during the anoxic period. The higher crystallinity of a portion of the precipitated <sup>57</sup>Fe-label likely explains why we could not extract all  $7.3 \text{ mmol kg}^{-1}$  of the added <sup>57</sup>Fe-label in 0.5 M HCl after 7 d. As previously mentioned, 0.5 M HCl most efficiently dissolves short-range-ordered (SRO) Fe minerals, leaving most crystalline phases intact (Peretyazhko and Sposito, 2005).

### Preferential Microbial Reduction of Recently Precipitated Fe(III)

Not only did the  $^{57}\text{Fe}$ -label preferentially precipitate as short-range-ordered Fe(III)-solids following oxidation, but this recently precipitated  $^{57}\text{Fe}$ (III)-label was preferentially reduced at the onset of subsequent microbial Fe(III)-reduction relative to the native soil Fe(III) phases (Fig. 3.4.). Some of these reduced added  $^{57}\text{Fe}$ (III) atoms entered solution at the onset of microbial Fe(III)-reduction (Fig. 3.4.), although most of the  $^{57}\text{Fe}$ (II) that formed during microbial Fe(III)-reduction remained in the solid phase, where MBS results confirm reduction of the solid-phase  $^{57}\text{Fe}$ (III)-label and chemical extractions show the corresponding movement of  $^{57}\text{Fe}$ -label from the solid to aqueous phase during microbial Fe(III)-reduction (deduced as soluble  $^{57}\text{Fe}$ (II) generated during reduction). Taken together, these results show that Fe(II) atoms that move from aqueous solution to the solid phase during atom exchange and oxidation by 21%  $\text{O}_2$ , as solid Fe(III), are highly reactive toward and preferentially re-reduced at the onset of subsequent microbial Fe(III)-reduction in the soil. These results provide evidence that adsorption and rapid oxidation of Fe(II) in redox-dynamic soils leads to the formation of more reactive Fe(III) electron acceptors, and provide a mechanistic explanation of our initial observations that microbial Fe(III)-reduction rates are intimately linked to prior Fe(II)-oxidation rates in humid tropical forest soils.

We found that aqueous  $^{57}\text{Fe}/\text{Fe}_T$  isotope ratios are mainly dependent on changes in the solid phase, which regulate mass transfer of Fe(II) from/to solution during oxidizing and reducing conditions (Fig. 3.5.). Overall, considering that acid-extractable added  $^{57}\text{Fe}$  levels remained relatively unchanged in the solid phase, despite large changes in the efficiency of extracting Fe with HCl, we can confirm that the majority of our added  $^{57}\text{Fe}$  remained reactive toward HCl extraction during the incubation, regardless of total HCl Fe extraction. Given that 5

mmol kg<sup>-1</sup> added <sup>57</sup>Fe-label remained constant in concentration between 10 d and 15 d despite large changes in HCl-extractable Fe<sub>T</sub>, 68% of the added <sup>57</sup>Fe-label was clearly more reactive toward acid dissolution (i.e. part of more reactive Fe pool(s)) than the bulk native Fe phases over the same period. This net result demonstrates that nearly all of the enriched added <sup>57</sup>Fe was associated with the more HCl-reactive Fe populations in the soil during the experiment.

#### Identification of Fe Minerals During Incubation

The mineral ferrihydrite is a naturally occurring nano-Fe(III)-oxyhydroxide that typically exists in the same particle-size range as the clustered Fe-(oxyhydr)oxide crystals observed in our oxic and anoxic samples using HRTEM (i.e. 3-8 nm) (Cismasu *et al.*, 2012). Disordered and irregular ferrihydrite-cluster edges have also been observed in synthetic media (Cismasu *et al.*, 2012), and we note similar characteristics in the predominant Fe-(oxyhydr)oxide crystals in our samples (Fig. 3.10.). The presence of ferrihydrite-clusters in our samples could also explain the detection of hematite in our SAED patterns, as ferrihydrite can serve as a precursor to hematite under environmentally relevant conditions (Michel *et al.*, 2010).

#### CONCLUSIONS

We have demonstrated that faster rates of Fe(II) oxidation lead to faster rates of microbial Fe(III) reduction during subsequent anoxic conditions in soil. Chemical and solid phase data using <sup>57</sup>Fe enrichment and controls indicated several important mechanisms during Fe-redox cycling that contributed to transformations in Fe(III)-(oxyhydr)oxides and corresponding changes in reactivity toward microbial Fe(III)-reduction. Mössbauer spectra compared between 140 and 4.5 K show that added <sup>57</sup>Fe partitioned mainly to highly disordered Fe(III) during rapid oxidation of <sup>57</sup>Fe(II) in both aqueous and solid phases. Samples analyzed at the end of

subsequent anoxic conditions show that added  $^{57}\text{Fe(III)}$ , formed during Fe(II)-oxidation and incorporated in more amorphous Fe(III) phases, was preferentially utilized as a terminal electron acceptor during microbial Fe(III)-reduction. A portion of the Fe(II) generated during microbial Fe(III)-reduction displayed weak magnetic order and quadrupole splitting at 4.5 K consistent with Fe(II) on the surface and/or internal structure of short-range-order Fe(III)-(oxyhydr)oxides. The presence of magnetically ordered Fe(II) was concomitant with incomplete dissolution of solid phase Fe(II) by 0.5 M HCl extraction. This Fe(II) phase indicates an anaerobic biotransformation product of Fe-(oxyhydr)oxides that could not be assigned to adsorbed Fe(II) or magnetite. We also found that a small portion of added  $^{57}\text{Fe(III)}$  became more magnetically ordered (i.e. more crystalline) during microbial Fe(III)-reduction, perhaps as the result of accelerated Ostwald ripening in the presence of microbial-generated Fe(II) during anoxic conditions. Our results provide spectroscopic evidence that rapid oxidation of Fe(II) in complex soil systems also displays similar behavior, in terms of Fe-mineral transformation and reactivity, to well-studied synthetic systems under controlled laboratory conditions. Based on our findings, future work will need to examine the occurrence and magnitude of these processes as governed by Fe(II)-oxidation rates in the field during redox-cycling over time, with detailed attention to their impact on microbial Fe(III)-reduction rates, nutrient availability and the C cycle.

#### ACKNOWLEDGEMENTS

We thank Kenneth Livi for analysis in the High-Resolution Analytical Electron Microbeam Facility at Johns Hopkins University. We thank Michelle Scherer and Timothy Pasakarnis at the University of Iowa for providing  $^{57}\text{Fe}$ -isotope. We thank Nehru Mantripragada for ICP-MS analysis at the University of Georgia. Important funding was provided through the

USDA-AFRI Soil Processes Program, NSF Geobiology and Low-Temperature Geochemistry, and NSF Critical Zone Observatory Programs.

#### LITERATURE CITED

- Bonneville S, Behrends T, Van Cappellen P. (2009). Solubility and dissimilatory reduction kinetics of iron(III) oxyhydroxides: A linear free energy relationship. *Geochim Cosmochim Acta* **73**: 5273-5282.
- Cabot A, Puentes VF, Shevchenko E, Yin Y, Balcells L, Marcus MA *et al.* (2007). Vacancy coalescence during oxidation of iron nanoparticles. *J Am Chem Soc* **129**: 10358-+.
- Carlson L, Schwertmann U. (1990). The effect of CO<sub>2</sub> and oxidation rate on the formation of goethite versus lepidocrocite from an Fe(II) system at pH-6 and pH-7. *Clay Miner* **25**: 65-71.
- Chacon N, Dezzeo N, Munoz B, Rodriguez JM. (2005). Implications of soil organic carbon and the biogeochemistry of iron and aluminum on soil phosphorus distribution in flooded forests of the lower Orinoco river, Venezuela. *Biogeochemistry* **73**: 555-566.
- Chen PY 1977. Table of key lines in x-ray powder diffraction patterns of minerals in clays and associated rocks. *In*: RESOURCES, D. O. N. (ed.) Occasional Paper 21 ed. Bloomington, Indiana: Authority of the State of Indiana.
- Cismasu AC, Michel FM, Stebbins JF, Levard C, Brown GE. (2012). Properties of impurity-bearing ferrihydrite I. Effects of Al content and precipitation rate on the structure of 2-line ferrihydrite. *Geochim Cosmochim Acta* **92**: 275-291.

- Cusack DF, Silver WL, Torn MS, Burton SD, Firestone MK. (2011). Changes in microbial community characteristics and soil organic matter with nitrogen additions in two tropical forests. *Ecology* **92**: 621-632.
- Deangelis KM, Silver WL, Thompson AW, Firestone MK. (2010). Microbial communities acclimate to recurring changes in soil redox potential status. *Environ Microbiol* **12**: 3137-3149.
- Fox PM, Davis JA, Kukkadapu R, Singer DM, Bargar J, Williams KH. (2013). Abiotic u(vi) reduction by sorbed fe(ii) on natural sediments. *Geochimica Et Cosmochimica Acta* **117**: 266-282.
- Friedrich AJ, Luo Y, Catalano JG. (2011). Trace element cycling through iron oxide minerals during redox-driven dynamic recrystallization. *Geology* **39**: 1083-1086.
- Gotic M, Music S, Popovic S, Sekovanic L. (2008). Investigation of factors influencing the precipitation of iron oxides from fe(ii) containing solutions. *Croat Chem Acta* **81**: 569-578.
- Hall SJ, McDowell WH, Silver WL. (2013). When wet gets wetter: Decoupling of moisture, redox biogeochemistry, and greenhouse gas fluxes in a humid tropical forest soil. *Ecosystems* **16**: 576-589.
- Hanna K. (2007). Adsorption of aromatic carboxylate compounds on the surface of synthesized iron oxide-coated sands. *Appl Geochem* **22**: 2045-2053.
- Hansel CM, Benner SG, Nico P, Fendorf S. (2004). Structural constraints of ferric (hydr)oxides on dissimilatory iron reduction and the fate of fe(ii). *Geochim Cosmochim Ac* **68**: 3217-3229.

- Hutchison KJ, Hesterberg D. (2004). Dissolution of phosphate in a phosphorus-enriched ultisol as affected by microbial reduction. *J. Environ. Qual.* **33**: 1793-1802.
- Jones AM, Griffin PJ, Collins RN, Waite TD. (2014). Ferrous iron oxidation under acidic conditions – the effect of ferric oxide surfaces. *Geochim Cosmochim Acta* **145**: 1-12.
- Komlos J, Kukkadapu RK, Zachara JM, Jaffe PR. (2007). Biostimulation of iron reduction and subsequent oxidation of sediment containing Fe-silicates and Fe-oxides: Effect of redox cycling on Fe(III) bioreduction. *Water Res* **41**: 2996-3004.
- Kukkadapu RK, Zachara JM, Smith SC, Fredrickson JK, Liu CX. (2001). Dissimilatory bacterial reduction of Al-substituted goethite in subsurface sediments. *Geochimica Et Cosmochimica Acta* **65**: 2913-2924.
- Larese-Casanova P, Kappler A, Haderlein SB. (2012). Heterogeneous oxidation of Fe(II) on iron oxides in aqueous systems: Identification and controls of Fe(III) product formation. *Geochim Cosmochim Acta* **91**: 171-186.
- Liptzin D, Silver WL, Detto M. (2011). Temporal dynamics in soil oxygen and greenhouse gases in two humid tropical forests. *Ecosystems* **14**: 171-182.
- Michel FM, Barron V, Torrent J, Morales MP, Serna CJ, Boily J-F *et al.* (2010). Ordered ferrimagnetic form of ferrihydrite reveals links among structure, composition, and magnetism. *P Natl Acad Sci USA* **107**: 2787-2792.
- Miller AJ, Schuur EaG, Chadwick OA. (2001). Redox control of phosphorus pools in hawaiian montane forest soils. *Geoderma* **102**: 219-237.
- Moore DMaR, R.C. 1997. *X-ray diffraction and the identification and analysis of clay minerals*, Oxford University Press.

- Morgan B, Lahav O. (2007). The effect of pH on the kinetics of spontaneous Fe(II) oxidation by  $O_2$  in aqueous solution - basic principles and a simple heuristic description. *Chemosphere* **68**: 2080-2084.
- Pallud C, Kausch M, Fendorf S, Meile C. (2010). Spatial patterns and modeling of reductive ferrihydrite transformation observed in artificial soil aggregates. *Environ Sci Technol* **44**: 74-79.
- Park B, Dempsey BA. (2005). Heterogeneous oxidation of Fe(II) on ferric oxide at neutral pH and a low partial pressure of  $O_2$ . *Environ Sci Technol* **39**: 6494-6500.
- Peretyazhko T, Sposito G. (2005). Iron(III) reduction and phosphorous solubilization in humid tropical forest soils. *Geochim Cosmochim Acta* **69**: 3643-3652.
- Rancourt DG, Ping JY. (1991). Voigt-based methods for arbitrary-shape static hyperfine parameter distributions in Mossbauer spectroscopy. *Nucl. Instrum. Methods Phys. Res. Sect. B-Beam Interact. Mater. Atoms* **58**: 85-97.
- Roden EE. (2006). Geochemical and microbiological controls on dissimilatory iron reduction. *Crit Rev Geosci* **338**: 456-467.
- Saidy AR, Smernik RJ, Baldock JA, Kaiser K, Sanderman J. (2013). The sorption of organic carbon onto differing clay minerals in the presence and absence of hydrous iron oxide. *Geoderma* **209**: 15-21.
- Scharer M, De Grave E, Semalulu O, Sinaj S, Vandenberghe RE, Frossard E. (2009). Effect of redox conditions on phosphate exchangeability and iron forms in a soil amended with ferrous iron. *Eur J Soil Sci* **60**: 386-397.
- Schwertmann U, Cornell RM 1991. *Iron oxides in the laboratory preparation and characterization*.

- Singer PC, Stumm W. (1970). Acid mine drainage: The rate-determining step. *Science* **167**: 1121-1123.
- Sjöstedt C, Persson I, Hesterberg D, Kleja DB, Borg H, Gustafsson JP. (2013). Iron speciation in soft-water lakes and soils as determined by exafs spectroscopy and geochemical modelling. *Geochimica et Cosmochimica Acta* **105**: 172-186.
- Steeffel CI, Vancappellen P. (1990). A new kinetic approach to modeling water-rock interaction - the role of nucleation, precursors, and ostwald ripening. *Geochim Cosmochim Ac* **54**: 2657-2677.
- Thompson A, Chadwick OA, Rancourt DG, Chorover J. (2006). Iron-oxide crystallinity increases during soil redox oscillations. *Geochim Cosmochim Ac* **70**: 1710-1727.
- Tishchenko V, Meile C, Scherer MM, Pasakarnis TS, Thompson A. (2015). Fe<sup>2+</sup> catalyzed iron atom exchange and re-crystallization in a tropical soil. *Geochim Cosmochim Ac* **148**: 191-202.
- Wang YH, Morin G, Ona-Nguema G, Menguy N, Juillot F, Aubry E *et al.* (2008). Arsenite sorption at the magnetite-water interface during aqueous precipitation of magnetite: Exafs evidence for a new arsenite surface complex. *Geochim Cosmochim Ac* **72**: 2573-2586.
- Williams AGB, Scherer MM. (2004). Spectroscopic evidence for fe(ii)-fe(iii) electron transfer at the iron oxide-water interface. *Environ Sci Technol* **38**: 4782-4790.
- Wu T, Shelobolina E, Xu H, Konishi H, Kukkadapu R, Roden EE. (2012). Isolation and microbial reduction of fe(iii) phyllosilicates from subsurface sediments. *Environmental Science & Technology* **46**: 11618-11626.

Zachara JM, Fredrickson JK, Li SM, Kennedy DW, Smith SC, Gassman PL. (1998). Bacterial reduction of crystalline  $Fe^{3+}$  oxides in single phase suspensions and subsurface materials.

*Am Mineral* **83**: 1426-1443.

TABLES AND FIGURES

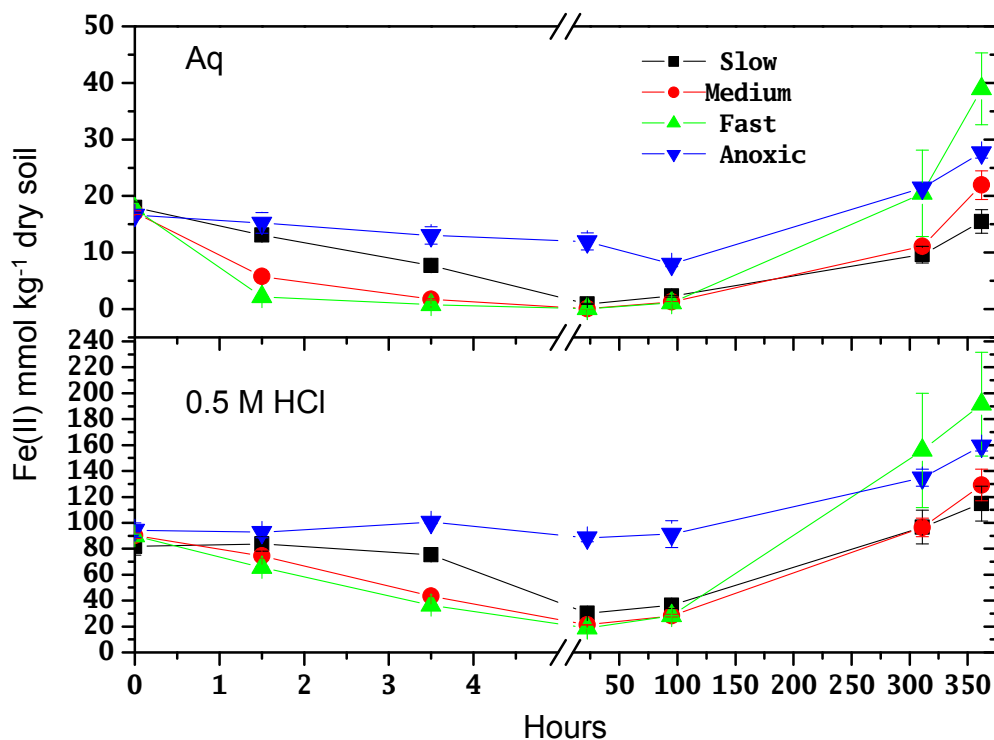


Figure 3.1. Fast, Medium and Slow oxidation rates of supplied Fe(II), supplied as FeCl<sub>2</sub>, (experiment #1) lead to different rates of microbial Fe(III)-reduction in LCZO soils following oxic conditions. Beginning at 0 hrs, serum bottles were pulsed with air ( $[O_2]_{atm}$  ca 21% O<sub>2</sub>) for an initial 7 h period (i.e. at the onset of oxidation) at a rate of either 1, 10 or 100 ml hr<sup>-1</sup> (0.21, 2.1 and 21 ml O<sub>2</sub> hr<sup>-1</sup> respectively) or left permanently anoxic throughout the incubation (in all, trt=4, rep=2). Error bars represent aqueous (top) and 0.5 M HCl (bottom) extractable Fe(II) averages  $\pm$ stdev (n=2).

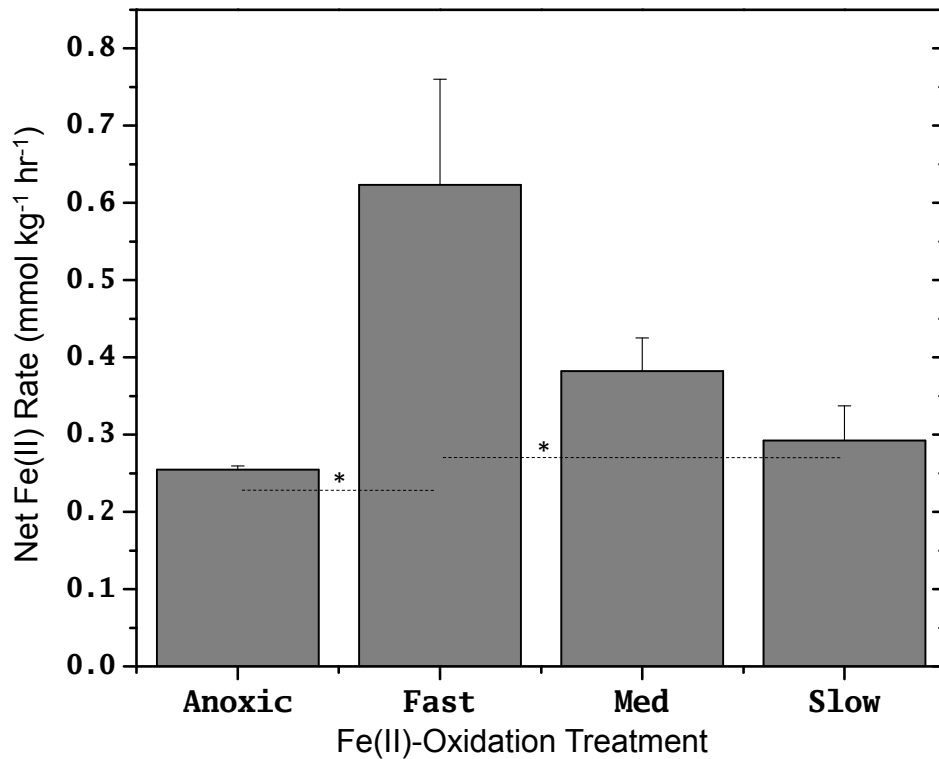


Figure 3.2. Net rate of Fe(II)-production (aqueous + 0.5 M HCl extractable Fe(II)) between 24 and 360 hrs (between sample point 4 and 7), following 24 hrs oxidation in Fast, Medium (Med) and Slow treatments, including the Anoxic control. ANOVA was used to calculate Net Fe(II) means  $\pm$ stdev (n=2). Significance was detected between Fast oxidation and Anoxic control ( $p = 0.0267$ ) and between Fast and Slow Oxidation treatments ( $p = 0.0383$ ).  $P$ -values from Tukey's Test are indicated by  $p < 0.05^*$ , where dashed lines connect significantly different treatment and control means.

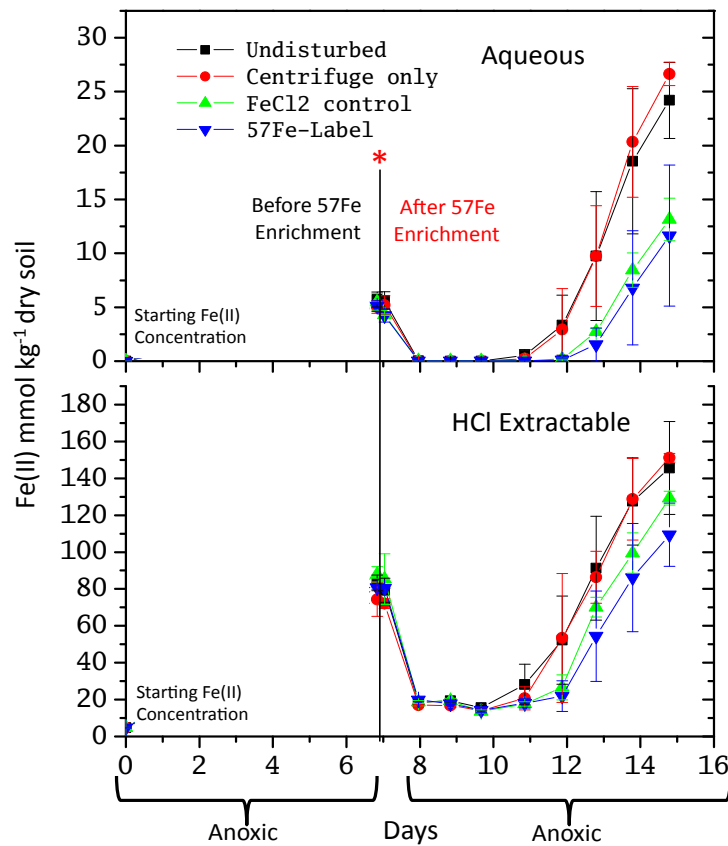


Figure. 3.3. Enriched <sup>57</sup>Fe-label and control microcosm Fe(II) concentrations in the aqueous and 0.5 M HCl extractable phases. Treatments initiated at the end of the 7 d anoxic pre-incubation period included: (1) an undisturbed microcosm control (Black Square); (2) a primary, centrifuged, enriched <sup>57</sup>Fe-label treatment (Blue Triangle); (3) an analogous centrifuged, FeCl<sub>2</sub>•4HCl amended control (Green Triangle); and (4) a centrifuged-only control that did not involve removal of the original microcosm supernatant (Red Circle). The black line marked by a red star represents the division between the time before isotope addition (i.e. pre-incubation) and the time after isotope addition. The native Fe(II) concentration at 0 d is indicated by *starting Fe(II) Concentration*. Error bars represent aqueous (top) and 0.5 M HCl (bottom) extractable Fe(II) averages ±stdev (n=3).

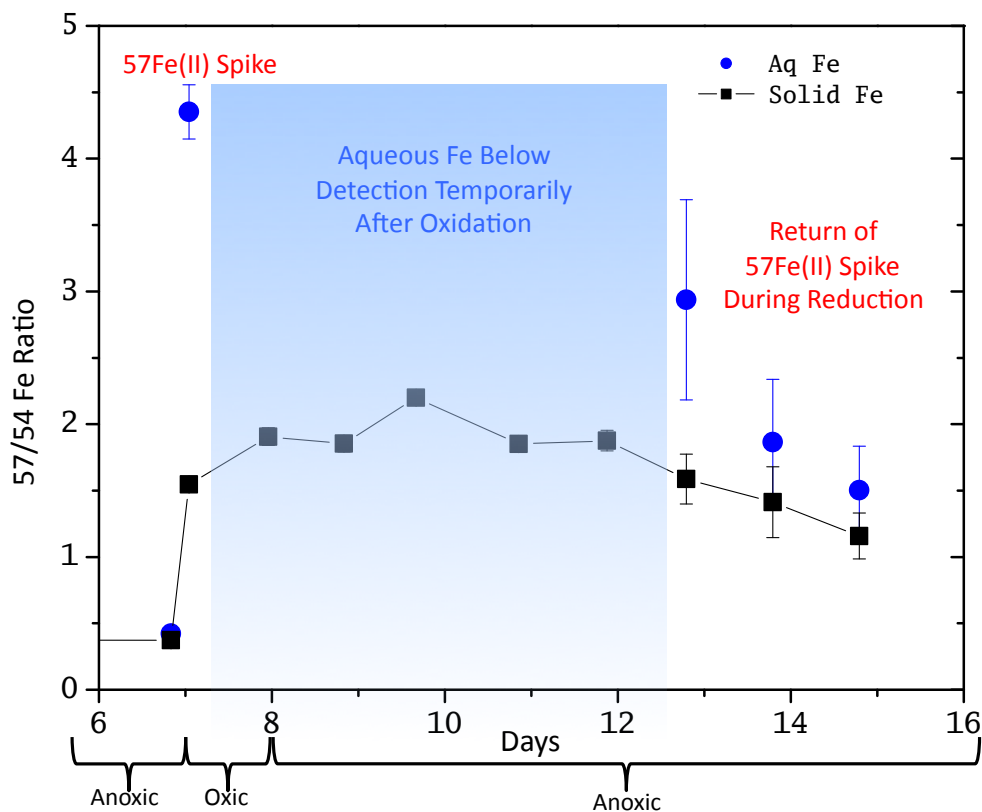


Figure. 3.4.  $^{57}/^{54}\text{Fe}$  isotope ratios in the aqueous (Aq Fe) and 0.5 M HCl extractable (Solid Fe) phases for the  $^{57}\text{Fe}$ -label treatment. X-axis shows the cycling of anoxic and oxic conditions beginning at 6 d. The  $^{57}/^{54}\text{Fe}$  isotope ratios up to 6 d represent natural abundances of  $^{57}$  and  $^{54}$  Fe isotopes in the soil. The  $^{57}/^{54}\text{Fe}$  isotope ratios were elevated after addition of the  $^{57}\text{Fe}$ -label at 7 d, following the pre-incubation period. After oxidation between 7 d and 8 d, Fe isotope ratios were below detection in the aqueous phase (shaded area). By 13 d, at the onset of Fe(III)-reduction, the  $^{57}\text{Fe}$ -label re-entered solution at a higher  $^{57}/^{54}\text{Fe}$  ratio than the solid phase, indicating preferential release of the added  $^{57}\text{Fe}$ -label during reduction of Fe(III) solid phases. Error bars represent aqueous (top) and 0.5 M HCl (bottom) extractable Fe(II) averages  $\pm$ stdev (n=3).

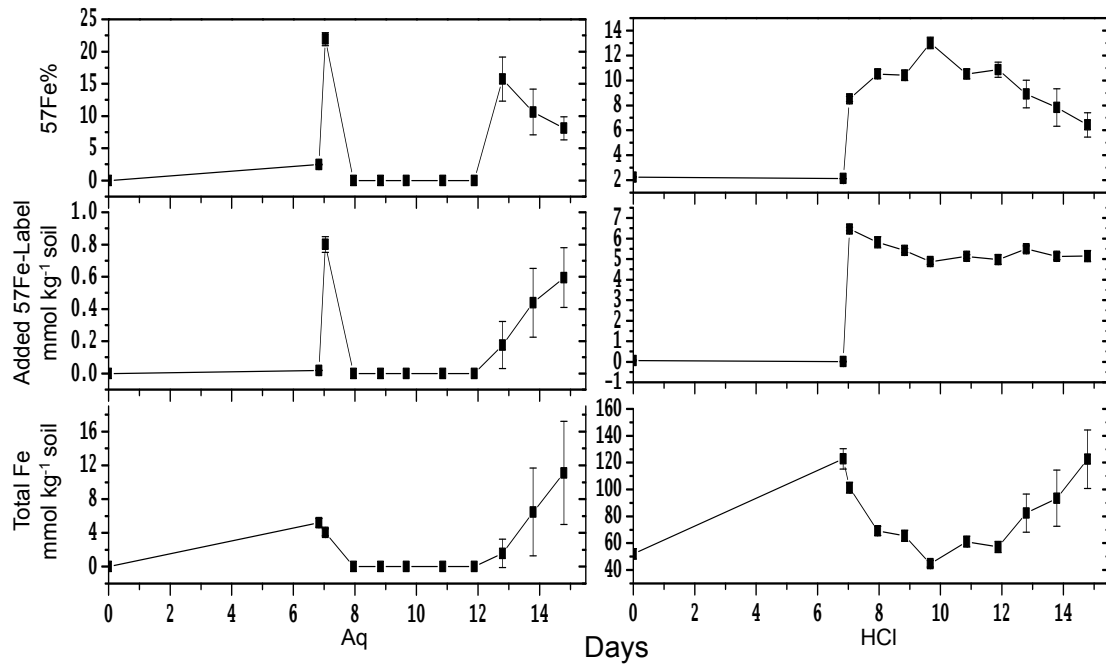


Figure 3.5. Aqueous and 0.5 M HCl-extractable %<sup>57</sup>Fe, added <sup>57</sup>Fe-label (with natural abundance <sup>57</sup>Fe subtracted) and total extractable Fe during incubation. Error bars represent aqueous (top) and 0.5 M HCl (bottom) extractable Fe(II) averages  $\pm$ stdev (n=3).

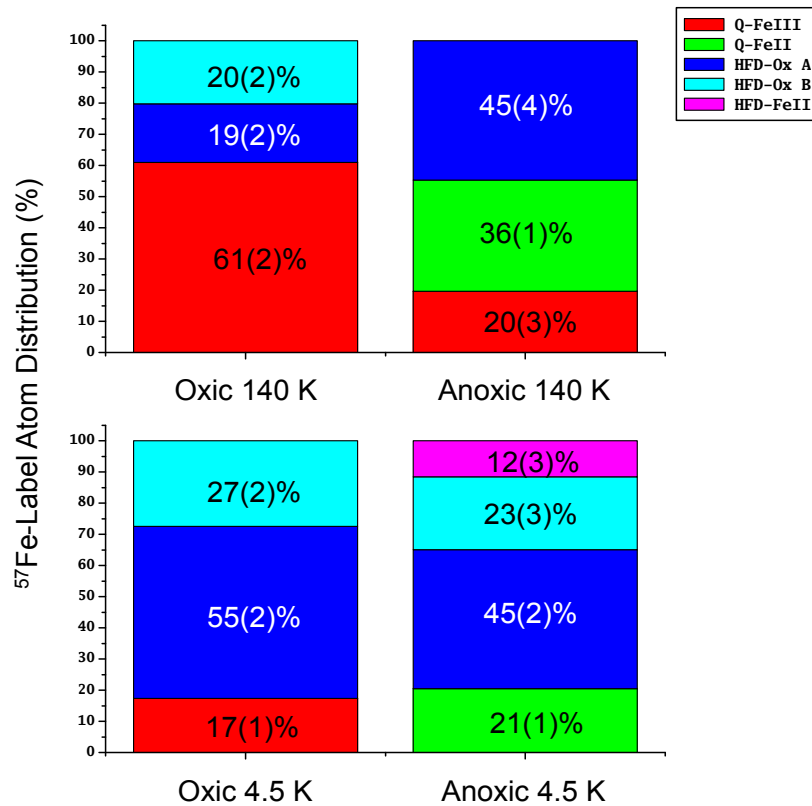


Figure 3.6.  $^{57}\text{Fe}$ -label shown as atom distributions (% total added  $^{57}\text{Fe}$  atoms) in  $^{57}\text{Fe}$ -enriched samples under oxic (8 d combined triplicates from enriched trt) and anoxic (15 d combined triplicates from enriched trt) conditions, and measured by MBS at 140 and 4.5 K.  $^{57}\text{Fe}$ -label distributions were calculated by subtractive differences between MBS peak areas in enriched  $^{57}\text{Fe}$ -label and control  $\text{FeCl}_2$  spectra. Samples were collected under the same conditions for accurate comparison. Standard errors on the last digits, as reported after Voight-based fitting in Recoil, are given in concise form.

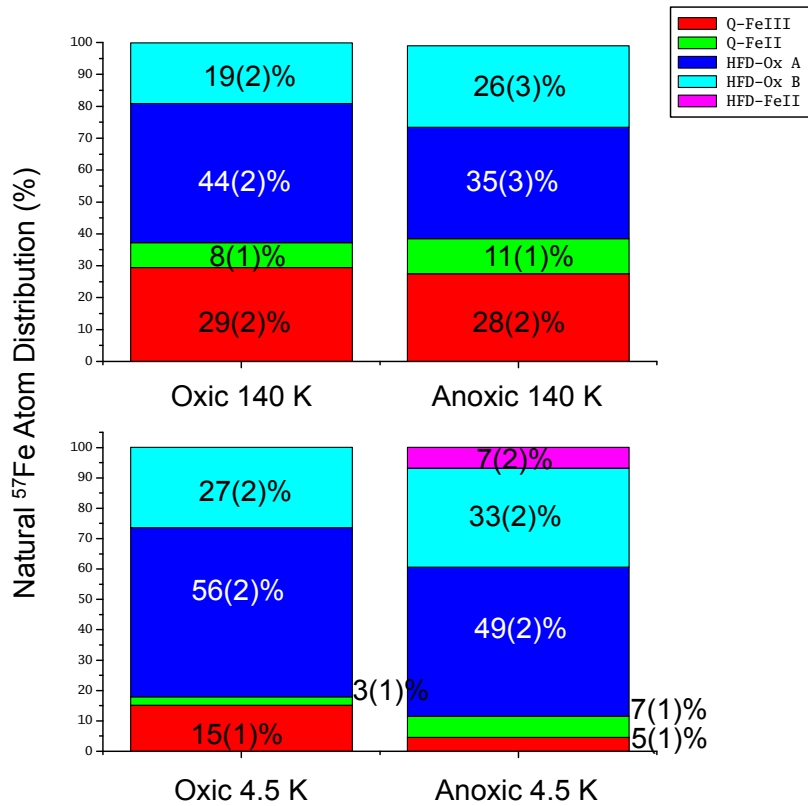


Figure 3.7. Natural abundance  $^{57}\text{Fe}$  shown as atom distributions in  $\text{FeCl}_2$  control samples (not enriched with added  $^{57}\text{Fe}$ ) under oxic (8 d mixed replicates from control trt) and anoxic (15 d mixed replicates from control trt) conditions, and measured by MBS at 140 and 4.5 K. Samples were collected under the same conditions for accurate comparison. Proportions and associated error values were taken directly from Recoil output. Standard errors on the last digits, as reported after Voight-based fitting in Recoil, are given in concise form.

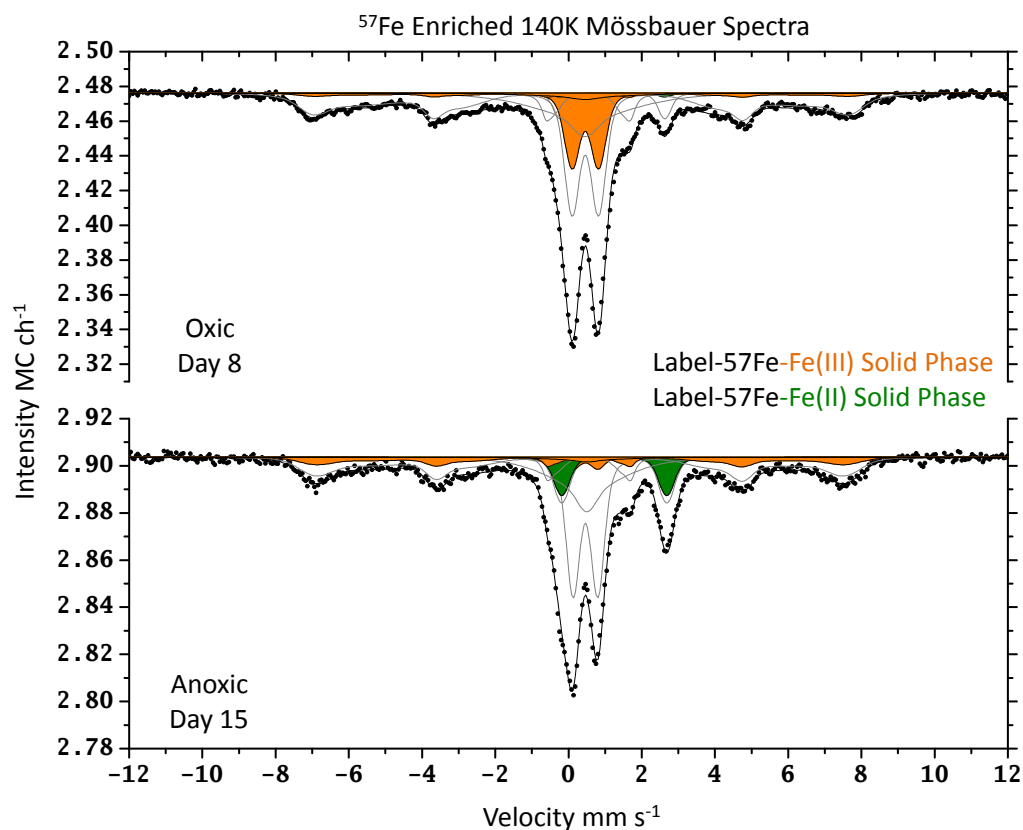


Fig 3.8.  $^{57}\text{Fe}$ -Mössbauer spectra collected at 140 K after calculating differences between treatment and control  $^{57}\text{Fe}$ -site populations. Raw spectral data points are shown as black dots. Modeled Fe site populations are indicated as gray lines: Q-FeIII, Q-FeII, HFD-OxHy, HFD-(b)OxHy, HFD-FeII and total fit (solid black line). Shaded areas (Fe(III) (orange); Fe(II) (green)) represent accumulation of the added  $^{57}\text{Fe}$ -label compared to natural abundance  $^{57}\text{Fe}$  in portions of the spectral sites, after taking into account the difference between total concentrations of  $^{57}\text{Fe}$  in the treatment and the control samples. Following oxidation, much of the  $^{57}\text{Fe}$ -label was part of highly disordered Fe(III) in the solid phase, indicated by the large shaded area (orange) in the Fe(III) central doublet under oxic conditions (top panel). After 7 days under anoxic

conditions, disordered Fe(III) was reduced to Fe(II) (green shaded area), along with a relative increase in the sextet that indicates labeled Fe(III)-(oxyhydr)oxides had become more crystalline during reducing conditions (bottom panel).

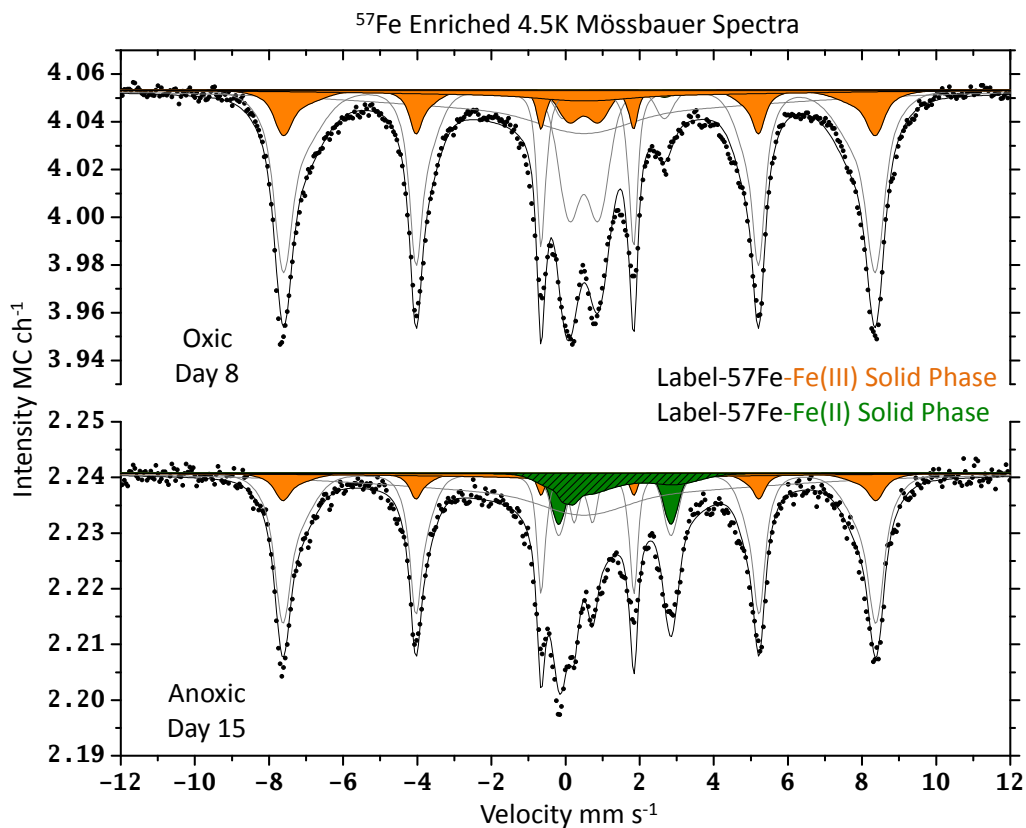


Fig 3.9.  $^{57}\text{Fe}$ -Mössbauer spectra collected at 4.5 K after calculating differences between treatment and control  $^{57}\text{Fe}$ -site populations. Raw spectral data points are shown as black dots. Modeled Fe site populations are indicated as gray lines: Q-FeIII, Q-FeII, HFD-OxHy, HFD-(b)OxHy, HFD-FeII and total fit (solid black line). Shaded areas (Fe(III) (orange); Fe(II) (green)) represent accumulation of the added  $^{57}\text{Fe}$ -label compared to natural abundance  $^{57}\text{Fe}$  in portions of the spectral sites, after taking into account the difference between total concentrations of  $^{57}\text{Fe}$  in the treatment and the control samples. At 4.5 K, a portion of the  $^{57}\text{Fe}$ -label that existed as Fe(II) was magnetically ordered (green shaded area with black cross-hatches).

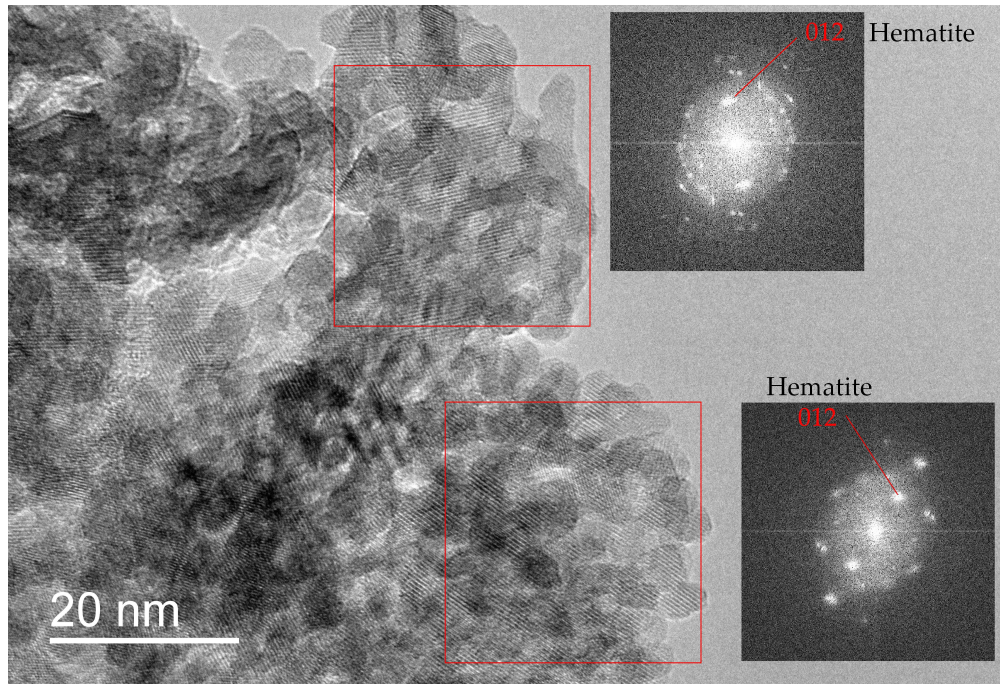


Figure 3.10. High resolution electron micrograph of representative cluster of 3-8 nm Fe-(oxyhydr)oxides collected from undisturbed, oxic, soil microcosm. Selective area electron diffraction patterns (SAED) of mineral assembly show constructive signals that are similar to the 012 reflections of hematite (spot size diameter = 25 nm), though the exact mineral speciation could not be delineated or confirmed.

APPENDIX

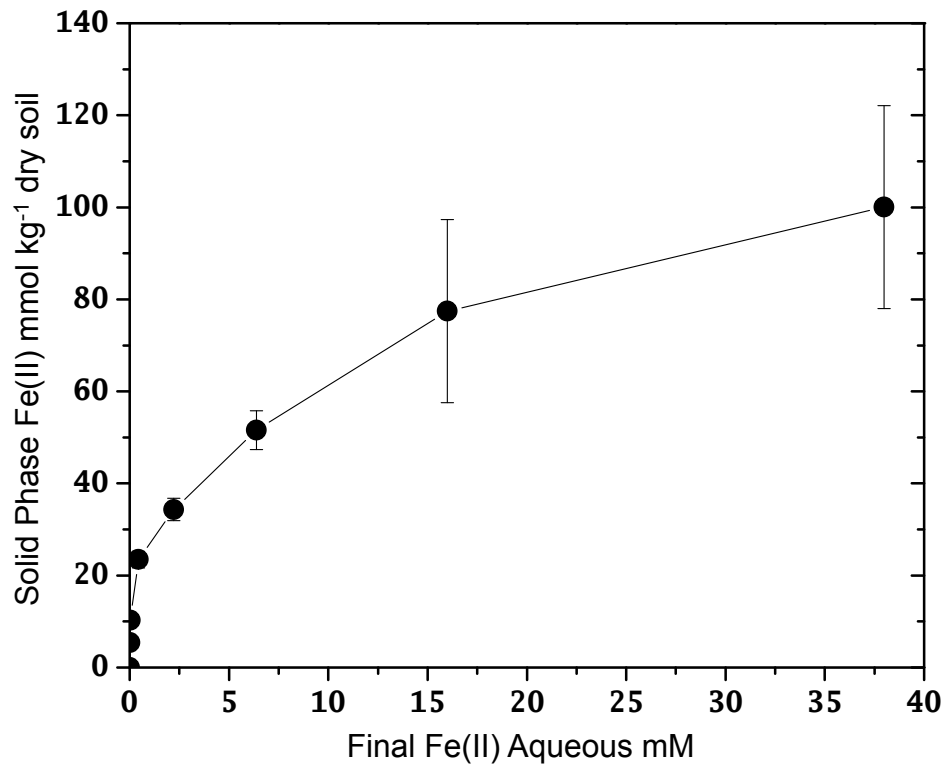
Appx. Table 3.1. MBS parameters table.

Appx. Table 3.1.: Mössbauer parameters (see Main Figures 3.6. – 3.9.)

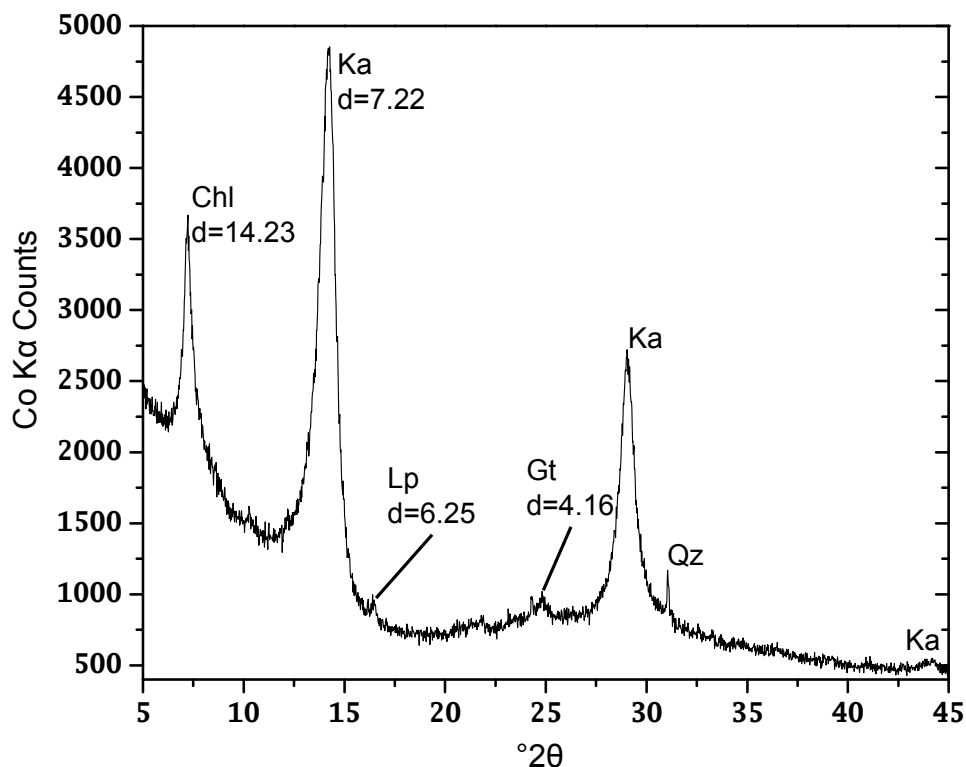
Sample	Temp K	Phase	Spectral Area		$\delta_0$	$\epsilon_0$	P	$\Delta$ or H	$\sigma$	Red- $X^2$	<CS>	< $\epsilon$ >	<QS> or <H>	s.d.
			MC*mm/s	%	mm/s	mm/s	%	mm/s or T	mm/s or T		mm/s	mm/s	mm/s or T	mm/s or T
<b>57Fe-Label Oxic</b> (2Q, 2H)	140	Q-Fe <sup>III</sup>	0.136(5)	37.2(11)	0.459(3)	n/a	100*	0.723(5)	0.326(10)	1.357	0.459	n/a	0.726	0.319
		Q-Fe <sup>II</sup>	0.018(2)	4.99(42)	1.195(16)	n/a	100*	2.87(3)	0.258(38)		1.195	n/a	2.87	0.258
		HFD-OxHy	0.141(5)	38.3(11)	0.443(17)	-0.099(16)	25.87*	45.39(22)	2.04(30)		0.443	-0.099	40.23	7.221
(BG = 2.476 MC/ch)							74(5)	38.43(91)	7.51(52)				(Peak H 45.13 T)	
		HFD-(b)OxHy	0.071(5)	19.5(11)	0.455(28)	0*	100*	0*	11.3(15)		0.455	0	9.031	6.823
<b>57Fe-Label Oxic</b> (2Q, 2H)	4.5	Q-Fe <sup>III</sup>	0.107(3)	15.0(4)	0.494(11)	n/a	100*	0.781(17)	0.499(19)	3.723	0.494	n/a	0.806	0.457
		Q-Fe <sup>II</sup>	0.020(2)	2.81(30)	1.302(34)	n/a	100*	2.73(7)	0.364(59)		1.302	n/a	2.73	0.364
		HFD-OxHy	0.396(6)	55.5(9)	0.480(2)	-0.107(2)	42.82*	49.55(3)	1.06(5)		0.48	-0.107	48.52	3.147
(BG = 4.053 MC/ch)							57(2)	47.74(14)	3.88(13)				(Peak H 49.51 T)	
		HFD-(b)OxHy	0.191(10)	26.7(10)	0.5*	0*	100*	0*	42.2(29)		0.5	0	33.7	25.46
<b>57Fe-Label Anoxic</b> (2Q, 2H)	140	Q-Fe <sup>III</sup>	0.071(7)	26.3(20)	0.462(5)	n/a	100*	0.676(11)	0.282(23)	0.87	0.462	n/a	0.678	0.278
		Q-Fe <sup>II</sup>	0.046(2)	17.2(8)	1.25(1)	n/a	100*	2.86(2)	0.348(21)		1.25	n/a	2.86	0.348
		HFD-OxHy	0.102(5)	38.1(17)	0.441(23)	-0.123(23)	40.74*	44.80(25)	2.50(46)		0.441	-0.123	39.49	7.34
(BG = 2.904 MC/ch)							59(13)	35.8(21)	7.3(17)				(Peak H 44.55 T)	
		HFD-(b)OxHy	0.049(6)	18.4(19)	0.5*	0*	100*	0*	8.6(16)		0.5	0	6.85	5.179
<b>57Fe-Label Anoxic</b> (2Q, 3H)	4.5	Q-Fe <sup>III</sup>	0.008(1)	3.41(50)	0.48*	n/a	100*	0.5*	0.15*	1.285	0.48	n/a	0.5	0.15
		Q-Fe <sup>II</sup>	0.024(1)	9.88(58)	1.331*	n/a	100*	3.027*	0.306*		1.331	n/a	3.03	0.306
		HFD-OxHy	0.117(2)	47.4(14)	0.483*	-0.109*	40.16*	49.658*	0.866*		0.483	-0.109	48.9	2.57
(BG = 2.241 MC/ch)							59.84*	48.39*	3.14*				(Peak H 49.62 T)	
		HFD-(b)OxHy	0.07(1)	28.4(16)	0.5*	0*	100*	0*	39.534*		0.5	0	31.54	23.83
		HFD-Fe <sup>I</sup>	0.027(4)	10.9(15)	1.079*	1*	100*	5.4*	3.9*		1.079	1	5.7	3.45

Appx. Table 3.1.: Mössbauer parameters (see Main Figures 3.6. – 3.9.)

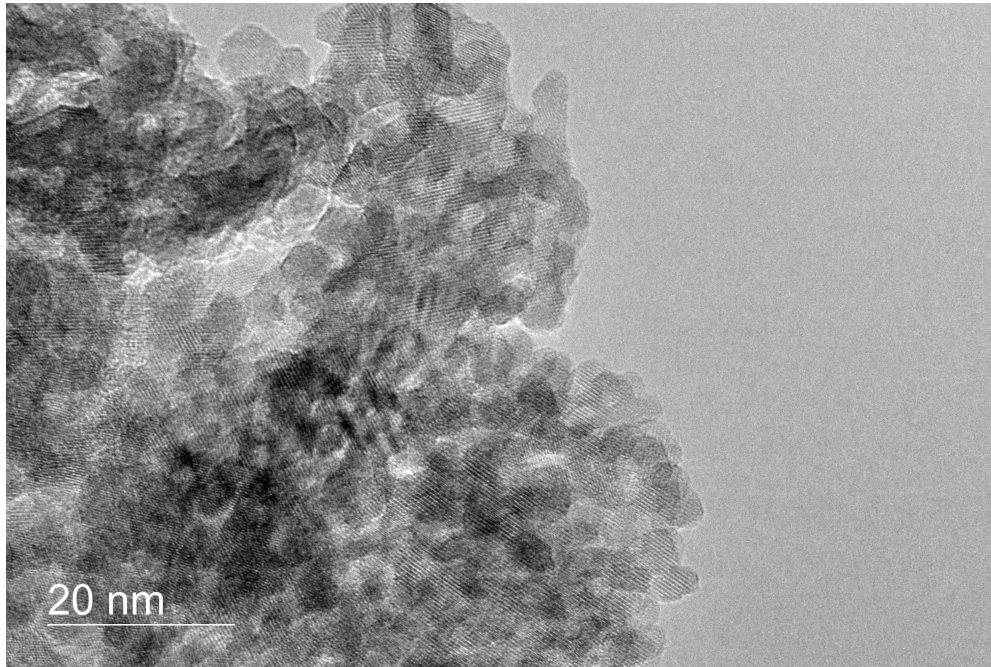
Sample	Temp K	Phase	Spectral Area		$\delta_0$ mm/s	$\epsilon_0$ mm/s	P %	$\Delta$ or H mm/s or T	$\sigma$ mm/s or T	Red- $X^2$	$\langle CS \rangle$ mm/s	$\langle \epsilon \rangle$ mm/s	$\langle QS \rangle$ or $\langle H \rangle$ mm/s or T	s.d. mm/s or T
			MC*mm/s	%										
<b>FeCl2 Cont. Oxid</b> (2Q, 2H)	140	Q-Fe <sup>III</sup>	0.059(5)	29.4(18)	0.458(6)	n/a	100*	0.68(1)	0.288(20)	0.898	0.458	n/a	0.683	0.284
		Q-Fe <sup>II</sup>	0.016(2)	7.78(73)	1.22(2)	n/a	100*	2.86(4)	0.321(48)		1.21	n/a	2.86	0.321
		HFD-OxHy	0.088(4)	43.7(18)	0.459(24)	-0.103(23)	28.85*	45.14(31)	2.17(42)	0.459	-0.103	40.63	7.243	
		HFD-(b)OxHy	0.038(4)	19.0(19)	0.5*	0*	71(7)	38.8(13)	7.76(79)	0.5	0	(Peak H 44.91 T)	8	6.047
<b>FeCl2 Cont. Oxid</b> (2Q, 2H)	4.5	Q-Fe <sup>III</sup>	0.036(2)	15.1(8)	0.469(19)	n/a	100*	0.707(24)	0.475(35)	1.309	0.469	n/a	0.736	0.43
		Q-Fe <sup>II</sup>	0.007(1)	2.85(57)	1.21(3)	n/a	100*	2.88(6)	0.203(80)		1.21	n/a	2.88	0.203
		HFD-OxHy	0.134(4)	55.6(18)	0.481(4)	-0.118(4)	47.87*	49.65(6)	0.943(92)	0.481	-0.118	48.93	2.654	
		HFD-(b)OxHy	0.064(7)	26.5(21)	0.5*	0*	52(5)	48.26(28)	3.43(29)	0.5	0	(Peak H 49.62 T)	34.39	25.98
<b>FeCl2 Cont. Anoxic</b> (2Q, 2H)	140	Q-Fe <sup>III</sup>	0.061(2)	27.5(17)	0.455(8)	n/a	100*	0.638(11)	0.315(15)	0.758	0.455	n/a	0.643	0.304
		Q-Fe <sup>II</sup>	0.027(2)	11(1)	1.24(1)	n/a	100*	2.85(3)	0.311(35)		1.24	n/a	2.85	0.311
		HFD-OxHy	0.077(7)	34.9(25)	0.471(25)	-0.096(24)	32.98*	46.27(36)	1.92(70)	0.471	-0.096	42.75	4.837	
		HFD-(b)OxHy	0.06(1)	25.6(34)	0.5*	0*	67(21)	41(2)	4.9(10)	0.5	0	(Peak H 45.92 T)	29.33	22.16
<b>FeCl2 Cont. Anoxic</b> (2Q, 3H)	4.5	Q-Fe <sup>III</sup>	0.009(1)	4.57(67)	0.48*	n/a	100*	0.5*	0.15*	1.198	0.48	n/a	0.5	0.15
		Q-Fe <sup>II</sup>	0.014(2)	6.96(94)	1.331*	n/a	100*	2.90(5)	0.334(60)		1.33	n/a	2.9	0.33
		HFD-OxHy	0.096(2)	49.1(20)	0.483*	-0.109	40.16*	49.66*	0.866*	0.483	-0.109	48.9	2.567	
		HFD-(b)OxHy	0.064(6)	32.6(21)	0.5*	0*	59.84*	48.39*	3.14*	0.5	0	(Peak H 49.62 T)	31.54	23.83
		HFD-Fe <sup>II</sup>	0.013(5)	6.8(22)	1.079*	1*	100*	5.4*	3.9*	1.08	1	5.7	3.454	



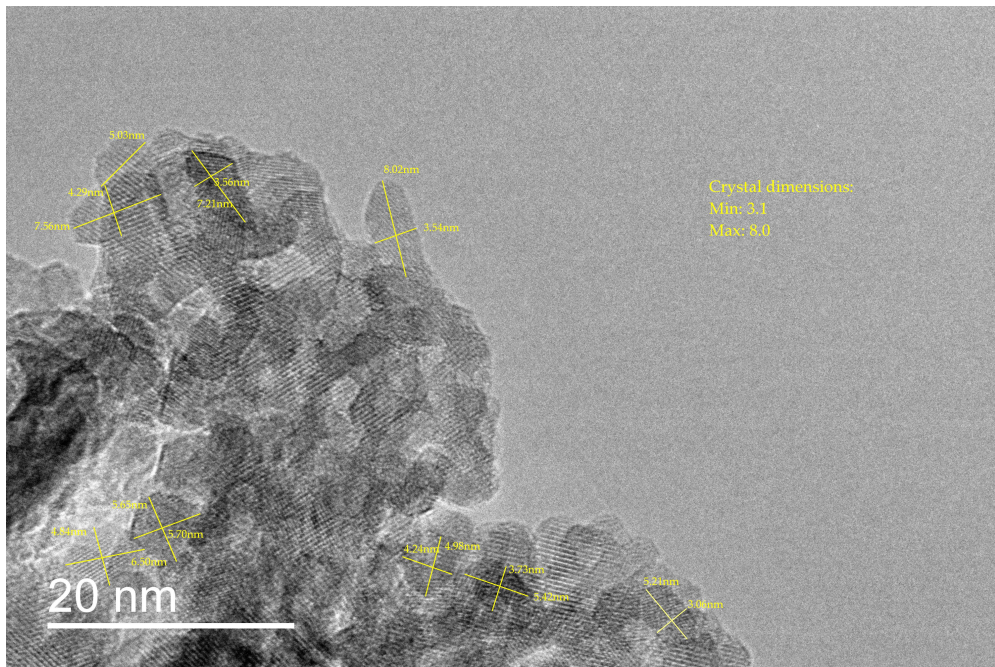
Appx. Figure 3.1. Fe(II)-sorption isotherm for LCZO soil using aqueous Fe(II) concentrations ranging from 0 to 50 mM (as  $\text{FeCl}_2 \cdot 4\text{HCl}$ ) under anoxic conditions. Soils were mixed in a 10:1 solution:solid ratio for 2 h on a rotary shaker at 200 rpm with 25 mM MES buffer adjusted to final pH 6.0 and final ionic strength of standard solutions was adjusted with KCl to equal that of the 50 mM aqueous Fe(II) standard. Solid and aqueous phase Fe(II) was measured by a modified ferrozine method after centrifugation at 28,000 *rcf* for 15 min., and extraction via 0.5M HCl, respectively.



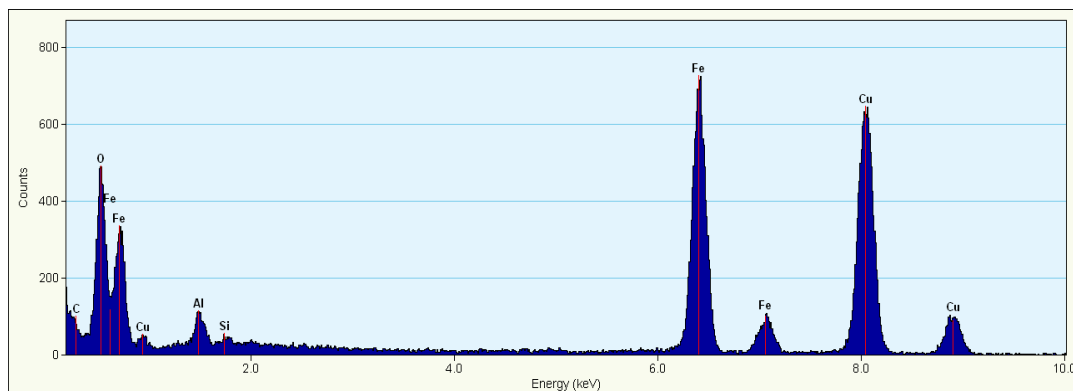
Appx. Figure 3.2. XRD was performed on the air-dry starting material using a Bruker Advance diffractometer with a Co-K $\alpha$  source. Mineral phases (d-spacing in Å) are indicated as follows: quartz (Qz); kaolinite (Ka); chlorite (Chl); lepidocrocite (Lp); and goethite (Gt). Clay suspensions were prepared by centrifugation, followed by vacuum filtration and filter-clay-transfer to glass slides, avoiding preferential sedimentation. Scan parameters included a 0.02° increment at 2°/min using a 0.6 mm slit and a 2 $\theta$  interval of 2-70°. Data analysis was performed using the EVA software package (Bruker).



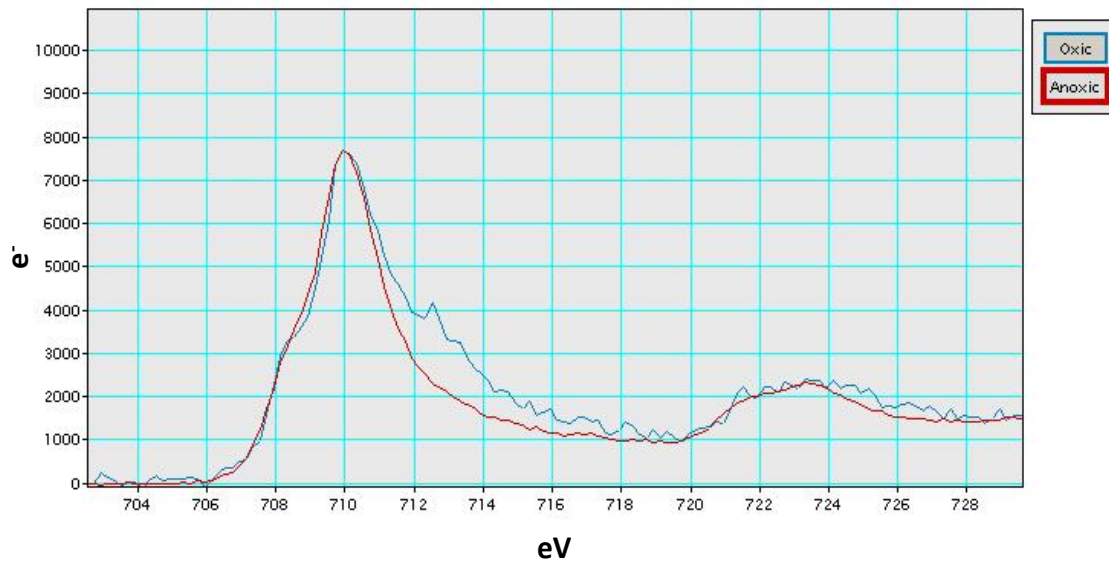
Appx. Figure 3.3. High resolution electron micrograph of representative cluster of 3-8 nm Fe-(oxyhydr)oxides collected from undisturbed, oxic, soil microcosm without post-imaging analysis.



Appx. Figure 3.4. High resolution electron micrograph of representative cluster of 3-8 nm Fe-(oxyhydr)oxides collected from undisturbed, oxic, soil microcosm with dimensional analysis after imaging.



Appx. Figure 3.5. Energy dispersive X-ray spectrum (EDXS) of nano-Fe cluster collected from undisturbed, oxic, soil microcosm (spot size diameter = 25 nm; top, red square Fig. 3.10.).



Appx. Figure 3.6. Electron energy loss spectrum (EELS) of nano-Fe cluster collected from undisturbed oxic (blue line) and anoxic (red line) soil microcosms (spot size diameter = 25 nm). A slightly higher, more broad, shoulder on the anoxic Fe *L3* peak (706-716 eV) between 708 and 710 eV indicates higher proportion of Fe(II) in the solid phase compared to the oxic sample. However, the *L3* peak difference between oxic and anoxic samples is too small to be used for quantitative evaluation of Fe(II)/(III) ratios.

## CHAPTER 4

# CHARACTERIZATION OF IRON SOLID PHASES IN A REDOX-DYNAMIC TROPICAL FOREST SOIL<sup>1</sup>

---

<sup>1</sup>Wilmoth, J.L., P. Schroeder and A. Thompson. To be submitted to the Journal of *Clays and Clay Minerals*.

## ABSTRACT

Understanding the physical characteristics of soil iron minerals can facilitate the prediction of biogeochemical processes at the landscape scale. We studied an upland valley of the Bisley Watershed (LEF), Luquillo Critical Zone Observatory, PR in order to advance our understanding of the speciation and crystalline properties of Fe minerals in redox-dynamic tropical soils that can impact microbial metabolism, and nutrient and C cycling. Geochemical and physical properties of the soils were measured with  $^{57}\text{Fe}$ -Mössbauer spectroscopy (MBS) (at 295, 140, 77, and 20 K), X-ray diffraction (XRD) and selective and total chemical extractions. XRD patterns of the Fe minerals goethite and lepidocrocite are evident, including patterns for quartz, kaolinite and feldspar. We find for the MBS parameters an average of  $2.8 \pm 1.3\%$   $\text{Fe}^{\text{II}}$  and  $16 \pm 2.9\%$   $\text{Fe}^{\text{III}}$  doublets with quadrupole splitting parameters  $\text{CS} = 0.45 \pm 0.02 \text{ mm s}^{-1}$ ,  $\text{QS} = 0.75 \pm 0.03 \text{ mm s}^{-1}$  and  $\text{CS} = 1.16 \pm 0.05 \text{ mm s}^{-1}$ ,  $\text{QS} = 2.88 \pm 0.13 \text{ mm s}^{-1}$  respectively. The dominant Fe-(oxyhydr)oxide sextet in the spectra accounts for  $77.7 \pm 4.7\%$  of the total Fe with hyperfine distribution parameters  $\text{HFD} = 48.18 \pm 0.16 \text{ T}$  and  $\text{QS} = -0.12 \pm 0.01 \text{ mm s}^{-1}$ . By comparing data from chemical, XRD and MBS analyses, we show that increases in MBS Fe(II) were positively correlated with increases in XRD lepidocrocite:goethite ratios and citrate-ascorbate extractable Fe.

## INTRODUCTION

The physical properties of Fe solid phases in soil, such as their size, structure, surface area and atomic order, can regulate the bioavailability of essential compounds (e.g. OC and P) (Hutchison and Hesterberg, 2004; Scharer *et al.*, 2009; Hiemstra *et al.*, 2013; Mallet *et al.*, 2013; Saidy *et al.*, 2013) and retention of organic and inorganic contaminants (Hanna, 2007; Wang *et al.*, 2008; Jiskra *et al.*, 2012), and are both dependent and influential upon the rate and extent of microbially mediated Fe-redox transformations (Zachara *et al.*, 1998; Hansel *et al.*, 2004; Roden, 2006; Bonneville *et al.*, 2009; Coby *et al.*, 2011; Li *et al.*, 2012). Tropical soils that are highly weathered and experience changes in redox conditions due to wetting and drying cycles (i.e. transitions between atm O<sub>2</sub> depletion and atm O<sub>2</sub> saturation) are of great interest because Fe minerals are relatively abundant, facilitate P immobilization under oxic conditions and release limited P and are coupled to OC oxidation during anoxic conditions (Miller *et al.*, 2001; Chacon *et al.*, 2005; Peretyazhko and Sposito, 2005; Liptzin and Silver, 2009). Soils of the Bisley Watershed, Luquillo Experimental Forest (LEF), Puerto Rico, as part of the NSF sponsored Long Term Ecological Research Program, have been actively studied to examine the effects of redox transitions on microbial community structure and activity, Fe, C and P cycling, all of which are thought to be influenced by the crystalline properties of Fe minerals in these tropical forest soils (Peretyazhko and Sposito, 2005; DeAngelis *et al.*, 2010; Dubinsky *et al.*, 2010; Liptzin *et al.*, 2011; DeAngelis and Firestone, 2012; Minyard *et al.*, 2012). However, little information exists on the molecular characteristics of Fe minerals as they occur in these redox-dynamic soils. A microscale evaluation of Fe solid phases can improve modeling of coupled changes in Fe mineral transformations, microbial community structure and activity, and nutrient and C cycling at the ecosystem level.

Because the Fe forms in soils are generally difficult to physically separate and isolate for direct characterization (Bigham *et al.*, 1978; Wu *et al.*, 2012; Regelink *et al.*, 2013), operationally defined chemical extractions have been used to assess their order, composition and abundance. Extraction of soil Fe(II) and Fe(III) with dithionite-citrate-bicarbonate (DCB) (Loeppert and Inskeep, 1996) gives an estimate of the abundance of total reducible Fe oxides, whereas acid-ammonium-oxalate (AAO) (McKeague and Day, 1966) and citrate-ascorbic acid (CA) (Reyes and Torrent, 1997) can be used to estimate abundance of short-range-ordered (SRO) Fe oxides. Measurements of Al, Si, Mn and P in these extractions have been used to estimate the accompanying elemental substitution in and sorption to Fe oxides (Bigham *et al.*, 1978; Peretyazhko and Sposito, 2005). Alternatively, non-destructive techniques (i.e. techniques that do not significantly alter the relevant chemical and physical properties of the analyte) can be used for *in situ* analysis of Fe-bearing minerals. X-ray diffraction (XRD) is a non-destructive technique that generally yields information on the structure and relative abundance of many crystalline minerals in complex mixtures, but may be insufficient to study the Fe solid phases of interest due to the distribution, concentration and short-range atomic order of such phases in soils (Schwertmann *et al.*, 1982; Refait *et al.*, 2001). These properties may explain observed differences between abundance of reducible Fe oxides derived from DCB extractions and abundance of Fe oxides detected by XRD in highly weathered soils (Bigham *et al.*, 1978; Peretyazhko and Sposito, 2005).

Since Fe plays an important role in tropical soils that undergo oxic/anoxic transitions, the solid phase composition is an important ecosystem variable to quantify. Previous detailed characterizations of Fe in the humid tropics have utilized a combination of analyses including operationally-defined extractions, XRD and Mössbauer spectroscopy (MBS) as measures of

complex Fe assemblages and crystallinity (Brinkman *et al.*, 1973; Goodman and Lewis, 1981; Degraeve *et al.*, 1988; Chorover and Sposito, 1995; Eyre and Dickson, 1995; Fritsch *et al.*, 2005; Peretyazhko and Sposito, 2005). Since a relatively large proportion of the Fe minerals in the humid tropics are short-range-ordered (SRO) based on chemical extractions, use of XRD as the only solid phase analysis may be less useful as characterization technique. Here, techniques such as Mössbauer spectroscopy (MBS) or synchrotron-based X-ray Adsorption spectroscopy (XAS) can provide information on the structure and composition of Fe phases irrespective of their overall crystallinity (Refait *et al.*, 2001). Of these two techniques, MBS offers a unique view of specifically the Fe minerals. MBS is a non-destructive technique that allows for the exclusive measurement of  $^{57}\text{Fe}$  in complex samples with the capability of identifying and examining finely separated, short-range-order and substituted Fe solid phases (Bigham *et al.*, 1978; Schwertmann *et al.*, 1982; Amarasiriwardena *et al.*, 1986; Fontes *et al.*, 1992; Komlos *et al.*, 2007; Mikutta *et al.*, 2008; Murad, 2010; Thompson *et al.*, 2011; Larese-Casanova *et al.*, 2012; Dhakal *et al.*, 2013).

Importantly, there are likely broad differences in Fe composition across soils rich in SRO phases that cannot be captured using any single conventional technique alone. We expect that a combined analysis using chemical extraction, XRD and MBS should reveal more differences and critical information between samples, where isolated techniques likely would not. Previous characterizations of Fe in surface soils of the LEF have included operational extractions as measures of Fe oxide crystallinity and solid phase analysis with XRD (Peretyazhko and Sposito, 2005). A relatively large proportion of the Fe minerals has been shown to be associated with Fe(III) oxides of short-range-order based on chemical extractions, with the constituent solid phase(s) remaining unresolved using Cu- $\alpha$  XRD (Peretyazhko and Sposito, 2005).

Recognizing the important and complex role of Fe in tropical soils that undergo aerobic/anaerobic transitions, what is the Fe solid phase distribution in such systems and what information regarding reactivity can be deduced from the constituent minerals based on relevant solid phase and geochemical/physical measures (structure, size, atomic order, valence etc.)? We characterized the Fe solid phases in 18 separate landscape positions across an upland valley site of the Bisley Watershed (LEF), Luquillo Critical Zone Observatory, PR using selective chemical extractions (oxalate, citrate-ascorbate, and dithionate), XRD, and MBS in order to address this question, with the aim of advancing our understanding of the speciation and crystalline properties of Fe minerals in redox-dynamic soils that can impact microbial metabolism, and nutrient and C cycling.

## MATERIALS AND METHODS

### Field Sampling and Storage

Soil samples were collected from the Bisley Watershed within the Luquillo Experimental Forest, Puerto Rico. Soils are classified as very-fine parasesquic, isohyperthermic Typic Haplohumults (Huffaker, 2002). Field plots (1.25 m<sup>2</sup>) were established within an upland valley site measuring 20 x 30 m, and separated by a minimum distance of 3 m (Hall *et al.*, 2013). Approximately 100 g field-moist soil was collected from each of 18 plots using a 2.2 cm diameter core down to 20 cm. This soil was homogenized, sealed in plastic bags and immediately flash-frozen with dry ice. The soils were placed in an icebox, then shipped overnight to the University of Georgia and stored in a -20°C freezer before analysis.

### Sample Preparations

Prior to all solid-state and chemical analyses, the *ca.* 100 g frozen samples were prepared by thawing for 12 hr in their original, open plastic bags which had been gas evacuated and moved into an anoxic glove box (Coy Laboratories) (evacuation at 3 cycles; 2x [vacuum followed by N<sub>2</sub>] and 1x [vacuum followed by N<sub>2</sub>-10% H<sub>2</sub>]) under a N<sub>2</sub>-H<sub>2</sub> atmosphere (96% N<sub>2</sub> : 4% H<sub>2</sub>). Approximately 70 g of each 100 g moist sample was pushed through a 2 mm sieve in the glove box. Half of the sieved material was freeze-dried and the other half was left at field-moist conditions, while the non-separated material was stored at -20°C. All 18 samples were subjected to chemical extractions (see section 2.3 below) and six freeze-dried samples (plots 1, 2, 4, 7, 9 and 18) were analyzed by XRD and MBS (see below).

### Chemical Extractions

Freeze-dried and field-moist soil samples were analyzed for operationally defined Fe pools using acid-ammonium-oxalate (AAO) (Tamms Reagent, SSSA) and citrate-ascorbic acid (CA) (Reyes and Torrent, 1997) extractions for amorphous Fe-oxides, dithionite-citrate-bicarbonate (DCB) for reducible Fe-oxides and a 0.5 M HCl (Peretyazhko and Sposito, 2005) extraction for labile Fe(II) and Fe(III). Round bottom 50 ml centrifuge tubes were weighed and filled with 30 ml of one of three extractant solutions as stated above. The filled, open tubes were gas evacuated in the anoxic gas chamber and 1 g of freeze-dried or field-moist samples was placed in each of the three extractants for Fe characterization. Each of the samples (n=18) was extracted in duplicate. Centrifuge tubes were sealed with a cap and rubber gasket in the glove box after soil had been added to extractants. Filled sample tubes were then taken from the glove box, immediately weighed, and extracted on a horizontal shaker. Samples extracted in acid ammonium oxalate and 0.5 M HCl were extracted for 2 hours in the dark, and those in citrate-

ascorbic acid for 16 hours in the dark. Once the soils had been extracted, they were separated from the supernatant by centrifugation at 32,600g for 20 min. Extract solutions were decanted into 50 ml polypropylene tubes in an anoxic glove box, then stored and at 4 °C in the dark. Freeze-dried samples (n=18) were dissolved for total soil Fe analysis using lithium(Li)-metaborate fusion and digestion (ALS Minerals) followed by analysis via ICP-MS.

### XRD

XRD was performed on the six selected samples on a Bruker Advance diffractometer with a Co-K $\alpha$  source. Bulk and clay-size samples were prepared according to Moore and Reynolds (1997). Clay suspensions were prepared by centrifugation, followed by vacuum filtration and filter-clay-transfer to glass slides, avoiding preferential sedimentation. The clay mounts were exposed to ethylene glycol treatment overnight prior to analysis. Scan parameters included a 0.01° increment at 1°/min using a 1 mm slit for bulk powder (70  $\mu$ m size) mounts, a 0.02° increment at 2°/min using a 0.6 mm slit for glass-slide clay mounts, and a 2 $\theta$  interval of 2-70° for all scans. Data analysis was performed using the EVA software package (Bruker). All similar primary mineral peaks were integrated over the same 2 $\theta$  intervals between samples and relative contributions from each phase were calculated as percentages of the total observed primary peak areas per sample. Mineral phase assignments to primary XRD lines were validated and referenced according to Chen (1977).

### <sup>57</sup>Fe-Mössbauer Spectroscopy

Spectra of the six freeze-dried samples were collected in transmission mode with a variable temperature He-cooled system and a 1024 channel detector. A <sup>57</sup>Co source (~50 mCi) embedded in a Rh matrix was used at room temperature. Velocity (i.e. gamma-ray energy) was calibrated using  $\alpha$ -Fe foil at 298 K and all center shift (CS) and peak positions are reported with

respect to this standard. The transducer was operated in constant acceleration mode and folding was performed to achieve a flat background. Mössbauer spectral fitting was performed in Recoil™ software (ISA Inc.) using the Voigt-based fitting (VBF) method of Rancourt and Ping (1991) for quadrupole splitting distributions (QSDs) and combined hyperfine field distributions (HFDs). All VBF Mössbauer parameter definitions and a description of the relevant notation are given by Rancourt and Ping (1991).

### Statistical Analyses

Fixed treatment level (i.e. extraction and wet or dry preparation) effects were tested with the ANOVA model ( $\alpha = 0.05$ ), and a full factorial design was used to test for interaction effects between treatments on the response variable and for effects between each treatment and the response variable. Tukey's Honestly Significant Difference (HSD) test was used to examine differences between extraction and preparation combinations. The Mössbauer and XRD data were analyzed with Tukey's HSD and t tests respectively. Multivariate analysis was used to study correlations ( $r$ ) between selected data sets. Statistical analyses were performed in JMP Pro 10.

## RESULTS

### Soil Fe Chemical Extractions

Differences between all plots moist or freeze-dried ( $n=18$ ) were minor overall based on Fe concentrations with no significant differences between moist or freeze-dried preparations (Fig. 4.1.). There were no significant differences detected between samples chosen for solid phase analysis ( $n = 6$ ) based on HCl, AAO, CA or DCB extractable Fe between moist and freeze-dried conditions. The samples showed  $6.12 \pm 0.82\%$  total Fe, DCB Fe to be  $1.6 \pm 0.34\%$  of total Fe, and

8.26±0.76% total Al (Appx. Table 4.1.). Treatments wet-CA and dry-AAO displayed significantly different effects on Fe extractability ( $p < 0.01$ ) for all samples (Fig. 4.2.). However, there was no significant difference observed overall between CA and AAO extractions or between wet and dry preparations for those treatments.

### XRD

The bulk XRD patterns were similar for the six selected samples (Appx. Fig. 4.1.). Common peaks include kaolinite, quartz and k-feldspar, with k-feldspar exhibiting the most variation in intensity among samples. The largest peaks in the clay size fraction result from disordered kaolinite-group minerals, with smaller contributions from chlorite and Fe-oxides goethite (Gt; ( $\alpha$ -FeOOH)) and lepidocrocite (Lp; ( $\gamma$ -FeOOH)) (Fig. 4.3.). The Lp 020 (~6.25 Å) and Gt 110 (~4.16 Å) peaks were identified as diagnostic features of these mineral phases using a Co- $\alpha$  source (Carlson and Schwertmann, 1990).

### <sup>57</sup>Fe-Mössbauer Spectroscopy

At *ca.* 20 K, doublets were assigned to clay minerals or highly disordered Fe(III) solids that displayed on average 16±2.9% Fe(III) and 2.8±1.3% Fe(II) with quadrupole parameters CS (center shift) = 0.45±0.02 mm s<sup>-1</sup>; QS (quadrupole splitting) = 0.75±0.03 mm s<sup>-1</sup> and CS = 1.16±0.05 mm s<sup>-1</sup>; QS = 2.88±0.13 mm s<sup>-1</sup> respectively (Appx. Table 4.2. and 4.3.). The Fe oxide phases that magnetically order near 20 K account for 77.7±4.7% of the total Fe with hyperfine distribution parameters  $B_{\text{hf}} = 48.18 \pm 0.16$  Tesla (T) and QS = -0.12±0.01 mm s<sup>-1</sup>. The magnetic ordering of Fe oxides first appeared at 140 K, with increases in area at *ca.* 77 K and again at *ca.* 20 K (Appx. Fig. 4.2.). To test for significant differences between Fe oxide distributions, the six plots were grouped by temperature such that each group included 140, 77 and 20 K measurements, and the magnetically ordered Fe oxide abundance means were compared.

Significant differences were observed between plot 4 (largest contribution = 81.65%) and every other plot ( $p < 0.01$ ), and also between plot 2 (smallest contribution = 63.54%) and plot 7 and 18 (second and third largest contribution = 72.62 and 69.34% respectively ( $p = < 0.01$  and  $< 0.05$  respectively)).

Our XRD analysis showed that plot 2 and 4 (P2 and P4) had the smallest and largest goethite:lepidocrocite ratios respectively, which explains the more pronounced development of the MBS sextet in P4 over P2 from 295 to 4.5 K (Fig. 4.4.). The probability distribution  $B_{hf} T^{-1}$  of P2 and P4 at 4.5 K showed that P2 had a higher probability for the 44 T site-component (attributed in part to magnetically ordered lepidocrocite) compared to P4, but a lower probability for the 48 T site-component (attributed in part to magnetically ordered goethite) compared to P4 (Fig. 4.5.). Comparison of the peak  $B_{hf}$  in T (H peak) vs. the quadrupole perturbation of the hyperfine magnetic field ( $\langle e \rangle$ ) for the sample 140, 77 and 20 K sextets and Fe-(oxyhydr)oxide standards showed that sample sextet parameters were similar to nano-goethite (Fig. 4.6.).

#### <sup>57</sup>Fe-Mössbauer, XRD and Chemical Extraction Correlations

Multivariate analysis of the XRD Fe oxide and kaolinite group relative abundances, MBS Fe(II) (20 K) and magnetically ordered Fe oxides (at 140, 77 and 20 K), total Al/Fe and mean dry-CA Fe concentrations were used to evaluate correlations ( $r$  coefficients) between selected data sets (Fig. 4.7. and Appx. Table 4.4.). Correlations with  $r > 0.75$  are observed between MBS magnetically ordered Fe oxides and Gt in XRD. The  $B_{hf}$  MBS parameter at 140 K vs XRD Gt shows  $r = -0.75$ , with lower  $r$  coefficients and alternating trends for MBS temperatures 77 and 20 K ( $r = -0.55$  and  $0.54$  respectively) (data not shown). A negative trend is observed between XRD Gt and MBS Fe(II) at 295 K ( $r = -0.81$ ), with a positive trend between XRD Lp and MBS Fe(II) at 295 K ( $r = 0.75$ ). Dry-CA extractable Fe is positively correlated with MBS Fe(II) at 295 K ( $r >$

0.77). Correlations with  $r = -0.64$ ,  $-0.63$  and  $-0.74$  were observed between dry-CA Fe and MBS Fe oxides at 140, 77 and 20 K respectively (data not shown). Total Al/Fe showed a striking correlation when compared with XRD Gt ( $r = -0.96$ ) and to a slightly lesser extent when compared with MBS magnetically ordered Fe oxide phases ( $r < -0.72$  at all temperatures). XRD kaolinite group abundance was not strongly correlated with MBS Fe(II) at 295 K or total Al/Fe.

## DISCUSSION

### Fe Chemical Extractions

Our chemical analyses of operationally-defined Fe pools showed no marked differences in extractable Fe due to freeze-drying the samples (Fig. 4.1.). We acknowledge that changes may have occurred to the samples during and immediately following excavation in the field, or possibly in the lab before processing, however, freeze-drying the field moist samples did not appear to impact the chemical characterizations overall. It is unclear why wet-CA and dry-AAO extractable Fe concentrations were significantly different. This observation suggests some interaction between freeze-drying field moist samples and selectivity of CA or AAO toward dissolution of SRO Fe. However, this interaction has little bearing on routine chemical analysis, since comparison of CA or AAO extractable Fe concentrations would generally be compared only between wet soil samples or only between dry soil samples, but not between combinations (i.e. wet-CA vs dry-AAO).

### Fe Mineral Identification and Biogeochemical Implications

The detection of both goethite and lepidocrocite in the samples at different ratios has implications for mineral phase partitioning and mineral reactivity in these wet tropical forest soils (Fig 4.3. to 4.5.). Goethite is a common stable form of Fe(III)-(oxyhydr)oxide found in

highly weathered and well-aerated soils. Lepidocrocite is a meta-stable Fe(III)-(oxyhydr)oxide similar to goethite, but tends to be more prevalent in wet and redoximorphic systems (Loeppert and Inskeep, 1996; Murad, 2010). The presence of both goethite and lepidocrocite likely reflects the wet and redox-dynamic conditions of the Bisley soils, conditions known to be affected by precipitation and microbial activity in these humid tropical forests (Liptzin *et al.*, 2011). The presence of goethite and lepidocrocite at different ratios may also be important for microbial Fe(III)-reduction in the field. When normalized for surface area, microbial Fe(III)-reduction of lepidocrocite has been shown to have a two-fold higher initial reduction rate (3 d after the onset of anoxic conditions) than goethite, based on the differences in crystalline structure of these two phases (Roden, 2006).

Although the largest peak areas detected in XRD belonged to the 1:1 clay mineral kaolinite (Fig. 4.3.), which can have minor isomorphous substitutions of Fe(III) and Fe(II) (Murad, 2010), the MBS analysis showed that on average most of the total Fe(III) (at least 78%  $Fe_T$ ) in the soils was in SRO (oxyhydr)oxide phases, not in the clay fraction (Fig. 4.4.). We did not observe any diagnostic XRD reflections for hematite using Co-K $\alpha$  radiation, and there were no hematite MBS parameters detected (i.e.  $B_{hf} \geq 50$  T at 20 and 4.5 K). The Fe(III)-(oxyhydr)oxides goethite and lepidocrocite identified by XRD cannot be conclusively assigned to the sextet or Fe(III)-doublet signals observed in our MBS analysis. Below 77 K, many crystalline, amorphous and nano Fe phases magnetically order, including those of goethite, lepidocrocite and ferrihydrite (Murad, 2010). Because the (oxyhydr)oxide Fe(III) in the Bisley soils does not show strong magnetic ordering until low temperatures and shows only one defined sextet, we cannot identify/delineate any distinct set of Fe(III) mineral phases confidently with MBS.

### Correlations Between Chemical, XRD and MBS Data

The positive correlation between XRD lepidocrocite abundance and MBS Fe(II) ( $r = 0.75$ ) perhaps implies mutual dependence on a primary redox-driving variable in the field, such as soil moisture (Fig. 4.7. and Appx. Table 4.4.). As mentioned above, both microbial Fe(III)-reduction to form Fe(II) and presence of goethite/lepidocrocite mixtures depend on wet soil conditions and redox-cycling. Although increased moisture in the field could lead to higher ratios of lepidocrocite to goethite and/or higher concentrations of Fe(II) from microbial Fe(III)-reduction separately, without codependence, there is a possibility that higher abundances of lepidocrocite facilitate Fe(III)-reduction to form Fe(II) (Roden, 2006), or alternatively that Fe(III)-reduction (increased Fe(II)) facilitates the formation of lepidocrocite during Fe mineral transformations (Loeppert and Inskeep, 1996; Tufano *et al.*, 2009; Zegeye *et al.*, 2011). Despite the exact mechanism(s) involved, which remain unclear, we observe a positive link between Fe(II) concentrations quantified by MBS and lepidocrocite:goethite ratios quantified by XRD in these highly active tropical forest soils. We also show that MBS Fe(II) is positively correlated with CA-extractable Fe ( $r = 0.78$ ), indicating that increases in Fe(II) are also linked to decreases in Fe(III) mineral crystal order (i.e. increases in reactivity toward reductive chemical dissolution) (Fig. 4.7. and Appx. Table 4.4.). A similar correlation ( $r = 0.76$ ) has been observed between abundance of Fe(III)-reducing bacteria and poorly crystalline Fe(III) in wetland soils (Weiss *et al.*, 2004). We therefore speculate that the Fe(II) measured in our MBS analysis primarily represents biogenic Fe(II) formed during microbial Fe(III)-reduction in the field.

The total Al/Fe ratio in the soil samples used in this study might be viewed as a master variable for interpreting a range of correlations (Fig. 4.7. and Appx. Table 4.4.). One such explanation of the data set, which requires the assumption that Al is substituted to some extent in

Fe oxide(s), is that as total Al/Fe increases, more Al is substituted in Fe oxides and leads to more disordered phases that cannot be detected by XRD or delineated in MBS. The Al content in soils is known to be a controlling factor on Fe oxide crystal parameters (Murad and Schwertmann, 1983; Goldberg, 1989; Masue-Slowey *et al.*, 2011). Naturally occurring Fe oxides can have relatively large Al substitutions (Kukkadapu *et al.*, 2001; Schwertman *et al.*, 2004; Murad, 2010). This is supported by increases in Al/Fe being shown to correlate strongly with decreases in MBS areas of magnetically ordered Fe oxides as well as decreases in XRD goethite abundances in our samples. We found no strong correlation between kaolinite abundance and total Al/Fe, supporting that decreases in Fe mineral crystal order that correlate with increasing total Al/Fe in the soils are due to Al substitution in Fe (oxyhydr)oxides.

Given the positive correlations between XRD goethite and MBS magnetically ordered Fe oxides, we assume that the most likely phase resulting in the distinct MBS sextet at all temperatures below 295 K is due to disordered/nano-goethite. However, we observe that the correlation between XRD goethite and MBS Fe(III) sextet drops from  $r = 0.86$  and  $0.91$  at  $140$  and  $77$  K, respectively, to  $0.76$  at  $20$  K. Given that crystalline and disordered lepidocrocites do not typically order magnetically until below  $77$  K, we speculate that this decrease in correlation between XRD goethite and MBS Fe(III) oxide is due to magnetic ordering of lepidocrocite by  $20$  K, which shares/convolutes the sextet area that is otherwise assigned primarily to goethite at higher temperatures. Finally, by comparing the samples that had the highest and lowest lepidocrocite:goethite ratios (P2 and P4 respectively) at  $4.5$  K with MBS (Fig. 4.5. and Appx. Fig. 4.3.), we can see a more prominent peak emerging in the sextet probability distribution ( $P B_{hf} T^{-1}$ ) at  $44$  T in the sample that contained more XRD-identified lepidocrocite (P2). Lepidocrocite has a  $B_{hf}$  of *ca*  $44$  T at  $4.5$  K (Murad, 2010), supporting the observation of more lepidocrocite in

sample P2 as measured by XRD (Fig. 4.3.), and that lower correlation overall between XRD goethite abundance and the MBS sextet abundance at 20 K is likely due to increases in magnetically ordered lepidocrocite (Fig. 4.7. and Appx. Table 4.4.). As noted above, MBS analysis alone was insufficient to identify lepidocrocite, even at 4.5 K. However, the correlation between XRD Fe phases and modeled MBS hyperfine distributions does offer the ability to speculate on the contribution of distinct Fe(III) populations to the MBS sextet at 4.5 K, as in the case of lepidocrocite and goethite, but with limited quantitative information that can be attributed to any particular phase.

## CONCLUSION

We studied a humid tropical rainforest soil, well documented to undergo dynamic redox transitions, in order to provide Fe solid phase distribution and reactivity measurements to improve modeling of Fe and associated biogeochemical pathways in such systems. Overall, we find no significant difference between oxalate (AAO) and ascorbate (CA) extractable Fe derived from wet vs. dry soil. XRD patterns using Co- $\alpha$  radiation show differences in Fe oxide distributions comprising lepidocrocite ( $\gamma$ -FeOOH) and goethite ( $\alpha$ -FeOOH), despite the dominant kaolinite group contribution in each sample. Development of a sextet in MBS spectra at 140 K and lower shows magnetic ordering and hyperfine parameters similar to that of naturally occurring goethite (i.e. present as Al-substituted, finely separated, and/or nanocrystalline phases) while relative contributions from Fe-substituted phyllosilicates (e.g. kaolinite group) and other Fe minerals (e.g. lepidocrocite) cannot be confidently resolved at 295, 140, 77, 20 and 4.5 K. The Fe(II) doublet in MBS spectra varies between each sample. Given the redox-dynamic nature of these soils in the field, which involve oxic/anoxic conditions, microbial Fe

reduction etc., and the ambiguity in MBS assignment of the Fe(II) phases which result from such processes, it is not possible to adequately identify the observed MBS Fe(II) doublet as phyllosilicate-Fe(II) or as Fe(II) associated with other mineral phases in this study. The ambiguity is non-trivial, particularly in redox-dynamic environments like tropical forest soils, where the co-evolution of Fe(II) and meta-stable and/or bio-reduced solid phases could indicate an ecologically significant shift in microbial metabolism and C and nutrient dynamics. However, by using chemical, XRD and MBS data together, we were able to show that increases in MBS Fe(II) were positively correlated with increases in XRD lepidocrocite:goethite ratios and citrate-ascorbate extractable Fe. Here we have demonstrated that in a redox-dynamic tropical soil, comprised of distinct Fe solid phases, and potentially of other, unidentified Fe phases, that the combination of selective extraction, Co- $k\alpha$  XRD and variable temperature  $^{57}\text{Fe}$ -MBS proved to be a useful methodology for characterizing Fe speciation and crystallinity. Future MBS analyses are encouraged to use a comprehensive temperature profile with analogous systems, as 295 K to *ca* 4.5 K spectra offer the prospect of improved characterization, especially when contributions from SRO Fe phases, lepidocrocite (Fe oxide with low magnetic ordering temperature ( $\sim 77$  K or less) in crystalline form) and biogenic solid-phase Fe(II) are suspect.

#### ACKNOWLEDGEMENTS

We thank Steven Hall and Whendee Silver for providing field samples. We would like to acknowledge Michele Scherer and Timothy Pasakarnis for collecting MBS measurements at the University of Iowa. We would also like to thank Joe Stucki, Martin and Linda Pentrak for MBS measurements including facility use and technical support at the University of Illinois Urbana-Champaign. Important funding was provided through the USDA-AFRI Soil Processes Program.

## LITERATURE CITED

- Amarasiriwardena DD, Degraeve E, Bowen LH, Weed SB. (1986). Quantitative-determination of aluminum-substituted goethite-hematite mixtures by mossbauer-spectroscopy. *Clay Clay Min.* **34**: 250-256.
- Bigham JM, Golden DC, Bowen LH, Buol SW, Weed SB. (1978). Iron-oxide mineralogy of well-drained ultisols and oxisols .1. Characterization of iron-oxides in soil clays by mossbauer-spectroscopy, x-ray-diffractometry, and selected chemical techniques. *Soil Science Society of America Journal* **42**: 816-825.
- Bonneville S, Behrends T, Van Cappellen P. (2009). Solubility and dissimilatory reduction kinetics of iron(iii) oxyhydroxides: A linear free energy relationship. *Geochim Cosmochim Acta* **73**: 5273-5282.
- Brinkman R, Jongmans AG, Miedema R, Maaskant P. (1973). Clay decomposition in seasonally wet, acid soils - micromorphological, chemical and mineralogical evidence from individual argillans. *Geoderma* **10**: 259-270.
- Carlson L, Schwertmann U. (1990). The effect of co<sub>2</sub> and oxidation rate on the formation of goethite versus lepidocrocite from an fe(ii) system at ph-6 and ph-7. *Clay Miner* **25**: 65-71.
- Chacon N, Dezzio N, Munoz B, Rodriguez JM. (2005). Implications of soil organic carbon and the biogeochemistry of iron and aluminum on soil phosphorus distribution in flooded forests of the lower orinoco river, venezuela. *Biogeochemistry* **73**: 555-566.

- Chen PY 1977. Table of key lines in x-ray powder diffraction patterns of minerals in clays and associated rocks. *In: RESOURCES, D. O. N. (ed.) Occasional Paper 21 ed. Bloomington, Indiana: Authority of the State of Indiana.*
- Chorover J, Sposito G. (1995). Colloid chemistry of kaolinitic tropical soils. *Soil Science Society of America Journal* **59**: 1558-1564.
- Coby AJ, Picardal F, Shelobolina E, Xu HF, Roden EE. (2011). Repeated anaerobic microbial redox cycling of iron. *Appl Environ Microb* **77**: 6036-6042.
- Deangelis KM, Silver WL, Thompson AW, Firestone MK. (2010). Microbial communities acclimate to recurring changes in soil redox potential status. *Environ Microbiol* **12**: 3137-3149.
- Deangelis KM, Firestone MK. (2012). Phylogenetic clustering of soil microbial communities by 16s rna but not 16s rna genes. *Appl Environ Microb* **78**: 2459-2461.
- Degrave E, Bowen LH, Amarasiriwardena DD, Vandenberghe RE. (1988). Fe-57 mossbauer-effect study of highly substituted aluminum hematites - determination of the magnetic hyperfine field distributions. *J. Magn. Magn. Mater.* **72**: 129-140.
- Dhakal P, Matocha CJ, Huggins FE, Vandiviere MM. (2013). Nitrite reactivity with magnetite. *Environmental Science & Technology* **47**: 6206-6213.
- Dubinsky EA, Silver WL, Firestone MK. (2010). Tropical forest soil microbial communities couple iron and carbon biogeochemistry. *Ecology* **91**: 2604-2612.
- Eyre JK, Dickson DPE. (1995). Mossbauer-spectroscopy analysis of iron-containing minerals in the chinese loess. *Journal of Geophysical Research-Solid Earth* **100**: 17925-17930.
- Fontes MR, Weed SB, Bowen LH. (1992). Association of microcrystalline goethite and humic-acid in some oxisols from brazil. *Soil Science Society of America Journal* **56**: 982-990.

- Fritsch E, Morin G, Bedidi A, Bonnin D, Balan E, Caquineau S *et al.* (2005). Transformation of haematite and al-poor goethite to al-rich goethite and associated yellowing in a ferralitic clay soil profile of the middle amazon basin (manaus, brazil). *European Journal of Soil Science* **56**: 575-588.
- Goldberg S. (1989). Interaction of aluminum and iron-oxides and clay-minerals and their effect on soil physical-properties - a review. *Communications in Soil Science and Plant Analysis* **20**: 1181-1207.
- Goodman BA, Lewis DG. (1981). Mossbauer-spectra of aluminous goethites (fe<sub>2</sub>o<sub>3</sub>). *Journal of Soil Science* **32**: 351-363.
- Hall SJ, McDowell WH, Silver WL. (2013). When wet gets wetter: Decoupling of moisture, redox biogeochemistry, and greenhouse gas fluxes in a humid tropical forest soil. *Ecosystems* **16**: 576-589.
- Hanna K. (2007). Adsorption of aromatic carboxylate compounds on the surface of synthesized iron oxide-coated sands. *Appl Geochem* **22**: 2045-2053.
- Hansel CM, Benner SG, Nico P, Fendorf S. (2004). Structural constraints of ferric (hydr)oxides on dissimilatory iron reduction and the fate of fe(ii). *Geochim Cosmochim Acta* **68**: 3217-3229.
- Hiemstra T, Mia S, Duhaut PB, Molleman B. (2013). Natural and pyrogenic humic acids at goethite and natural oxide surfaces interacting with phosphate. *Environmental Science & Technology* **47**: 9182-9189.
- Huffaker L 2002. Soil survey of caribbean national forest and luquillo experimental forest, commonwealth of puerto rico. United States Department of Agriculture.

- Hutchison KJ, Hesterberg D. (2004). Dissolution of phosphate in a phosphorus-enriched ultisol as affected by microbial reduction. *J. Environ. Qual.* **33**: 1793-1802.
- Jiskra M, Wiederhold JG, Bourdon B, Kretzschmar R. (2012). Solution speciation controls mercury isotope fractionation of hg(ii) sorption to goethite. *Environ Sci Technol* **46**: 6654-6662.
- Komlos J, Kukkadapu RK, Zachara JM, Jaffe PR. (2007). Biostimulation of iron reduction and subsequent oxidation of sediment containing fe-silicates and fe-oxides: Effect of redox cycling on fe(iii) bioreduction. *Water Res* **41**: 2996-3004.
- Kukkadapu RK, Zachara JM, Smith SC, Fredrickson JK, Liu CX. (2001). Dissimilatory bacterial reduction of al-substituted goethite in subsurface sediments. *Geochimica Et Cosmochimica Acta* **65**: 2913-2924.
- Larese-Casanova P, Kappler A, Haderlein SB. (2012). Heterogeneous oxidation of fe(ii) on iron oxides in aqueous systems: Identification and controls of fe(iii) product formation. *Geochim Cosmochim Ac* **91**: 171-186.
- Li XM, Liu TX, Li FB, Zhang W, Zhou SG, Li YT. (2012). Reduction of structural fe(iii) in oxyhydroxides by shewanella decolorationis s12 and characterization of the surface properties of iron minerals. *J. Soils Sediments* **12**: 217-227.
- Liptzin D, Silver WL. (2009). Effects of carbon additions on iron reduction and phosphorus availability in a humid tropical forest soil. *Soil Biol Biochem* **41**: 1696-1702.
- Liptzin D, Silver WL, Detto M. (2011). Temporal dynamics in soil oxygen and greenhouse gases in two humid tropical forests. *Ecosystems* **14**: 171-182.
- Loeppert RH, Inskeep WP 1996. Iron. In: SPARKS, D. L. (ed.) *Methods of soil analysis. Part 3: Chemical methods*. Madison Wisconsin: Soil Science Society of America.

- Mallet M, Barthelemy K, Ruby C, Renard A, Naille S. (2013). Investigation of phosphate adsorption onto ferrihydrite by x-ray photoelectron spectroscopy. *J. Colloid Interface Sci.* **407**: 95-101.
- Masue-Slowey Y, Loeppert RH, Fendorf S. (2011). Alteration of ferrihydrite reductive dissolution and transformation by adsorbed as and structural al: Implications for as retention. *Geochimica Et Cosmochimica Acta* **75**: 870-886.
- Mckeague JA, Day DH. (1966). Dithionite- and oxalate-extractable fe and al as aids in differentiating various classes of soils. *Canadian Journal of Soil Science* **46**: 13-&.
- Mikutta C, Mikutta R, Bonneville S, Wagner F, Voegelin A, Christl I *et al.* (2008). Synthetic coprecipitates of exopolysaccharides and ferrihydrite. Part i: Characterization. *Geochim Cosmochim Ac* **72**: 1111-1127.
- Miller AJ, Schuur EaG, Chadwick OA. (2001). Redox control of phosphorus pools in hawaiian montane forest soils. *Geoderma* **102**: 219-237.
- Minyard ML, Bruns MA, Liermann LJ, Buss HL, Brantley SL. (2012). Bacterial associations with weathering minerals at the regolith-bedrock interface, luquillo experimental forest, puerto rico. *Geomicrobiology Journal* **29**: 792-803.
- Moore DMar, R.C. 1997. *X-ray diffraction and the identification and analysis of clay minerals*, Oxford University Press.
- Murad E, Schwertmann U. (1983). The influence of aluminum substitution and crystallinity on the mossbauer-spectra of goethite. *Clay Minerals* **18**: 301-312.
- Murad E. (2010). Mossbauer spectroscopy of clays, soils and their mineral constituents. *Clay Minerals* **45**: 413-430.

- Peretyazhko T, Sposito G. (2005). Iron(III) reduction and phosphorous solubilization in humid tropical forest soils. *Geochim Cosmochim Acta* **69**: 3643-3652.
- Rancourt DG, Ping JY. (1991). Voigt-based methods for arbitrary-shape static hyperfine parameter distributions in mossbauer-spectroscopy. *Nucl. Instrum. Methods Phys. Res. Sect. B-Beam Interact. Mater. Atoms* **58**: 85-97.
- Refait P, Abdelmoula M, Trolard F, Génin J-MR, Ehrhardt JJ, Bourrié G. (2001). Mössbauer and xas study of a green rust mineral; the partial substitution of Fe<sup>2+</sup> by Mg<sup>2+</sup>. *American Mineralogist* **86**: 731-739.
- Regelink IC, Weng L, Koopmans GF, Van Riemsdijk WH. (2013). Asymmetric flow field-flow fractionation as a new approach to analyse iron-(hydr)oxide nanoparticles in soil extracts. *Geoderma* **202–203**: 134-141.
- Reyes I, Torrent J. (1997). Citrate-ascorbate as a highly selective extractant for poorly crystalline iron oxides. *Soil Sci Soc Am J* **61**: 1647-1654.
- Roden EE. (2006). Geochemical and microbiological controls on dissimilatory iron reduction. *Cr Geosci* **338**: 456-467.
- Saidy AR, Smernik RJ, Baldock JA, Kaiser K, Sanderman J. (2013). The sorption of organic carbon onto differing clay minerals in the presence and absence of hydrous iron oxide. *Geoderma* **209**: 15-21.
- Scharer M, De Grave E, Semalulu O, Sinaj S, Vandenberghe RE, Frossard E. (2009). Effect of redox conditions on phosphate exchangeability and iron forms in a soil amended with ferrous iron. *Eur J Soil Sci* **60**: 386-397.

- Schwertman U, Friedl JI, Kyek A. (2004). Formation and properties of a continuous crystallinity series of synthetic ferrihydrites (2-to 6-line) and their relation to feooh forms. *Clay Clay Min.* **52**: 221-226.
- Schwertmann U, Schulze DG, Murad E. (1982). Identification of ferrihydrite in soils by dissolution kinetics, differential x-ray-diffraction, and mossbauer-spectroscopy. *Soil Science Society of America Journal* **46**: 869-875.
- Thompson A, Rancourt DG, Chadwick OA, Chorover J. (2011). Iron solid-phase differentiation along a redox gradient in basaltic soils. *Geochim Cosmochim Acta* **75**: 119-133.
- Tufano KJ, Benner SG, Mayer KU, Marcus MA, Nico PS, Fendorf S. (2009). Aggregate-scale heterogeneity in iron (hydr)oxide reductive transformations. *Vadose Zone J* **8**: 1004-1012.
- Wang YH, Morin G, Ona-Nguema G, Menguy N, Juillot F, Aubry E *et al.* (2008). Arsenite sorption at the magnetite-water interface during aqueous precipitation of magnetite: Exafs evidence for a new arsenite surface complex. *Geochim Cosmochim Acta* **72**: 2573-2586.
- Weiss JV, Emerson D, Megonigal JP. (2004). Geochemical control of microbial fe(iii) reduction potential in wetlands: Comparison of the rhizosphere to non-rhizosphere soil. *FEMS microbiology ecology* **48**: 89-100.
- Wu T, Shelobolina E, Xu H, Konishi H, Kukkadapu R, Roden EE. (2012). Isolation and microbial reduction of fe(iii) phyllosilicates from subsurface sediments. *Environmental Science & Technology* **46**: 11618-11626.
- Zachara JM, Fredrickson JK, Li SM, Kennedy DW, Smith SC, Gassman PL. (1998). Bacterial reduction of crystalline fe<sup>3+</sup> oxides in single phase suspensions and subsurface materials. *Am Mineral* **83**: 1426-1443.

Zegeye A, Abdelmoula M, Usman M, Hanna K, Ruby C. (2011). In situ monitoring of lepidocrocite bioreduction and magnetite formation by reflection mossbauer spectroscopy. *American Mineralogist* **96**: 1410-1413.

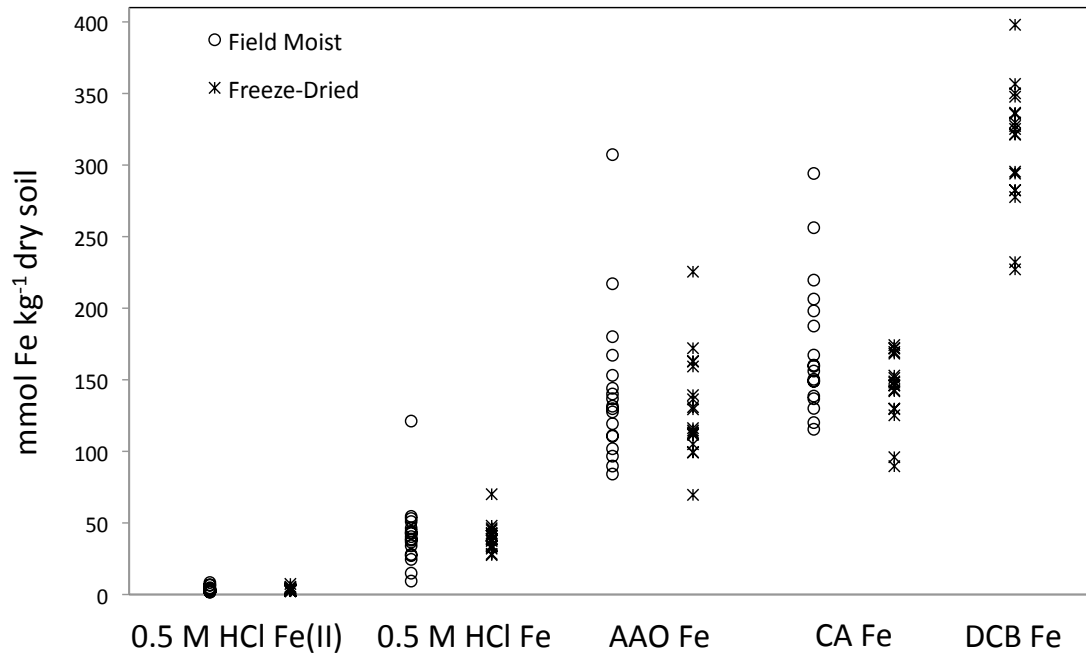


Figure 4.1. Fe extracts from field moist and freeze dried soils (n=18 field plots). Acid ammonium oxalate, citrate ascorbate and dithionite citrate bicarbonate extractable Fe is indicated as AAO Fe, CA Fe and DCB Fe respectively. Soils for dithionite extraction were only prepared as freeze-dried samples.

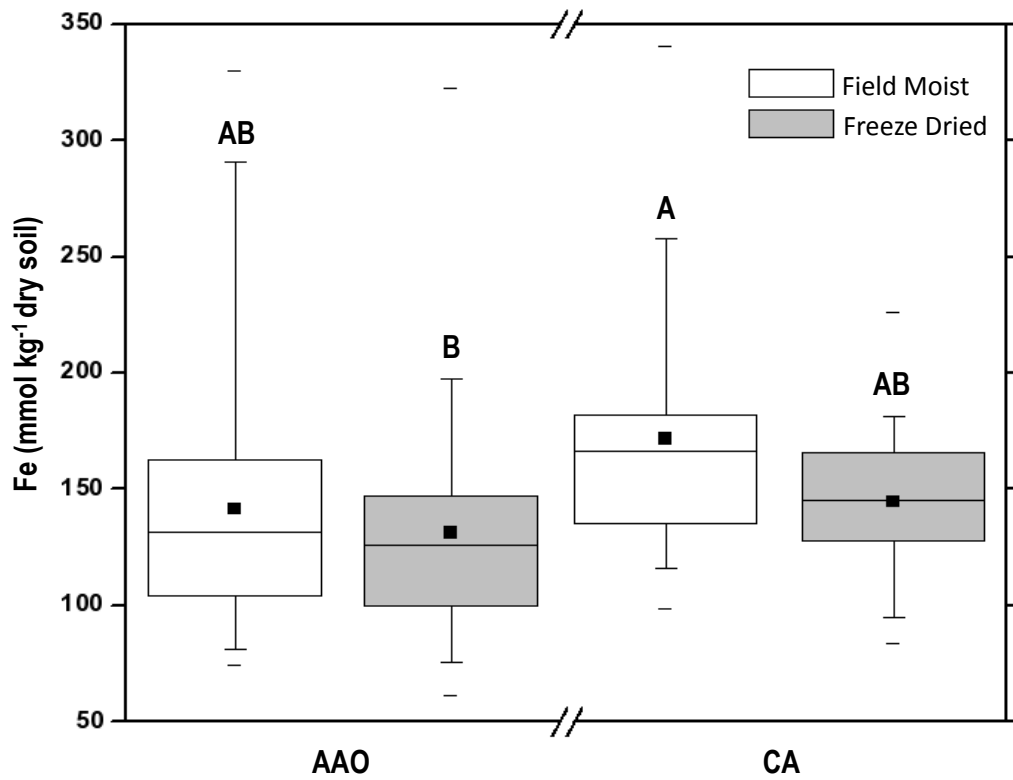


Figure 4.2. Box plots of total Fe concentrations in duplicate acid ammonium oxalate (AAO) and citrate ascorbic acid (CA) extracts from field moist and freeze dried soils (n=18 field plots). Top and bottom horizontal whisker levels range from 5 to 95% and extreme horizontal levels range from 1 to 99%. Means are indicated by black squares. Significant differences based on Tukey's HSD test ( $p < 0.01$ ) between means are indicated and connected by different letters (*A* and *B*).

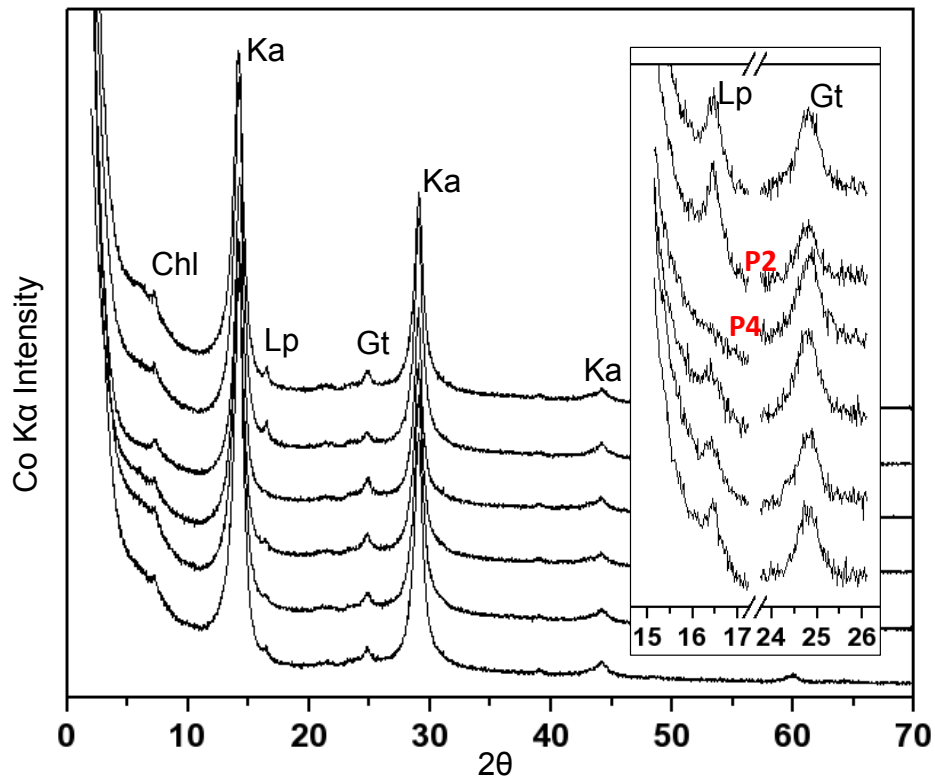


Figure 4.3. XRD was performed on the freeze-dried soils from plots 1, 2, 4, 7, 9 and 18 using a Bruker Advance diffractometer with a Co-K $\alpha$  source. Stacked XRD patterns represent in order plots 1, 2, 4, 7, 9 and 18 from top to bottom. XRD Mineral phases are indicated as follows: kaolinite (Ka); chlorite (Chl); lepidocrocite (Lp); and goethite (Gt). Inset figure panel shows magnified view of lepidocrocite and goethite reflections in  $2\theta$  space between  $15^\circ$  to  $26^\circ$ . Plot 2 (P2) shows the largest lepidocrocite proportion while P4 shows the largest goethite proportion (P2 and P4 XRD patterns are marked red). Clay suspensions were prepared by centrifugation, followed by vacuum filtration and filter-clay-transfer to glass slides, avoiding preferential sedimentation. Scan parameters included a  $0.02^\circ$  increment at  $2^\circ/\text{min}$  using a 0.6 mm slit and a  $2\theta$  interval of  $2\text{-}70^\circ$ . Data analysis was performed using the EVA software package (Bruker).

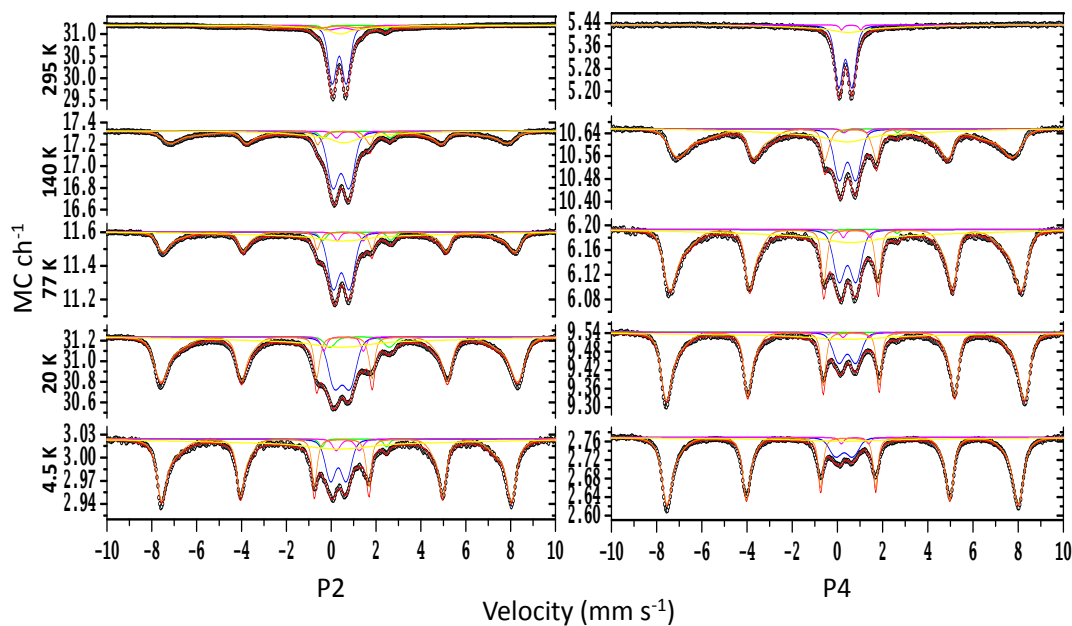


Figure 4.4.  $^{57}\text{Fe}$  Mössbauer spectra collected at 295, 140, 77, 20 and 4.5 K for freeze-dried plots P2 and P4. Raw spectral data points are shown as black open circles. Modeled Fe site populations are indicated as colored lines: Q-FeIII (blue), Q-FeII (green), Q-Fe (violet), HFD-OxHy (orange), HFD-(b)OxHy (yellow), and total fit (red). This comparison shows that the P4 sample, which contained the most goethite of all analyzed plots based on XRD, has a much more developed sextet that is attributed to the presence of goethite in the P4 MBS spectra. The P2 spectra show development of a smaller and broader sextet relative to their central doublet upon cooling to 4.5 K, which we attribute to the presence of lepidocrocite as confirmed by XRD.

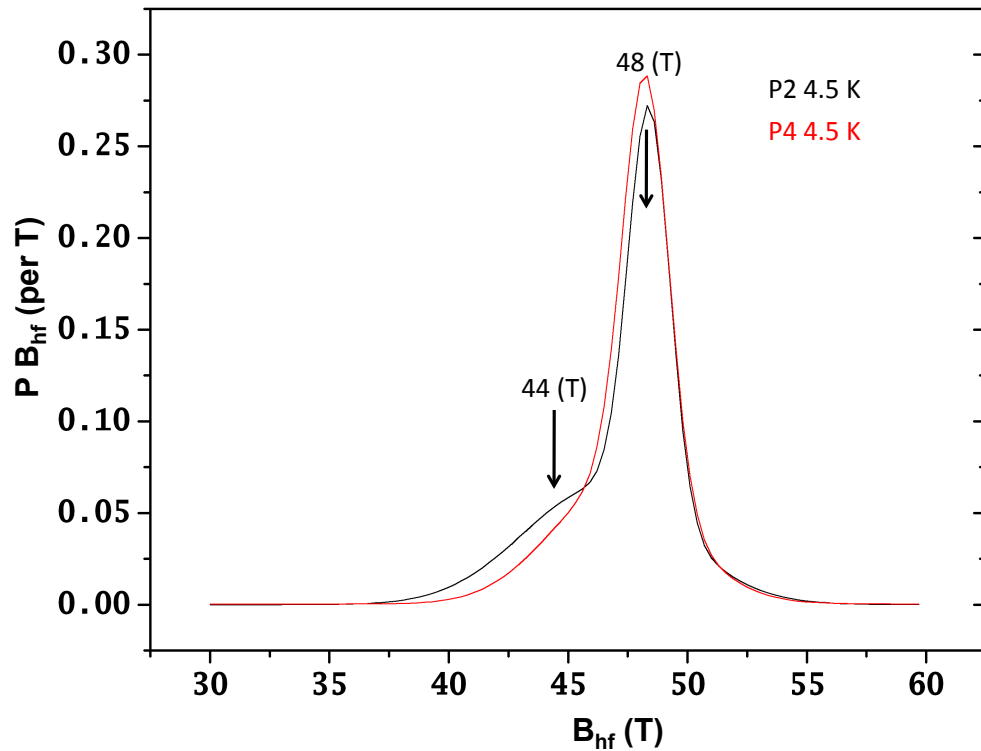


Figure 4.5. Probability density distributions of the dominant sextets (HFD-OxHy) from plot 2 and plot 4 MBS spectra collected at 4.5 K (see Appx. Figure 4.3. for complete MBS fitting). Arrows indicate the presence of distinct  $B_{hf}$  (T) peaks within the distributions. The higher  $B_{hf}$  probability of plot 2 in the 44 (T) region is attributed to the presence of lepidocrocite, and the large peak of both plot 2 and plot 4 in the 48 (T) region to the presence of goethite.

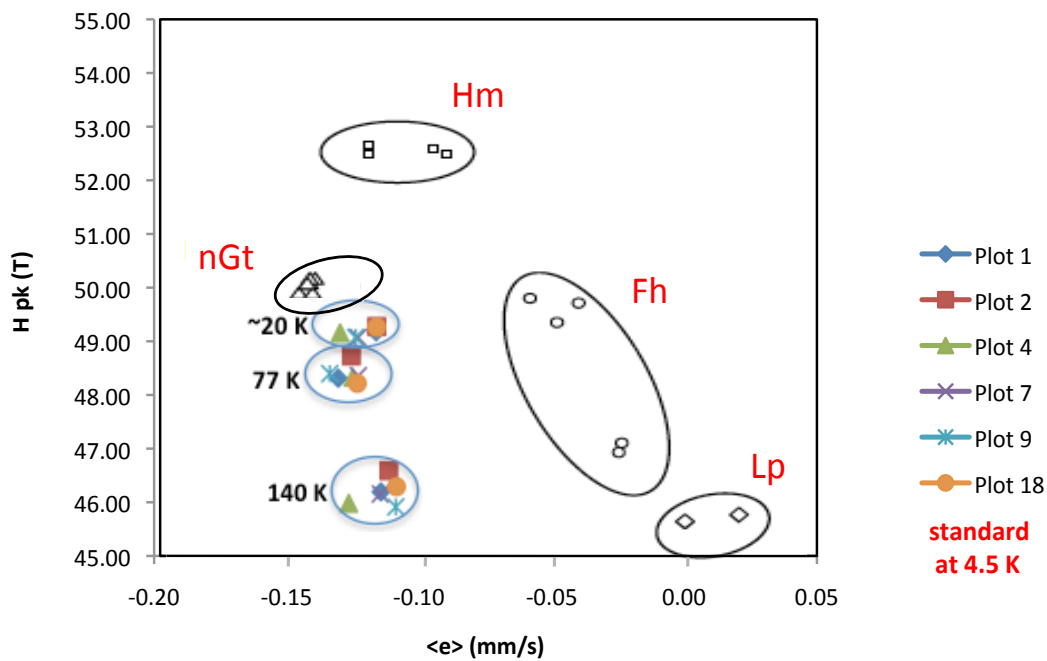


Figure 4.6. Most probable hyperfine field, H peak vs. average  $B_{hf}$  quadrupole shift,  $\langle e \rangle$ , for the HFD-OxHy sextets, primary site-component 1, of freeze-dried samples ( $n=6$ ) at 140, 77 and  $\sim 20$  K. Fe mineral standards are marked (red) that were collected near 4.5 K: nano-goethite (nGt); hematite (Hm); ferrihydrite (Fh); and lepidocrocite (Lp). The HFD-OxHy component 1 in analyzed plot samples is attributed in part to nano/highly-disordered goethite.

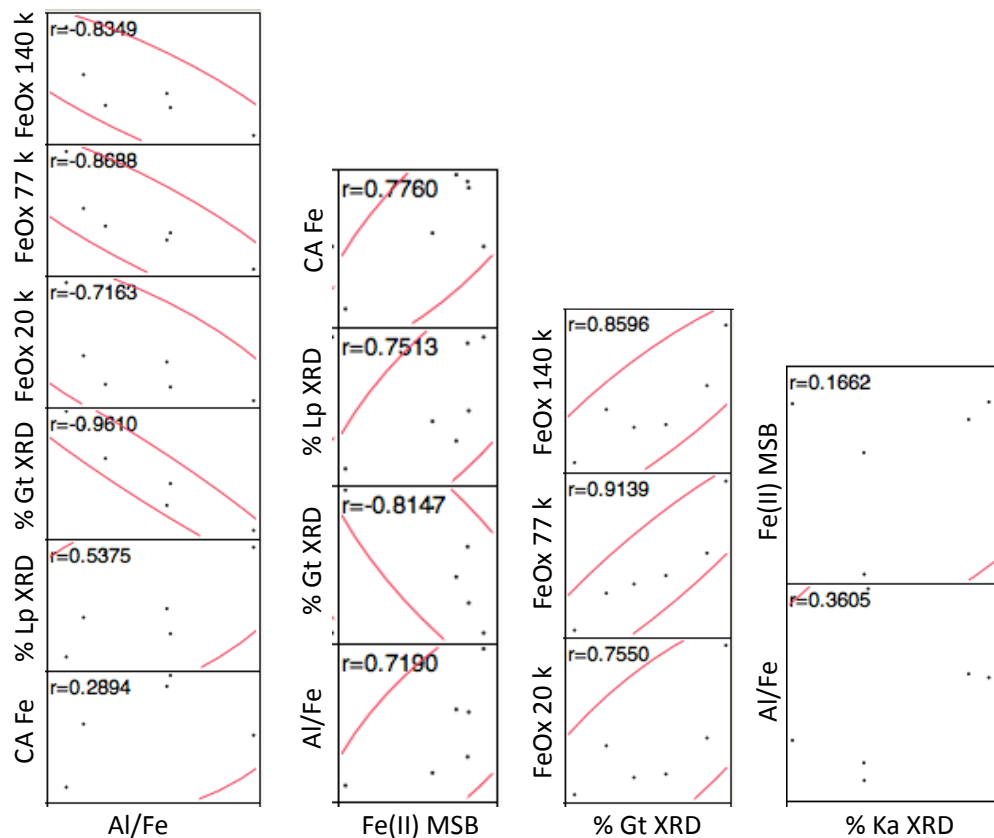


Figure 4.7. Correlation matrix for selected variables measured in this study. Al/Fe ratios were calculated from total elements analysis. Fe(II) MSB was calculated from F(II) MBS spectral proportions. MBS HFD-OxHy sextet proportions at 140, 77, and 20 K are indicated here as FeOx 140, 77 and 20 K. XRD variable include: kaolinite% (% Ka XRD); goethite% (% Gt XRD); and lepidocrocite% (% Lp XRD). Extractable Fe concentrations for the citrate ascorbate (CA) treatment are shown as CA Fe.

APPENDIX

Appx. Table 4.1. Table of total elements.

Plot ID	Analyte Conc.	Ag ppm	Ba ppm	Ce ppm	Co ppm	Cr ppm	Cs ppm	Cu ppm	Dy ppm	Er ppm	Eu ppm	Ga ppm	Gd ppm	Hf ppm	Ho ppm
1	<1		242	21.9	37.8	100	0.95	102	3.25	2.47	0.72	19.1	2.79	4.5	0.69
2	<1		194.5	18.2	40.3	90	1.03	106	2.1	1.46	0.66	20	2.25	4.5	0.44
3	<1		154.5	14.6	33.4	100	0.92	114	1.78	1.29	0.52	21.4	1.83	4.4	0.38
4	<1		154.5	12.8	35.4	130	1.02	93	1.49	1.16	0.44	23	1.48	4.5	0.32
5	<1		170	15.4	42.2	100	0.97	114	1.84	1.32	0.56	21.1	2	4.4	0.39
6	<1		193	17.3	39	100	1.06	94	2.01	1.43	0.64	21	2.16	4.6	0.43
7	<1		172.5	17.4	33	100	0.83	93	1.98	1.41	0.67	17.8	2.2	4.3	0.44
8	<1		162	19.2	33.7	110	0.84	111	1.97	1.41	0.61	21.7	2.09	4.3	0.43
9	<1		188	19.4	31.7	90	0.96	96	2.14	1.49	0.71	19.6	2.32	4.4	0.44
10	<1		182.5	19	42.3	100	0.98	92	2.06	1.44	0.67	20.5	2.24	4.6	0.43
11	<1		155.5	15.1	47	110	0.99	100	1.76	1.3	0.54	21.9	1.88	4.7	0.38
12	<1		197	20	36.7	90	0.92	108	2.21	1.54	0.73	19.2	2.42	4.3	0.46
13	<1		117	10.7	31.4	90	0.85	95	1.28	1.02	0.34	20.8	1.2	4.2	0.28
14	<1		174	16	34.5	100	1	86	1.75	1.28	0.53	19.6	1.81	4.5	0.37
15	<1		142	11.2	38.4	90	0.93	97	1.27	1.03	0.34	20.3	1.24	4.5	0.29
16	<1		161	12.5	36.8	120	0.88	103	1.25	1.02	0.35	21	1.27	4.4	0.28
17	<1		179	12.6	35.1	90	0.97	101	1.3	1.05	0.39	20.2	1.3	4.4	0.3
18	<1		186.5	18.2	37.4	90	0.99	85	2.01	1.42	0.66	20.1	2.14	4.4	0.43

Plot ID	Analyte Amount	La ppm	Lu ppm	Mo ppm	Nb ppm	Nd ppm	Ni ppm	Pb ppm	Pr ppm	Rb ppm	Sm ppm	Sn ppm	Sr ppm	Ta ppm	Tb ppm
1		9.5	0.55	2	2.9	12.5	30	11	2.84	7.7	2.98	1	71.2	0.2	0.46
2		9.1	0.29	<2	3.1	10.4	34	11	2.43	7	2.45	1	63.7	0.2	0.33
3		7.9	0.27	<2	3	8.4	39	10	2	5.7	1.93	1	28.6	0.2	0.27
4		7.3	0.27	2	3.3	6.9	44	11	1.71	6.4	1.55	1	27.6	0.2	0.23
5		8.6	0.29	<2	2.9	8.9	38	10	2.14	5.4	2.07	1	32.7	0.2	0.3
6		9	0.29	<2	3.2	9.9	40	9	2.34	6.5	2.23	1	59.2	0.2	0.32
7		8.3	0.26	<2	3.1	9.4	30	8	2.2	5.8	2.23	1	73	0.2	0.32
8		7.8	0.28	<2	3	8.9	30	11	2.12	5.7	2.13	1	30.9	0.2	0.32
9		8.6	0.29	<2	3.2	10.1	29	10	2.38	6.6	2.37	1	55.9	0.2	0.34
10		9.2	0.29	<2	3	9.9	34	11	2.35	5.5	2.26	1	53	0.2	0.33
11		8.8	0.28	<2	3.1	8.6	42	9	2.14	5.2	1.91	1	31	0.2	0.28
12		8.9	0.29	<2	2.9	10.5	33	20	2.49	6.9	2.49	1	62.4	0.2	0.36
13		5.5	0.24	<2	3.3	5.4	30	12	1.31	5.1	1.21	1	20.4	0.2	0.19
14		7.8	0.27	<2	3.3	8.3	27	11	1.97	6.8	1.91	1	47.5	0.2	0.27
15		6	0.23	<2	3.3	5.7	30	12	1.41	5.7	1.27	1	31.9	0.2	0.19
16		6.5	0.24	<2	3.5	5.9	31	11	1.52	6.5	1.31	1	33.5	0.2	0.2
17		7.7	0.24	<2	3.3	6.6	31	10	1.75	7.6	1.41	1	31.6	0.2	0.2
18		9	0.27	<2	2.9	10	29	11	2.38	6.1	2.32	1	56.6	0.2	0.32

Plot ID	Analyte Amount	Th ppm	Tl ppm	Tm ppm	U ppm	V ppm	W ppm	Y ppm	Yb ppm	Zn ppm	Zr ppm	SiO2 %	Al2O3 %	Fe2O3 %	CaO %
1		2.69	<0.5	0.47	1.15	331	<1	36.2	3.47	161	168	60.1	14.8	8.57	0.74
2		2.43	<0.5	0.24	1.09	320	<1	13.9	1.72	78	167	58.2	15.45	7.68	0.68

3	2.46	<0.5	0.22	1.06	328	<1	11.2	1.55	102	163	50.6	17.15	10.4	0.26
4	2.75	<0.5	0.19	1.08	353	<1	9	1.5	97	168	48.1	18.25	11.05	0.25
5	2.44	<0.5	0.22	1.07	331	<1	11.2	1.62	79	164	50.3	17.65	10.3	0.34
6	2.48	<0.5	0.24	1.19	334	<1	12.3	1.66	78	175	57.8	16.15	8.65	0.58
7	2.27	<0.5	0.23	1.06	349	1	12.1	1.58	64	161	61	13.95	8.28	0.83
8	2.43	<0.5	0.22	1.06	362	1	12	1.62	70	161	52.5	17.3	10.75	0.32
9	2.43	<0.5	0.25	1.08	336	1	12.6	1.63	68	167	58.2	15.5	8.37	0.62
10	2.53	<0.5	0.24	1.12	352	<1	12	1.68	74	167	56.7	16.1	9.58	0.47
11	2.55	<0.5	0.21	1.13	352	<1	10.3	1.55	76	170	53.2	17.75	11	0.25
12	2.31	<0.5	0.24	1.05	341	<1	13.1	1.64	71	161	58.1	14.95	8.33	0.7
13	2.47	<0.5	0.17	1.03	355	<1	8	1.27	63	159	48.3	17.9	10.6	0.24
14	2.44	<0.5	0.21	1.09	361	1	10.6	1.49	76	170	55.9	15.55	8.86	0.54
15	2.48	<0.5	0.17	1.06	367	<1	8.3	1.35	71	168	52.7	16.3	10.8	0.34
16	2.53	<0.5	0.18	1.07	363	<1	8.2	1.32	61	164	53.4	16.85	10.85	0.34
17	2.49	<0.5	0.18	1.07	330	<1	8.3	1.35	72	164	53.2	15.95	9.3	0.32
18	2.38	<0.5	0.23	1.04	343	<1	11.8	1.57	77	162	57.4	15.7	8.51	0.61
Plot ID	Analyte Amount	MgO %	Na2O %	K2O %	Cr2O3 %	TiO2 %	MnO %	P2O5 %	SrO %	BaO %	LOI %	Total %		
1		0.62	0.35	0.33	0.01	0.92	0.12	0.1	0.01	0.03	15.25	102		
2		0.57	0.24	0.25	0.01	0.93	0.12	0.07	0.01	0.02	16.25	100.5		
3		0.47	0.09	0.17	0.01	0.89	0.09	0.11	<0.01	0.02	18.5	98.8		
4		0.4	0.11	0.18	0.02	0.93	0.11	0.08	<0.01	0.02	19.75	99.3		
5		0.51	0.17	0.18	0.01	0.91	0.11	0.08	0.01	0.02	18.5	99.1		
6		0.56	0.22	0.23	0.01	0.95	0.11	0.07	0.01	0.02	16.6	102		
7		0.56	0.37	0.33	0.01	0.86	0.11	0.1	<0.01	0.02	NSS	NSS		
8		0.57	0.18	0.22	0.01	0.96	0.11	0.08	<0.01	0.02	16.7	99.7		
9		0.58	0.3	0.27	0.01	0.95	0.13	0.06	0.01	0.02	14.35	99.4		
10		0.46	0.18	0.2	0.01	0.91	0.16	0.06	0.01	0.02	14.8	99.7		
11		0.4	0.1	0.16	0.01	0.92	0.16	0.07	<0.01	0.02	16.4	100.5		
12		0.6	0.33	0.28	0.01	0.89	0.15	0.06	0.01	0.02	13.75	98.2		
13		0.48	0.18	0.17	0.01	0.94	0.07	0.12	0.01	0.01	19.5	98.5		
14		0.47	0.25	0.25	0.01	0.97	0.15	0.07	0.01	0.02	16.4	99.5		
15		0.46	0.17	0.2	0.01	0.97	0.13	0.07	<0.01	0.02	18.2	100.5		
16		0.51	0.17	0.25	0.02	0.97	0.13	0.07	<0.01	0.02	17.05	100.5		
17		0.45	0.19	0.29	0.01	0.95	0.1	0.08	<0.01	0.02	18.85	99.7		
18		0.58	0.26	0.24	0.01	0.93	0.17	0.05	0.01	0.02	NSS	NSS		

Appx. Table 4.2. MBS details for plot 2 and 4 at 295, 140, 77, ~20 and 4.5 K.

Appx. Table 4.2.: Mössbauer parameters (see Figure 4.4.)

Sample	Temp K	Phase	Spectral Area		$\delta_0$ mm/s	$\epsilon_0$ mm/s	P %	$\Delta$ or H mm/s or T	$\sigma$ mm/s or T	Red- $X^2$	<CS> mm/s	< $\epsilon$ > mm/s	<QS> or <H> mm/s or T	s.d. mm/s or T
			MC*mm/s	%										
Plot 2 (2Q, 2H)  (BG = 31.2 MC/ch)	295	Q-Fe <sup>III</sup>	1.415	53.3(1)	0.36	n/a	100*	0.626	0.272	8.088	0.36	n/a	0.628	0.267
		Q-Fe <sup>II</sup>	0.08	3(1)	1.077	n/a	100*	2.758	0.136		1.08	n/a	2.76	0.136
		Q-Fe?	0.217(4)	8.18(15)	0.509(13)	n/a	100*	1.272(21)	0.700(23)		0.51	n/a	1.29	0.664
		HFD-OxHy	0.486	18.30(3)	0.455	0.08	0*	38.14	2.119		0.46	0.08	30.38	11.38
		HFD-(b)OxHy	0.458	17.23(3)	0.404	0*	100*	0*	10.58		0.4	0	(Peak H 30.32 T)	8.44
Plot 2 (2Q, 2H)  (BG = 17.32 MC/ch)	140	Q-Fe <sup>III</sup>	0.724(13)	37.6(6)	0.438(4)	n/a	100*	0.707(4)	0.413(8)	1.928	0.438	n/a	0.722	0.387
		Q-Fe <sup>II</sup>	0.065(4)	3.40(22)	1.147(13)	n/a	100*	2.98(2)	0.254(29)		1.147	n/a	2.98	0.254
		Q-Fe?	0.057(7)	2.97(35)	0.78(1)	n/a	100*	1.095(37)	0.185(33)		0.78	n/a	1.095	0.185
		HFD-OxHy	0.728(14)	37.9(6)	0.455(5)	-0.110(5)	43.35*	46.65(7)	1.90(11)		0.455	-0.110	44.036	4.917
		HFD-(b)OxHy	0.350(13)	18.2(6)	0.571(33)	0*	100*	0*	15.4(12)		0.571	0	(Peak H 46.47 T)	12.285
Plot 2 (2Q, 2H)  (BG = 11.6 MC/ch)	77	Q-Fe <sup>III</sup>	0.463(6)	33(1)	0.451(3)	n/a	100*	0.709(4)	0.404(7)	2.613	0.451	n/a	0.722	0.38
		Q-Fe <sup>II</sup>	0.048(3)	3.40(22)	1.140(11)	n/a	100*	3.036(22)	0.213(28)		1.14	n/a	3.036	0.213
		Q-Fe?	0.043(4)	3.05(26)	0.852(11)	n/a	100*	1.166(25)	0.149(30)		0.852	n/a	1.166	0.149
		HFD-OxHy	0.499*	35.5(6)	0.475(3)	-0.123(3)	54.18*	48.67(5)	1.30(8)		0.475	-0.123	47.26	2.886
		HFD-(b)OxHy	0.351(15)	25.0(8)	0.536(60)	0*	100*	0*	32.9(22)		0.536	0	(Peak H 48.57 T)	26.27
Plot 2 (2Q, 3H)  (BG = 31.24 MC/ch)	20	Q-Fe <sup>III</sup>	0.765(9)	19.9(3)	0.489(4)	n/a	100*	0.682	0.490(12)	15.927	0.488	n/a	0.719	0.434
		Q-Fe <sup>II</sup>	0.146(7)	3.78(17)	1.266(13)	n/a	100*	2.656(25)	0.396(27)		1.266	n/a	2.656	0.396
		Q-Fe?	0.115(8)	2.99(20)	0.552(6)	n/a	100*	1.768(13)	0.145(19)		0.552	n/a	1.768	0.145
		HFD-OxHy	2.012(18)	52.3(5)	0.476(2)	-0.113(2)	51.2*	49.36(2)	1.436(34)		0.476	-0.113	47.96	3.287
		HFD-(b)OxHy	0.814(28)	21.1(6)	0.455*	0*	100*	0*	40.4(19)		0.455	0	(Peak H 49.27 T)	32.22
Plot 2 (2Q, 3H)  (BG = 3.024 MC/ch)	4.5	Q-Fe <sup>III</sup>	0.072(3)	14.4(12)	0.318(9)	n/a	100*	0.694(12)	0.378(19)	2.762	0.318	n/a	0.704	0.36
		Q-Fe <sup>II</sup>	0.008(2)	1.68(32)	1.025(21)	n/a	100*	2.884(43)	0.141(65)		1.025	n/a	2.88	0.141
		Q-Fe?	0.016(2)	3.19(50)	0.745(20)	n/a	100*	1.024(40)	0.253(52)		0.745	n/a	1.02	0.253
		HFD-OxHy	0.283(4)	56.6(43)	0.354(2)	-0.113(2)	47.9*	48.38(3)	0.869(43)		0.354	-0.113	47.33	2.636
		HFD-(b)OxHy	0.121(38)	24.2(57)	0.35*	0*	100*	0*	46(15)		0.35	0	(Peak H 48.35 T)	37.08

Appx. Table 4.2.: Mössbauer parameters (see Figure 4.4.)

Sample	Temp K	Phase	Spectral Area		$\delta_0$ mm/s	$\epsilon_0$ mm/s	P %	$\Delta$ or H mm/s or T	$\sigma$ mm/s or T	Red- $X^2$	<CS> mm/s	< $\epsilon$ > mm/s	<QS> or <H> mm/s or T	s.d. mm/s or T
			MC*mm/s	%										
Plot 4 (2Q, 2H)  (BG = 5.435 MC/ch)	295	Q-Fe <sup>III</sup>	0.226(3)	64.6(14)	0.355(2)	n/a	100*	0.586(3)	0.252(6)	1.357	0.355	n/a	0.588	0.248
		Q-Fe <sup>II</sup>	n/a	n/a	n/a	n/a	n/a	n/a	n/a	n/a	n/a	n/a	n/a	n/a
		Q-Fe?	0.011(2)	3.13(61)	0.608(16)	n/a	100*	0.850(36)	0.0(14)	n/a	0.608	n/a	0.85	0.003
		HFD-OxHy	n/a	n/a	n/a	n/a	n/a	n/a	n/a	n/a	n/a	n/a	n/a	n/a
		HFD-(b)OxHy	0.113(7)	32.2(14)	0.48*	0*	100*	0*	20.3(21)		0.48	0	(Peak H n/a) 16.23	12.26
Plot 4 (2Q, 2H)  (BG = 10.66 MC/ch)	140	Q-Fe <sup>III</sup>	0.240(5)	20.5(6)	0.446(5)	n/a	100*	0.723(7)	0.39(1)	2.301	0.446	n/a	0.732	0.367
		Q-Fe <sup>II</sup>	0.010(2)	0.81(20)	1.441(31)	n/a	100*	2.437(62)	0.08(11)	n/a	1.44	n/a	2.437	0.077
		Q-Fe?	0.011(3)	0.93(29)	0.810(35)	n/a	100*	1.010(68)	0.14(11)	n/a	0.81	n/a	1.01	0.14
		HFD-OxHy	0.655(19)	56.1(13)	0.461(4)	-0.126(4)	48.71*	46.09(6)	2.05(12)	4.83(40)	0.461	-0.126	43.32	4.61
		HFD-(b)OxHy	0.252(21)	21.6(15)	0.426(72)	0*	100*	0*	27.0(34)		0.426	0	(Peak H 45.85 T) 21.54	16.27
Plot 4 (2Q, 2H)  (BG = 6.193 MC/ch)	77	Q-Fe <sup>III</sup>	0.118(4)	16.3(5)	0.447(8)	n/a	100*	0.736(11)	0.409(18)	2.464	0.447	n/a	0.748	0.387
		Q-Fe <sup>II</sup>	0.005(2)	0.68(24)	1.159(34)	n/a	100*	2.967(68)	0(46)	n/a	1.159	n/a	2.967	0.153
		Q-Fe?	0.010(2)	1.36(32)	0.851(26)	n/a	100*	1.183(57)	0.105(86)	n/a	0.851	n/a	1.183	0.105
		HFD-OxHy	0.425(7)	58.7(10)	0.482(3)	-0.123(3)	56.04*	48.28(4)	1.361(89)	3.14(30)	0.482	-0.123	46.77	2.876
		HFD-(b)OxHy	0.166(11)	23.0(12)	0.59(11)	0*	100*	0*	39.9(37)		0.595	0	(Peak H 48.15 T) 31.8	24.02
Plot 4 (2Q, 3H)  (BG = 9.542 MC/ch)	22	Q-Fe <sup>III</sup>	0.143(4)	12.0(4)	0.437(9)	n/a	100*	0.746(12)	0.427(20)	5.538	0.437	n/a	0.76	0.402
		Q-Fe <sup>II</sup>	0.004(2)	0.35(18)	1.109(51)	n/a	100*	3.00(10)	0.03(49)	n/a	1.109	n/a	2.996	0.027
		Q-Fe?	0.013(3)	1.08(25)	0.836(26)	n/a	100*	1.177(59)	0.116(83)	n/a	0.836	n/a	1.177	0.116
		HFD-OxHy	0.775(7)	65.0(8)	0.483(15)	-0.128(2)	55.87*	49.19(2)	1.058(36)	2.947(91)	0.483	-0.128	48.25	2.363
		HFD-(b)OxHy	0.256(14)	21.5(9)	0.51(15)	0*	100*	0*	57.7(52)		0.506	0	(Peak H 49.14 T) 46	34.75
Plot 4 (2Q, 3H)  (BG = 2.769 MC/ch)	4.5	Q-FelII	0.063(3)	10.1(7)	0.30(1)	n/a	100*	0.748(14)	0.468(23)	9.008	0.296	n/a	0.769	0.431
		Q-FelI	n/a	n/a	n/a	n/a	n/a	n/a	n/a	n/a	n/a	n/a	n/a	n/a
		Q-Fe?	0.010(1)	1.63(24)	0.774(14)	n/a	100*	1.207(30)	0.100(50)	n/a	0.774	n/a	1.207	0.1
		HFD-OxHy	0.469(4)	74.8(44)	0.354(1)	-0.120(1)	55.4*	48.24(2)	0.958(29)	2.769(88)	0.354	-0.120	47.696	2.072
		HFD-(b)OxHy	0.084(36)	13.4(50)	0.35*	0*	100*	0*	51(23)		0.35	0	(Peak H 48.2 T) 40.299	30.45

Appx. Table 4.3. Average 295 (room temperature K or RTK), 140, 77, ~20 and 4.5 K key Mössbauer parameters for plot 1, 2, 4, 7, 9 and 18. Quadrupole and magnetic hyperfine distributions (QSD and HFD site values) have been split into two columns left and right respectively. Voight-based fitting (VBF) sites are as follows: For QSD column, VBF Site 1 (Q-FeIII); VBF Site 2 (Q-FeII); VBF Site 3 (Q-Fe); and for HFD column, VBF Site 1 (HFD-OxHy); VBF Site 2 (HFD-(b)OxHy).

VBF Site 1	QSD Sites							VBF Site 1	HFD Sites						
	QSD-RTK	P1	P2	P4	P7	P9	P18		HFD-RTK	P1	P2	P4	P7	P9	P18
	<CS>	0.37	0.36	0.36	0.36	0.36	0.36		<CS>	0.00	0.46	0.00	0.46	0.00	0.00
	<delta>	0.63	0.63	0.59	0.63	0.61	0.63		<e>	0.00	0.08	0.00	0.08	0.00	0.00
	stdev<delta>	0.25	0.27	0.25	0.27	0.27	0.31		<H>	0.00	30.38	0.00	30.38	0.00	0.00
	%	57.30	53.30	65.88	53.18	59.56	62.00		<H>peak	0.00	30.30	0.00	30.34	0.00	0.00
									stdev<H>	0.00	11.38	0.00	11.38	0.00	0.00
									%	0.00	18.30	0.00	14.65	0.00	0.00
VBF Site 1	QSD-140K	P1	P2	P4	P7	P9	P18	VBF Site 1	HFD-140K	P1	P2	P4	P7	P9	P18
	<CS>	0.44	0.44	0.45	0.43	0.44	0.43		<CS>	0.45	0.46	0.46	0.46	0.46	0.44
	<delta>	0.75	0.72	0.73	0.73	0.71	0.73		<e>	-0.11	-0.11	-0.13	-0.11	-0.11	-0.11
	stdev<delta>	0.44	0.39	0.37	0.37	0.34	0.39		<H>	43.66	44.04	43.32	43.59	43.19	44.09
	%	32.28	37.60	20.54	26.41	32.00	28.70		<H>peak	46.07	46.48	45.85	46.03	45.78	46.17
									stdev<H>	5.22	4.92	4.61	4.88	5.05	4.31

								%	41.51	37.85	56.10	46.74	41.70	33.50
<b>QSD-77K</b>	<b>P1</b>	<b>P2</b>	<b>P4</b>	<b>P7</b>	<b>P9</b>	<b>P18</b>		<b>HFD-77K</b>	<b>P1</b>	<b>P2</b>	<b>P4</b>	<b>P7</b>	<b>P9</b>	<b>P18</b>
<CS>	0.41	0.45	0.45	0.43	0.47	0.45		<CS>	0.49	0.47	0.48	0.47	0.48	0.48
<delta>	0.80	0.72	0.75	0.75	0.69	0.74		<e>	-0.13	-0.12	-0.12	-0.12	-0.13	-0.12
stdev<delta>	0.47	0.38	0.39	0.41	0.33	0.36		<H>	46.68	47.26	46.77	46.79	46.47	46.46
%	25.30	32.99	16.26	23.16	23.90	24.20		<H>peak	48.14	48.58	48.16	48.19	48.23	48.04
								stdev<H>	3.89	2.89	2.88	3.26	3.72	3.77
								%	37.80	35.54	58.70	47.49	45.90	46.30
<b>QSD--20K</b>	<b>P1</b>	<b>P2</b>	<b>P4</b>	<b>P7</b>	<b>P9</b>	<b>P18</b>		<b>HFD--20K</b>	<b>P1</b>	<b>P2</b>	<b>P4</b>	<b>P7</b>	<b>P9</b>	<b>P18</b>
<CS>	0.46	0.49	0.44	0.42	0.44	0.43		<CS>	0.48	0.48	0.48	0.48	0.48	0.48
<delta>	0.79	0.72	0.76	0.78	0.73	0.74		<e>	-0.11	-0.11	-0.13	-0.12	-0.12	-0.11
stdev<delta>	0.43	0.43	0.40	0.40	0.39	0.39		<H>	48.19	47.96	48.25	48.01	48.37	48.29
%	17.21	19.86	12.01	15.32	18.98	14.95		<H>peak	49.16	49.26	49.14	49.05	49.29	49.25
								stdev<H>	3.23	3.29	2.36	2.92	2.43	2.76
								%	55.50	52.25	65.04	55.29	57.50	56.20
<b>QSD-4.5K</b>	<b>P1</b>	<b>P2</b>	<b>P4</b>	<b>P7</b>	<b>P9</b>	<b>P18</b>		<b>HFD-4.5K</b>	<b>P1</b>	<b>P2</b>	<b>P4</b>	<b>P7</b>	<b>P9</b>	<b>P18</b>
<CS>	n/a	0.32	0.3	n/a	n/a	n/a		<CS>	n/a	0.35	0.35	n/a	n/a	n/a

		<delta>	n/a	0.7	0.77	n/a	n/a	n/a			<e>	n/a	-0.11	-0.12	n/a	n/a	n/a
		stdev<delta>	n/a	0.36	0.43	n/a	n/a	n/a			<H>	n/a	47.33	47.7	n/a	n/a	n/a
		%	n/a	14.4	10.12	n/a	n/a	n/a			<H>peak	n/a	48.35	48.2	n/a	n/a	n/a
											stdev<H>	n/a	2.64	2.07	n/a	n/a	n/a
											%	n/a	56.6	74.8	n/a	n/a	n/a
<b>VBF Site 2</b>	<b>QSD-RTK</b>	<b>P1</b>	<b>P2</b>	<b>P4</b>	<b>P7</b>	<b>P9</b>	<b>P18</b>		<b>VBF Site 2</b>	<b>HFD-RTK</b>	<b>P1</b>	<b>P2</b>	<b>P4</b>	<b>P7</b>	<b>P9</b>	<b>P18</b>	
	<CS>	1.07	1.08	0.00	1.08	1.03	0.98			<CS>	0.36	0.40	0.39	0.40	0.46	0.41	
	<delta>	2.75	2.76	0.00	2.76	2.75	2.80			<e>	0.00	0.00	0.00	0.00	0.00	0.00	
	stdev<delta>	0.21	0.14	0.00	0.14	0.21	0.27			<H>	7.47	8.44	14.63	8.44	19.20	14.27	
	%	4.25	3.00	0.00	2.38	2.55	3.64			stdev<H>	5.64	6.38	11.05	6.38	14.51	10.78	
	high-line pos	1.91	1.92	0.00	1.92	1.89	1.89			%	38.40	17.23	34.12	24.97	37.89	34.40	
	<b>QSD-140K</b>	<b>P1</b>	<b>P2</b>	<b>P4</b>	<b>P7</b>	<b>P9</b>	<b>P18</b>			<b>HFD-140K</b>	<b>P1</b>	<b>P2</b>	<b>P4</b>	<b>P7</b>	<b>P9</b>	<b>P18</b>	
	<CS>	1.18	1.15	1.44	1.15	1.17	1.15			<CS>	0.59	0.57	0.43	0.58	0.52	0.25	
	<delta>	2.91	2.98	2.44	2.96	2.91	2.93			<e>	0.00	0.00	0.00	0.00	0.00	0.00	
	stdev<delta>	0.33	0.25	0.08	0.23	0.21	0.23			<H>	13.51	12.28	21.54	15.05	11.70	28.57	
	%	3.26	3.40	0.81	2.79	3.83	2.94			stdev<H>	10.21	9.28	16.27	11.37	8.84	21.59	
	high-line pos	2.04	2.06	1.94	2.06	2.04	2.04			%	20.53	18.19	21.60	21.42	19.90	30.90	

QSD-77K							HFD-77K						
	P1	P2	P4	P7	P9	P18		P1	P2	P4	P7	P9	P18
<CS>	1.15	1.14	1.16	1.15	1.23	1.18	<CS>	0.84	0.54	0.59	0.66	0.27	0.51
<delta>	3.01	3.04	2.97	3.01	2.94	2.98	<e>	0.00	0.00	0.00	0.00	0.00	0.00
stdev<delta>	0.35	0.21	0.15	0.19	0.23	0.17	<H>	42.91	26.27	31.80	25.13	23.79	21.90
%	2.29	3.40	0.68	2.66	4.05	3.66	stdev<H>	32.42	19.85	24.02	18.99	17.97	16.55
high-line pos	2.08	2.09	2.06	2.08	2.08	2.08	%	30.50	25.01	23.00	24.00	21.20	19.50
QSD--20K							HFD--20K						
	P1	P2	P4	P7	P9	P18		P1	P2	P4	P7	P9	P18
<CS>	1.13	1.27	1.11	1.16	1.16	1.15	<CS>	0.13	0.46	0.51	0.47	0.47	0.47
<delta>	2.79	2.66	3.00	2.98	2.97	2.86	<e>	0.00	0.00	0.00	0.00	0.00	0.00
stdev<delta>	0.29	0.40	0.03	0.18	0.19	0.24	<H>	34.69	32.22	46.00	31.22	34.44	35.45
%	3.38	3.78	0.35	2.51	3.10	3.41	stdev<H>	26.21	24.34	34.75	23.58	26.02	26.79
high-line pos	1.96	1.96	2.05	2.07	2.06	2.00	%	19.70	21.13	21.52	23.10	17.40	21.50
QSD-4.5K							HFD-4.5K						
	P1	P2	P4	P7	P9	P18		P1	P2	P4	P7	P9	P18
<CS>	n/a	1.03	n/a	n/a	n/a	n/a	<CS>	n/a	0.35	0.35	n/a	n/a	n/a



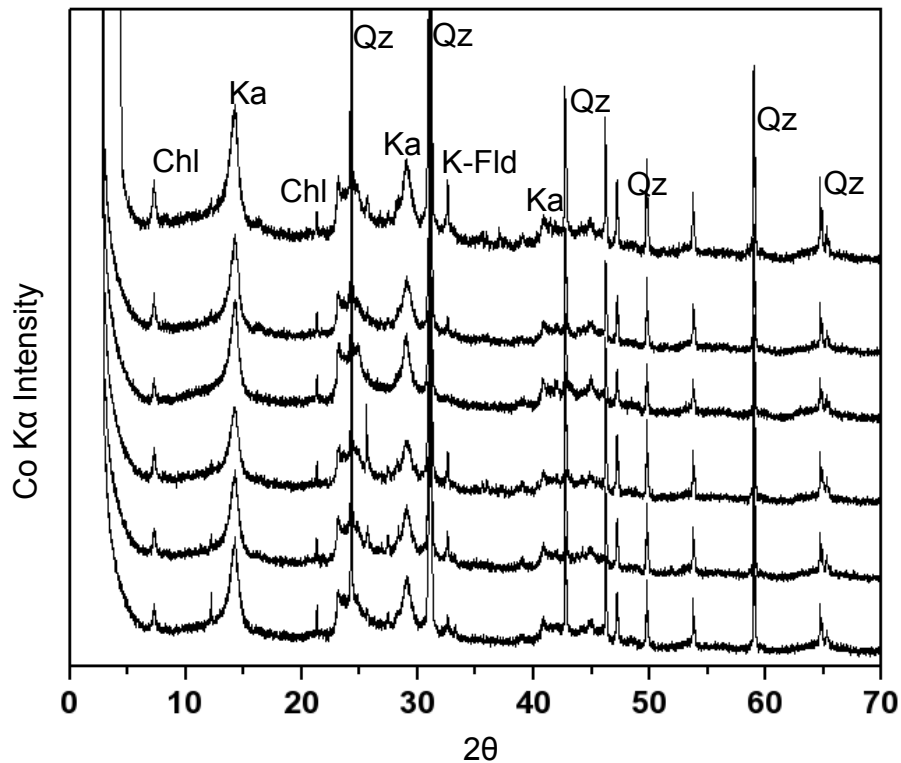
QSD-77K	P1	P2	P4	P7	P9	P18
<CS>	0.86	0.85	0.85	0.85	0.89	0.90
<delta>	1.05	1.17	1.18	1.18	0.92	0.93
stdev<delta>	0.24	0.15	0.11	0.14	0.35	0.32
%	4.10	3.05	1.36	2.73	4.90	6.30
QSD--20K	P1	P2	P4	P7	P9	P18
<CS>	0.90	0.55	0.84	0.88	0.88	0.85
<delta>	0.99	1.77	1.18	1.08	1.20	1.03
stdev<delta>	0.24	0.14	0.12	0.25	0.14	0.25
%	4.13	2.99	1.08	3.79	2.95	3.89
QSD-4.5K	P1	P2	P4	P7	P9	P18
<CS>	n/a	0.74	0.77	n/a	n/a	n/a
<delta>	n/a	1.02	1.21	n/a	n/a	n/a

<b>stdev&lt;delta&gt;</b>	n/a	<b>0.25</b>	<b>0.1</b>	n/a	n/a	n/a		
<b>%</b>	n/a	<b>3.19</b>	<b>1.63</b>	n/a	n/a	n/a		

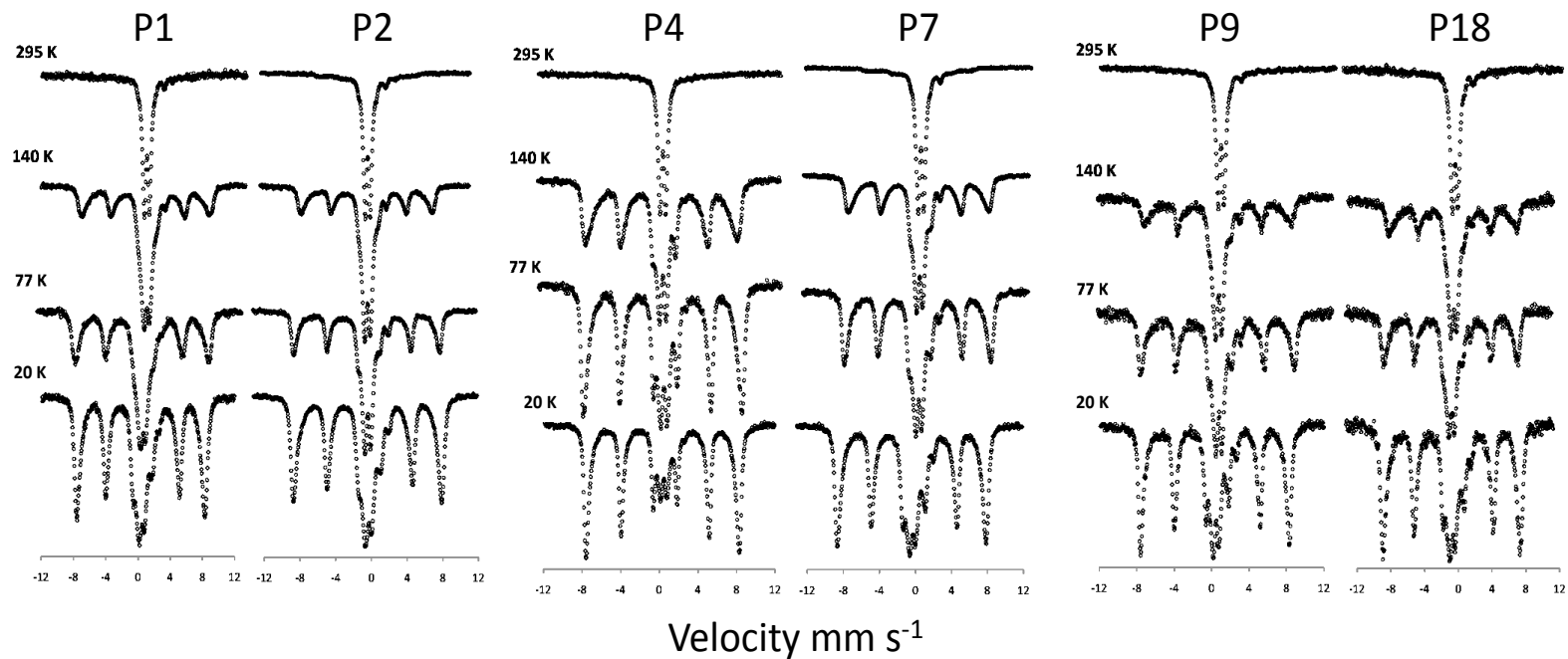
Appx. Table 4.4. Correlation matrix statistics for selected variables measured in this study (see Fig. 4.7).

Correlations Between XRD, MSB & Extractable Fe

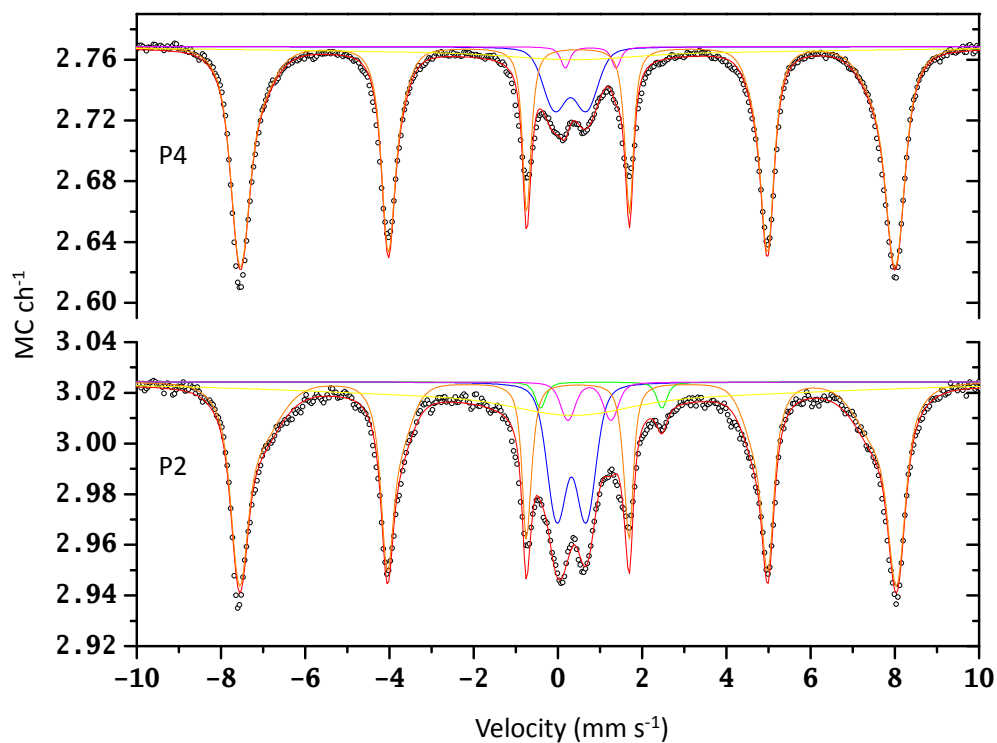
Variable	by Variable	Correlation (r)	Lower 95%	Upper 95%	Lower 90%	Upper 90%
XRD Gt/(Gt+Lp)	MSB Sextet 140K	0.8516	0.1298	0.9835	0.3026	0.9763
XRD Gt/(Gt+Lp)	MSB Sextet ~77K	0.8434	0.101	0.9825	0.2759	0.9749
XRD Gt/(Gt+Lp)	MSB Sextet ~20K	0.7768	-0.094	0.9742	0.0874	0.9631
XRD Gt/(Gt+Lp)	MSB 140 Bhf	-0.7548	-0.9714	0.1464	-0.959	-0.0344
XRD Gt/(Gt+Lp)	MSB 77 Bhf	-0.545	-0.9406	0.478	-0.9156	0.3261
XRD Gt/(Gt+Lp)	MSB 20 Bhf	0.535	-0.4888	0.9389	-0.3386	0.9132
XRD Gt/(Gt+Lp)	MSB 295K Fe2%	-0.741	-0.9695	0.177	-0.9564	-0.003
XRD Lp/(Gt+Lp)	MSB Sextet 140K	-0.8516	-0.9835	-0.1298	-0.9763	-0.3026
XRD Lp/(Gt+Lp)	MSB Sextet ~77K	-0.8434	-0.9825	-0.101	-0.9749	-0.2759
XRD Lp/(Gt+Lp)	MSB Sextet ~20K	-0.7768	-0.9742	0.094	-0.9631	-0.0874
XRD Lp/(Gt+Lp)	MSB 140 Bhf	0.7548	-0.1464	0.9714	0.0344	0.959
XRD Lp/(Gt+Lp)	MSB 77 Bhf	0.545	-0.478	0.9406	-0.3261	0.9156
XRD Lp/(Gt+Lp)	MSB 20 Bhf	-0.535	-0.9389	0.4888	-0.9132	0.3386
XRD Lp/(Gt+Lp)	MSB 295K Fe2%	0.741	-0.177	0.9695	0.003	0.9564
XRD Lp/(Gt+Lp)	XRD Gt/(Gt+Lp)	-1	-1	-1	-1	-1
Dry CA Fe	MSB 295K Fe2%	0.8414	0.0941	0.9822	0.2694	0.9745
Dry CA Fe	MSB Sextet 140K	-0.6411	-0.9555	0.3554	-0.9366	0.1874
Dry CA Fe	MSB Sextet ~77K	-0.6276	-0.9535	0.375	-0.9338	0.2091
Dry CA Fe	MSB Sextet ~20K	-0.7424	-0.9697	0.174	-0.9567	-0.0062
Dry CA Fe	XRD Gt/(Gt+Lp)	-0.3377	-0.9021	0.6527	-0.862	0.5357
Dry CA Fe	XRD Lp/(Gt+Lp)	0.3377	-0.6527	0.9021	-0.5357	0.862



Appx. Figure 4.1. XRD was performed on the freeze-dried bulk soils from plots 1, 2, 4, 7, 9 and 18 using a Bruker Advance diffractometer with a Co-K $\alpha$  source. Stacked XRD patterns represent in order plots 1, 2, 4, 7, 9 and 18 from top to bottom. XRD Mineral phases are indicated as follows: kaolinite (Ka); chlorite (Chl); quartz (Qz); and K-feldspar (K-Fld). Scan parameters of the bulk soil included a 0.02° increment at 2°/min using a 0.6 mm slit and a 2 $\theta$  interval of 2-70°. Data analysis was performed using the EVA software package (Bruker).



Appx. Figure. 4.2. Raw MBS spectra (observed data points) of freeze-dried plot samples 1, 2, 4, 7, 9 and 18 collected at 295, 140, 77 and 20 K. See Appx. Tables 4.2. and main Fig. 4.4. for detailed modeling of plot 2 and 4 (P2 and P4). See Appx. Table 4.3. for all average MBS parameters of spectra collected at all temperatures.



Appx. Figure 4.3.  $^{57}\text{Fe}$  Mössbauer spectra collected at 4.5 K for freeze-dried plots P2 and P4. Raw spectral data points are shown as black open circles. Modeled Fe site populations are indicated as colored lines: Q-FeIII (blue), Q-FeII (green), Q-Fe (violet), HFD-OxHy (orange), HFD-(b)OxHy (yellow), and total fit (red). This comparison shows that the P4 sample, which contained the most goethite of all analyzed plots based on XRD, has a larger sextet that is attributed to the presence of goethite in the P4 MBS spectrum. The P2 spectrum shows a smaller and broader sextet relative to the central doublet, which we attribute to the presence of both lepidocrocite and goethite in a 1:1 ratio as confirmed by XRD.

## CONCLUSION

In this work, we had three principal findings. (1) We found that mRNA sequences annotated as encoding putative *c*-type cytochromes, including pili, flagella, exopolysaccharide, carbon-degrading and TCA cycle enzymes collectively, with highest alignment to *Anaeromyxobacter*, *Geobacter* and *Desulfovibrio* genomes in the NCBI database, are important during Fe(III)-reduction in a humid tropical forest soil. Considering that recent whole genome sequencing and functional analysis of *Anaeromyxobacter* and *Geobacter* species have uncovered the presence of genes required for the use of O<sub>2</sub> as an electron acceptor and possible evolutionary branching from an ancient aerobic ancestor, our data emphasizes the importance of continued research to elucidate the current role and evolution of these organisms in redox oscillating tropical soils. (2) Our data show that soil Fe(III)-(oxyhydr)oxide crystal order can either increase or decrease depending on how fast Fe(II) is oxidized. Isotopically-labeled Fe(II), oxidized rapidly, forms highly disordered Fe(III) phases that are preferentially utilized as terminal electron acceptors during the onset of microbial Fe(III)-reduction in soil. (3) In the characterization of field-based soil samples, we find no significant difference between oxalate (AAO) and ascorbate (CA) extractable Fe derived from wet vs. dry soil. XRD patterns from Co- $\kappa\alpha$  radiation show differences in Fe oxide distributions comprising lepidocrocite ( $\gamma$ -FeOOH) and goethite ( $\alpha$ -FeOOH), within a dominant kaolinite group contribution in each sample. Development of a sextet in MBS spectra at 140 K and lower shows magnetic ordering and hyperfine parameters similar to that of naturally occurring goethite (i.e. present as Al-substituted, finely separated, and/or nano-crystalline phases). However, relative contributions from Fe-

substituted phyllosilicates (e.g. kaolinite group) and both Fe minerals goethite and lepidocrocite cannot be completely resolved or identified with confidence at 295, 140, 77 and ~20 K. The Fe(II) doublet in MBS spectra at 295, 140, 77 and ~20 K varies between each sample. Given the redox-dynamic nature of these soils in the field, which involve oxic/anoxic conditions, microbial Fe reduction etc., and the ambiguity in MBS assignment of the Fe(II) phases which result from such processes, it is not possible to adequately identify the observed MBS Fe(II) doublet as phyllosilicate-Fe(II) or as Fe(II) associated with other mineral phases (or organic matter) in this study. The ambiguity is non-trivial, particularly in redox-dynamic environments like tropical forest soils, where the co-evolution of Fe(II) and meta-stable and/or bio-reduced solid phases could indicate an ecologically significant shift in microbial metabolism and C and nutrient dynamics. However, by using chemical, XRD and MBS data together, we were able to show that increases in MBS Fe(II) (solid phase Fe(II)) were positively correlated with increases in XRD lepidocrocite:goethite ratios and citrate-ascorbate extractable Fe.

Interactions between Fe(III) minerals and Fe(III)-reducing bacteria in the environment play a critical role in determining the stability of C and availability of plant nutrients. This role is uniquely dynamic in highly active, highly weathered, humid tropical forest soils because of repeated redox cycling occurring as the result of precipitation frequency, OC pulses from overlying vegetation, reactivity of Fe(III)-(oxyhydr)oxides and microbial communities adapted to such conditions. Our principal findings as presented here collectively help elucidate the connection between micro/nano-scale Fe transformations and microbial Fe(III)-reduction in redox-dynamic tropical forest soils to better understand ecosystem-level processes.